



**University of Naples “Federico II”**

---

NOVEL TECHNOLOGIES FOR MATERIALS, SENSORS AND IMAGING  
International PhD program

PHD THESIS

# **Microfluidics assisted platforms for biotechnological applications**

**Emanuele Orabona**

Supervisor:  
**Dr. Luca De Stefano**  
Institute for Microelectronics and Microsystems  
National Council of Research

---

XXIV Cycle



# Table of contents

|   |           |
|---|-----------|
| Table of contents .....                                       | 3         |
| Introduction .....  | 5         |
| <b>1 Microfluidics basic concepts.....</b>                    | <b>13</b> |
| <b>1.1 Why microfluidics? .....</b>                           | <b>13</b> |
| <b>1.2 Microfluidics phenomena and equations .....</b>        | <b>14</b> |
| 1.2.1 Fluid mechanics .....                                   | 17        |
| 1.2.2 Transport and dynamic.....                              | 19        |
| <b>1.3 Modelling microfluidic circuit .....</b>               | <b>22</b> |
| 1.3.1 Analytical solutions.....                               | 23        |
| 1.3.2 Electric equivalent circuit.....                        | 25        |
| 1.3.3 Numerical simulations .....                             | 28        |
| <b>References .....</b>                                       | <b>31</b> |
| <b>2 Microfabrication techniques .....</b>                    | <b>33</b> |
| <b>2.1 Fabrication methods in microfluidics.....</b>          | <b>33</b> |
| <b>2.2 Soft lithography techniques.....</b>                   | <b>34</b> |
| 2.2.1 Materials characteristics.....                          | 36        |
| 2.2.2 Replica molding technique.....                          | 42        |
| 2.2.3 Surface activation processes .....                      | 43        |
| <b>2.3 Photographic procedure for masks fabrication .....</b> | <b>45</b> |
| <b>2.4 Porous silicon fabrication .....</b>                   | <b>49</b> |
| 2.4.1 Porous silicon as an optical transducer .....           | 52        |
| 2.4.2 Porous silicon surface functionalization .....          | 54        |
| <b>2.5 Porous silicon based microarray.....</b>               | <b>55</b> |
| 2.5.1 Fabrication process.....                                | 57        |
| <b>References .....</b>                                       | <b>59</b> |

|   |            |
|---|------------|
| <b>3 A microfluidics assisted porous silicon array for optical label-free biochemical sensing .....</b> | <b>63</b>  |
| <b>3.1 Design a microfluidic circuit for biochemical interactions .....</b>                             | <b>63</b>  |
| 3.1.1 Binding kinetic inside microchannels .....  | 65         |
| 3.1.2 Optimization of microfluidic circuit by numerical simulations.....                                | 69         |
| <b>3.2 Microfluidic integration on to a porous silicon based microarray.....</b>                        | <b>73</b>  |
| 3.2.1 Biofunctionalization of the microfluidic PSi-array.....   | 77         |
| 3.2.2 Binding kinetic analysis .....  | 79         |
| 3.2.3 DNA hybridization.....  | 84         |
| <b>References .....</b>   | <b>85</b>  |
| <b>4 A microfluidic circuit for synthetic biology.....</b>  | <b>89</b>  |
| <b>4.1 Cells culturing in microfluidic devices.....</b>   | <b>89</b>  |
| <b>4.2 In vitro testing of a genetic network.....</b>   | <b>96</b>  |
| 4.2.1 A microfluidic trap for yeast cells .....   | 100        |
| <b>References .....</b>   | <b>104</b> |
| <b>5 Electric field mapping in microfluidic devices .....</b>   | <b>107</b> |
| <b>5.1 Electrokinetic transport phenomena.....</b>  | <b>107</b> |
| <b>5.2 Electric field mapping in microfluidic devices .....</b>   | <b>108</b> |
| <b>References .....</b>   | <b>113</b> |
| <b>Conclusions.....</b>   | <b>115</b> |
| <b>Ringraziamenti .....</b>   | <b>119</b> |

# Introduction

“Smaller, faster, and cheaper” is the mantra referred to a huge number of commercial products which are of interest for a very large market, spanning from high-tech devices to everyday electronics, such as smartphones, digital video cameras, but also biomedical and healthcare instruments. The answer of research and development centres, both academic and industrial, to market requirements is a general trend to make things as smaller as possible. This effort is driven mainly by the electronic industry, which competition is focused on size reduction of basic components as the key for smaller and better devices, and, in ultimate analysis, for commercial success. However, there are also many other reasons why scaling things down in size is of crucial importance for science, in general. In this way, it is possible to detect, measure and build on the nanometer scale, which is the same size scale that Life uses. Working on the same scale as Nature does, helps to gain knowledge about fundamental biological and biophysical phenomena. Biomolecular and medical applications also demand down-scaling of both scientific apparatus and systems under studies: practical advantages are the possibility to decrease sample volumes, separate smaller particles, probe smaller areas and detect fewer molecules. From the theoretical point of view, new horizons can be explored in a very controlled way, and many models can be accurately tested: for example, in very thin channels, the ratio between volume and surface changes drastically and bulk forces are not predominant with the respect to surface interactions. This is also the technological and scientific environment where a new generation of devices born and grown: the so called lab-on-a-chip tools, which have been described as the results of the new millennium industrial revolution, due to their potential impact in all the fields of modern life [1]. An example schematic of a lab-on-a-chip device is illustrated in Figure 1.

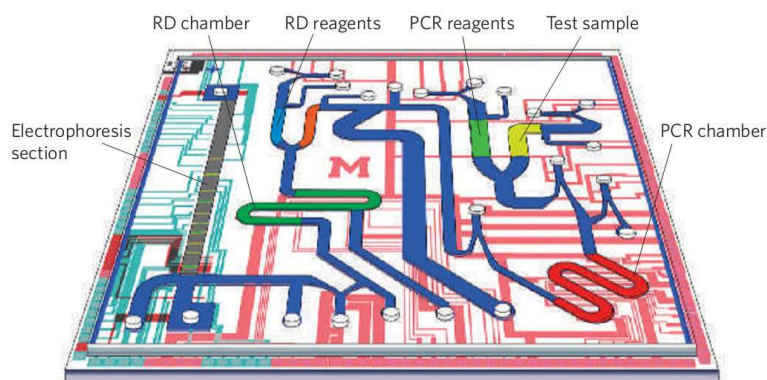


Figure 1 Schematic of a lab-on-a-chip for genetic analysis.

The micromanipulation of liquid started when the heavy use of fast etching techniques and smart handling of resist and sacrificial layers, obtained by bi-dimensional optical lithography, allowed the construction of complex structures. Although major developments occurred earlier in mechanical systems, it is only in 1975 that the first microfabricated device using liquid was reported by S.C. Terry at Stanford University [2]. In subsequent years devices such as miniaturized pumps, valves, mixers and sensors were invented, designed and fabricated [3,4]. Microfluidics was thus born, and within its core, the potential of using this technique in conjunction with life sciences. Many scientists believe that the development of microfluidic devices will revolutionize not only chemistry laboratory processes, but also the modern approach to the complex field of biology. Microfluidics is really a multi-disciplinary field of investigation, involving almost all the scientific branches of knowledge, such as physics, biology, engineering, chemistry and microtechnology. In particular, the fabrication of microfluidic systems was originated from the field of microelectromechanical systems (MEMS), which itself is a spin-off of the semiconductor industry. Lab-on-a-chip devices can be date to 1990, when Manz et al. [5] proposed that MEMS technologies could be applied to biological and chemical processes, and that a single device could incorporate many aspects of laboratory processes including sample preparation, separation, transport and detection. These miniaturized devices have been demonstrated in really many applications that

possess superior analytical performance even if the amount of reagents required is strongly reduced.

Another important issue was the use of novel, and cheaper, materials rather than crystalline silicon, which need to be purified, oriented and eventually doped in order to satisfy the industrial standard. Glass and polymers, like the resist SU8 or the polydimethylsiloxane (PDMS), classically used as sealing material in electronics, are nowadays more and more used to realize microfluidic circuits. Microfluidic tools boost the features of many kind of devices, by providing striking advantages over their macro correspondent. Compatibility with microfabrication technologies allows the integration of microfluidic circuits with micro, and actually nano, scale devices. As the length scale is reduced, processes such as thermal energy transfer are significantly faster and devices can operate with faster analysis and response time. Small size also makes microfluidic devices portable, which is particularly appealing for clinical or on-field use in point-of-care diagnostics [6]. Due to device compactness, lot of experiments, up to tenths of thousands, can be run in parallel or on one single chip in order to increase throughput. Microfluidic devices have the capability to handle liquid precisely in the nanoliter interval and reduce cost of running experiments by requiring less reagents [7]. Lab-on-a-chip can be designed to perform a wide range of tasks that span from detecting airborne toxins to DNA and protein sequences analysis, which are key actions in environment monitoring, genomic and proteomic, respectively [8]. Microfluidics can also be a breakthrough for a more biological approach to lab-on-a-chip applications, where tools are developed with the only aim to perform better what is already available at the lab scale. Therefore, microfluidics systems provide a real potential for improving the efficiency of techniques applied in drug discovery and biochemical diagnostics. Microfluidics related research is a field that has increased very much in last ten years. In particular, between 2004 and 2008 it had a great boost: the number of article has been growing with a quadratic law. Now the interest in microfluidics continues and the number of article is growing linearly with high production rate.

The aim of this PhD work is to exploit microfluidics features to improve the performances of some lab-on-a-chip designed for biotechnological applications:

microfabrication techniques developed in the frame of telecommunication systems have by far found many other fields of applications, in particular optical sensing of chemical substances and biomolecular process is of outmost relevance in defence, health, and environment, i.e. the principal items of social interest. The experience developed in design, fabricate, and test optical components or MEMS systems, can be successfully applied to the realization of lab-on-a-chip for specific scopes: two kind of microfluidics circuits for biotechnology have been considered, one integrated with the microarray technology, and the other devoted to cell manipulation. In general, microarrays technology is undergoing significant changes by improving not only the signal detection but also the support materials, the functionalization procedures, the scanning methods, and, last but not least, the integration of microfluidic circuits with the standard devices. Microarrays, originally developed for gene expression profiling ,offer the advantages of very high throughput, cost-effective analysis with low consumption of reagents, and quite rapid operative times. They are powerful devices for laboratory application in genomics, proteomics, pathogen detection, and also microbial ecology research. Most common microarrays use fluorescence as the transduction signal of molecular interaction under investigation. To overcome the intrinsic limits of this technology, such as chromophores photobleaching and quenching, label-free optical methods, like surface plasmon resonance imaging, ellipsometry, and spectroscopic reflectometry have been proposed [9–13]. In particular, recently a porous silicon based microarray for label free optical monitoring of molecular interactions has been proposed by Rea et al. [14]. One aim of the PhD program has been the integration of a proper microfluidic circuit with the porous silicon microarray: even if all the fabrication techniques are in principle compatible, this operation is not trivial nor straightforward. It required a proper design of the microfluidic network, the modelling of the biological phenomena at the microscale, the realization by soft lithography technique, the integration with the microarray, and finally the optical characterizations of the whole system. Final device is illustrated in Figure 1.

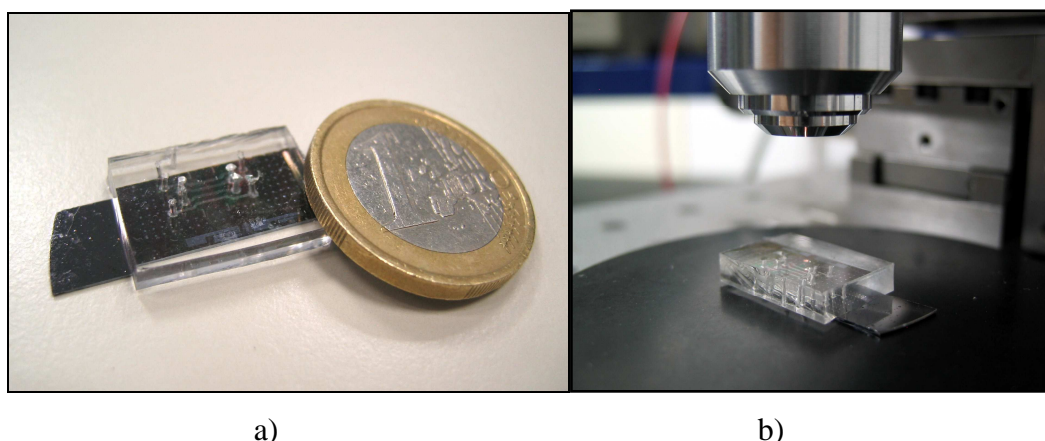


**Figure 2 Microfluidic assisted porous silicon array, a) compared to one euro coin and b) under a 10× objective for optical characterization.**

The manipulation of cells was for long time the domain of micro clamps and pipette, but direct mechanical contact has consequences on the cell surface which can result in damaging the membrane and perturbation of the interaction of the cell surface with its environment. Alternative cell manipulation techniques is thus strongly desired in order to facilitate cell sorting and diagnosis. Isolation and manipulation of cells can also be applied for diagnostic and purification purposes, especially in blood or bone marrow for the detection of cancer cell but also with pathogen disease (malaria, dengue fever, HIV) [15]. Also in this case, the fabrication of a microfluidic system for manipulation, feeding, and observation of a small number of living cells has been realized using soft lithography and computer aided design and simulations.

The PhD thesis is organized in four chapters plus a special one on a spin-off activity, which exploited some numerical and experimental tools developed during the main studies. The first chapter introduces to microfluidics basic concepts. Microfluidics fluid mechanics has been explained to give some basics to the reader, and dimensionless numbers useful in microfluidics have been presented. The last paragraph is dedicated to computer aided circuit modelling: analytical solutions are illustrated in few but very important cases; an alternative modelling based on electrical circuits formulation is also exposed; then numerical simulations are treated for all other cases.

Microfabrication techniques are developed in chapter two. It starts with a small introduction to fabrication methods in microfluidics, with an in depth look at soft-

lithography, which is a convenient non-photolithographic based approach for micro- and nano-fabrication extensively used in microfluidics. An innovative photographic low cost procedure for masks fabrication has been also presented. Porous silicon, and their related realization technique are also a topic of this chapter: Porous silicon is an ideal material as transducer for biosensing due to its sponge-like morphology characterized by a high specific surface area that assures an efficient and rapid interaction with the species to detect; its fabrication process is compatible with microelectronics, which makes it an important material in lab-on-a-chip application.

The third chapter is completely dedicated to a microfluidic assisted porous silicon array for optical label-free biochemical sensing. The integration of a microfluidic circuit with a porous silicon microarray is step-by-step illustrated, and its features are investigated. Experimental proofs have been obtained for the selective label-free DNA-DNA interaction. Finite element method analysis was applied to the characterization of the biomolecular interactions taking place in a microfluidic assisted microarray. Numerical simulations have been used for the optimization of geometrical and physical parameters of the sensing device. Different configurations have been analyzed and general considerations have been derived. Stationary and time dependent results have also been obtained.

Microfluidics applied to synthetic biology is the topic of the fourth chapter. In this section, an integrated computational and experimental strategy based on a microfluidic device to achieve control of a synthetic biological system has been proposed. This strategy has been applied to study and model a synthetic genetic network constructed in yeast cells.

The thesis ends with a chapter on a side activity: the electric field mapping in microfluidic devices. In this chapter a new technique to measure the direction and amplitude of the electric field generated by microelectrodes in a liquid environment, as often used in microfluidic devices, is presented. The method is based on the use of optical tweezers as a force transducer. A trapped, charged particle behaves as a probe. By this technique, it is possible to obtain a detailed map of the electric field, even for very complex electrode structures with high resolution.

Finally, the conclusions and perspectives of this very promising research field are presented.

## References

- [1] J. El-Ali, P.K. Sorger, K.F. Jensen, Cells on chips, *Nature*. 442 (2006) 403-411.
- [2] S.C. Terry, J.H. Jerman, J.B. Angell, A gas chromatographic air analyzer fabricated on a silicon wafer, *IEEE Transactions on Electron Devices*. 26 (1979) 1880- 1886.
- [3] S. Shoji, M. Esashi, T. Matsuo, Prototype miniature blood gas analyser fabricated on a silicon wafer, *Sensors and Actuators*. 14 (1988) 101-107.
- [4] M. Esashi, S. Shoji, A. Nakano, Normally close microvalve and micropump fabricated on a silicon wafer, in: *IEEE Micro Electro Mechanical Systems, 1989, Proceedings, An Investigation of Micro Structures, Sensors, Actuators, Machines and Robots, IEEE, 1989: pp. 29-34.*
- [5] A. Manz, N. Graber, H.M. Widmer, Miniaturized total chemical analysis systems: A novel concept for chemical sensing, *Sensors and Actuators B: Chemical*. 1 (1990) 244-248.
- [6] P. Yager, T. Edwards, E. Fu, K. Helton, K. Nelson, M.R. Tam, et al., Microfluidic diagnostic technologies for global public health, *Nature*. 442 (2006) 412-418.
- [7] N.-T. Nguyen, S. Wereley, *Fundamentals and Applications of Microfluidics*, 1st ed., Artech House, 2002.
- [8] G.H. Sanders, A. Manz, Chip-based microsystems for genomic and proteomic analysis, *TrAC Trends in Analytical Chemistry*. 19 (2000) 364-378.
- [9] K.M. Hansen, T. Thundat, Microcantilever biosensors, *Methods*. 37 (2005) 57-64.
- [10] X. Yu, D. Xu, Q. Cheng, Label-free detection methods for protein microarrays, *Proteomics*. 6 (2006) 5493-5503.
- [11] J. Homola, Present and future of surface plasmon resonance biosensors, *Analytical and Bioanalytical Chemistry*. 377 (2003) 528-539.
- [12] E. De Tommasi, L. De Stefano, I. Rea, V. Di Sarno, L. Rotiroti, P. Arcari, et al., Porous Silicon Based Resonant Mirrors for Biochemical Sensing, *Sensors*. 8 (2008) 6549-6556.
- [13] L. De Stefano, D. Alfieri, I. Rea, L. Rotiroti, K. Malecki, L. Moretti, et al., An integrated pressure-driven microsystem based on porous silicon for optical monitoring of gaseous and liquid substances, *Physica Status Solidi (a)*. 204 (2007) 1459-1463.
- [14] I. Rea, A. Lamberti, I. Rendina, G. Coppola, M. Gioffre, M. Iodice, et al., Fabrication and characterization of a porous silicon based microarray for label-free optical monitoring of biomolecular interactions, *Journal of Applied Physics*. 107 (2010) 014513-014513-4.
- [15] C. Yi, C.-W. Li, S. Ji, M. Yang, Microfluidics technology for manipulation and analysis of biological cells, *Analytica Chimica Acta*. 560 (2006) 1-23.



# Chapter 1

## Microfluidics basic concepts

The study of fluid motion in lab-on-a-chip devices is called microfluidics. In this chapter microfluidics fluid mechanics has been explained to give some basics to the reader for the comprehension of topics presented in the next chapters. The last paragraph is dedicated to circuit modelling used in chapter 3: Analytical solutions are illustrated in few but very important cases; the modelling with electrical circuits is exposed for most of case; then numerical simulations are treated for all other cases.

### 1.1 Why microfluidics?

Microfluidics is the science that studies the manipulation of small ( $10^{-9}$  to  $10^{-18}$  litres) amounts of fluids, using channels with dimensions of tenths to hundreds micrometres. Microfluidics is the perfect tool to integrate complex systems devices, the so-called lab-on-a-chip, for biology and chemistry applications, since it allows automation of all operations, and also offers possibility of scaling down that rival with respect to electronics integrated circuits.

Furthermore, microfluidic devices can work with smaller reagent volumes, shorter reaction time, and parallel operations, which means a new capability in the control of molecules and cells concentrations in space and time. Microfluidic devices exploit their most obvious characteristic, small size, and less obvious characteristics of fluids in microchannels, such as laminar flow. Microfluidic devices are nowadays commercially employed in chemistry, biology, genomics, proteomics, pharmaceuticals, bio-defence, and other areas where their advantages exceed standard methodologies. Although most current effort in microfluidics concerns devices with applications in chemistry [1],

biology [2], and medicine [3] news and more foreseen applications are in the field of physical sciences for systems control, heat management, energy generation, displays and printing technology [4,5]. In fact some microfluidic applications as liquid crystal displays and ink jet printers have had enormous industrial impact and they now are certainly large consumer products.

## 1.2 Microfluidics phenomena and equations

The behaviour of fluids at the microscale can differ from “macrofluidic” behaviour in that factors such as surface tension, energy dissipation, and fluidic resistance that dominate system behaviour. Reasoning on scaling laws (Table 1) can be useful to anticipate the changes one may expect from miniaturizing a given system. When going from the macroscale to the microscale is inevitable an increase of the surface area to volume (SAV) ratio. This implies that the surface-related force becomes dominant with respect to volume-related force. For example, in microfluidic the capillary force influences the system more than gravity.

| Quantity                           | Scaling law |
|------------------------------------|-------------|
| Intermolecular van der Waals force | $l^{-7}$    |
| Capillary force                    | 1           |
| Flow velocity                      | 1           |
| Electrostatic force                | $l^2$       |
| Diffusion time                     | $l^2$       |
| Mass                               | $l^3$       |
| Force of gravity                   | $l^3$       |
| Force Centrifuge                   | $l^4$       |

Table 1 Scaling law of some physical quantities.

The interactions in a fluid can be described as a many-body problem with one set of equations for every elements (in this case for every molecule) and together these equations form a huge system of equations. Fluids can be also considered under the

continuum model, and so discrete quantities like mass and force become continuous fields. In this approximation the macroscopic properties of a fluid are the same as the fluid was perfectly continuous instead of, as in reality, consisting of molecules. Physical quantities such as the mass, momentum and energy associated with a small volume of fluid containing a sufficiently large number of molecules can be calculated as the sum of the corresponding quantities for the molecules in the volume. In microfluidic volumes the continuum approximation remains valid. In fact, for example, a picoliter volume of water contains  $3 \times 10^{13}$  molecules, a number large enough to make valid this hypothesis. As shown in Figure 3, measured quantity on a fluid volume encounters large fluctuations due to the molecular structure of the fluid as its volume decrease. Thus, in the microfluidic range steady and reproducible measurements are possible [6].

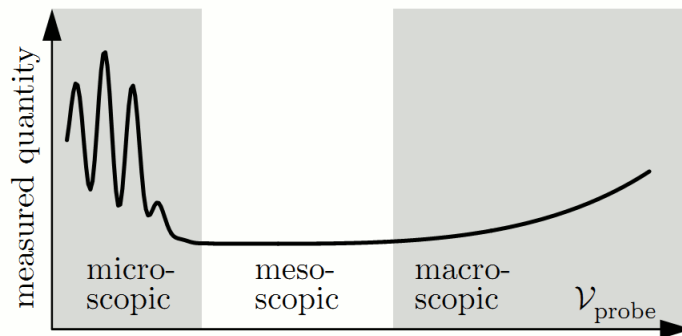


Figure 3 A sketch of a measured physical quantity of a liquid as a function of the volume probed. Large fluctuations are due to the molecular structure of the fluid as its volume decreases. In the microfluidic range, steady and reproducible measurements are possible.

This happens once the probe volume is big enough to contain a sufficiently large number of molecules, such that well defined average values with small statistical fluctuations are obtained. In nanofluidics, where smaller length scales and less fluid molecules are present, the continuum hypothesis starts to break down [7]. When the continuum approximation loses its validity molecular effects change drastically the fluid behaviour.

To understand better the validity range of continuum hypothesis is useful to distinguish between gas and liquids, because they have different nature: while gas molecules move

ballistically and collide only rarely, liquid molecules are in constant collision. In the first case, using the kinetic theory of gases, the mean free path  $\lambda$  between collisions can be calculated from

$$\lambda_f = \frac{1}{\pi n a^2} \quad (1)$$

where  $n$  is the number of molecules per unit volume with diameter  $a$ . For example, an ideal gas at 1 atm and 25°C has a mean free path  $\lambda_f \sim 70\text{nm}$  that increases at lower pressures. As channel dimensions decrease, the mean free path occupies an increasingly significant portion of the flow and thus plays an increasingly important role. The Knudsen number

$$Kn = \frac{\lambda_f}{L} \quad (2)$$

is the ratio of the mean free path (the length scale on which molecules matter) to a length channel scale  $L$ . It express a measure of noncontinuum effects that play an increasing role as  $Kn$  increases. Gases behaves like a continuum up to a distance  $\lambda_f$  from the wall, and influence the boundary conditions obeyed by the fluid. Three distinct Knudsen regimes have been measured in pressure-driven flow [8]:

- $Kn \ll 1$  where the gas behaves as a no-slip fluid;
- $Kn \sim 1$  where the gas behaves as a continuum but slips at the boundaries;
- $Kn \gg 1$  where the continuum approximation breaks down completely.

On the other hand liquid are incompressible and its molecules are in constant contact, making the concept of mean free path less meaningful. However noncontinuum effects appear to play a role only when the liquids are confined to molecular length scales.

The fluid behaviour in a system is dictated by a competition between various phenomena, which can be described by a series of dimensionless numbers expressing their relative importance. These dimensionless numbers form a sort of parameter space for microfluidic physics, ready to be explored [9]. These dimensionless number are summarized in Table 2.

| Name     | Symbol | Definition                       | significance  |
|----------|--------|----------------------------------|---|
| Reynolds | Re     | $Re = \frac{\rho u_0 L_0}{\eta}$ | $\frac{\text{inertial force}}{\text{viscous force}}$                  |
| Peclet   | Pe     | $Pe = \frac{u_0 L}{D}$           | $\frac{\text{diffusion time}}{\text{convection time}}$                |
| Knudsen  | Kn     | $Kn = \frac{\lambda_f}{L}$       | $\frac{\text{molecular mean free path}}{\text{length channel scale}}$ |

Table 2 Dimensionless numbers used in microfluidics.

In this work all fluids considered are Newtonian, which means that the stress versus strain rate curve is linear and passes through the origin, with viscosity as the constant of proportionality.

### 1.2.1 Fluid mechanics

The velocity field for a Newtonian fluid obeys the Navier-Stokes equations, which essentially represent the continuum version of Newton's Law  $F = ma$  per unit volume:

$$\rho \left[ \frac{\partial \vec{u}}{\partial t} + (\vec{u} \cdot \vec{\nabla}) \vec{u} \right] = -\vec{\nabla} p + \eta \nabla^2 \vec{u} + \vec{f} \quad (3)$$

where  $u$ ,  $p$ ,  $\rho$  and  $\eta$  are the velocity field, the pressure, the density and dynamic viscosity of the fluid, respectively. In this equation inertial acceleration terms appear on the left and forces on the right; here  $f$  represents the body force densities. The body forces are external forces that act throughout the entire body of the fluid as the gravitational force (in terms of the density  $\rho$  and the acceleration of gravity  $g$ ) or the electrical force (in terms of the charge density  $\rho_{el}$  of the fluid and the external electric field  $E$ ); the resulting force density from these two body forces is:

$$\vec{f} = \vec{f}_{grav} + \vec{f}_{el} = \rho \vec{g} + \rho_{el} \vec{E}. \quad (4)$$

To the Navier-Stokes must be added the mass conservation equation

$$\frac{\partial \rho}{\partial t} + \nabla \cdot (\rho \vec{u}) = 0 \quad (5)$$

and if the material density is constant, it becomes:

$$\nabla \cdot \vec{u} = 0$$

When inertial forces are small compared to viscous forces, which is usually the case in microfluidic channels, the nonlinear term can be neglected, leading to the Stokes equation:

$$\rho \frac{\partial \vec{u}}{\partial t} = -\vec{\nabla} p + \eta \nabla^2 \vec{u} + \vec{f} \quad (6)$$

To see this, we can compare the nonlinear (or inertial) term  $\rho(\vec{u} \cdot \vec{\nabla})\vec{u}$  with the viscous term  $\eta \nabla^2 \vec{u}$ . We denote by  $L_0$  the length over which the derivative of the velocity field changes significantly, and we denote by  $u_0$  the characteristic velocity of the flow. The ratio between the inertial and the viscous term can then be estimated as

$$\frac{|\rho(\vec{u} \cdot \vec{\nabla})\vec{u}|}{|\eta \nabla^2 \vec{u}|} \approx \frac{\rho u_0^2 / L_0}{\eta u_0 / L_0^2} = \frac{\rho u_0 L_0}{\eta} \quad (7)$$

Hence if  $\rho u_0 L_0 / \eta \ll 1$  we can indeed neglect the nonlinear/inertial term. The dimensionless number that appeared on the right-hand side of eq. (7) is called Reynolds number Re:

$$\text{Re} = \frac{\rho u_0 L_0}{\eta} \quad (8)$$

$L_0$  is also called “hydraulic diameter” and generally is four times the cross-sectional area divided by the wetted perimeter, which leads to [10]:

$$L_0 = \begin{cases} d & \text{for cylindrical channel (d=diameter)} \\ \frac{2}{1/h + 1/w} & \text{for rectangular channel (h=height; w=width)} \end{cases} \quad (9)$$

Fluids in great channels are often turbulent and behave chaotically, where an infinitesimal change in initial conditions totally change the flow pattern. Our weather system is an excellent example of a turbulent fluidic system and can be accurately simulated for short periods of time, but on a larger time scale the flow pattern cannot be determined even with the most accurate initial conditions. When scaling down in size, inertial energies decrease more rapidly than viscous energies. Viscosity thus dominates and the flow can be divided into streamlines, which slide smoothly over one another. A

small bead into the fluid will follow a streamline and mixing occurs only on a molecular level by diffusion. This type of flow is called laminar and is the most commonly encountered in microfluidic devices. The Reynolds number is able to describe the flow regime in fluid dynamics (Figure 4).

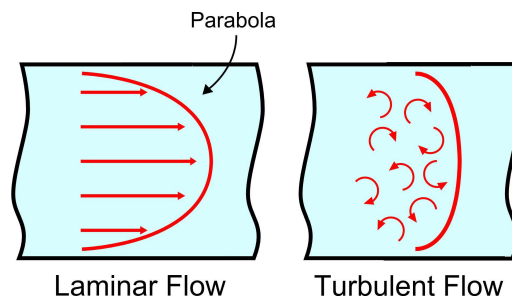


Figure 4 Laminar and turbulent flows.

In cylindrical channel the flow transition value takes place at  $Re = 2300$ :  $Re < 2300$  indicates a laminar flow, as  $Re$  approaches to 2300 the flow starts to show some turbulence and for  $Re > 2300$  the flow is considered turbulent. In microfluidics, the flow in microchannels is almost always laminar, which it means that the velocity of a particle in a fluid stream is not a random function of time and is possible to predict its position in the fluid as function of time. In microfluidics the Reynolds number is generally  $< 0.1$  because of the small size of microchannels. For example, a microchannel with circular cross section with a radius of  $25 \mu\text{m}$  filled with water that flows at  $100 \mu\text{m/s}$  has a Reynolds number of  $5 \cdot 10^{-6}$ . If we downscale further and investigate atomistic flows, fluctuations become significant and, for example, Monte Carlo methods can be used to simulate flow patterns [11].

### 1.2.2 Transport and dynamic

It is important to remember that fluids are made of molecules, and this discreteness reveals itself in the phenomenon of diffusion. Both the molecules of the fluid and any “tracer” or additive move diffusively through the fluid. It is a statistical phenomena on the molecular level caused by random motion such as Brownian motion. Over macroscopic distances diffusion is a very slow process, but in microchannels of a

typical microfluidic system, diffusion can give a significant contribution to the transport of matter. Random molecular motion tends to set up a diffusion current density  $J_{diff}$  of the solute from regions of high density to low concentration density  $c$ . This phenomenon is expressed by the Fick's first law:

$$\overrightarrow{J}_{diff} = -D\overrightarrow{\nabla}c \quad (10)$$

where  $D$  is the diffusion coefficient of the molecular species. Using the continuity equation for flux and concentration:

$$\frac{\partial c}{\partial t} + \overrightarrow{\nabla} \cdot \overrightarrow{J}_{diff} = 0 \quad (11)$$

it's possible to obtain the Fick's second law:

$$\frac{\partial c}{\partial t} = D\nabla^2 c \quad (12)$$

that predicts how diffusion causes the concentration to change with time. However diffusion can be simply modelled in one dimension with a dimensional analysis of (12)

$$L = \sqrt{Dt} \quad \text{or} \quad t = \frac{L^2}{D} \quad (13)$$

where  $L$  is the distance that a particle covers in a time  $t$ . These equations could be useful to understand the contribution that diffusion gives to transport of matter. For example a bio-molecule with  $D=1 \times 10^{-10} \text{ m}^2/\text{s}$  in water go through few microns in 1s, but it employs  $5 \cdot 10^6 \text{ s}$  for 1 cm. As show in Figure 5 ,one consequence of laminar flow is that two or more streams flowing in contact with each other will not mix except by diffusion [12]. This is not an advantage when mixing is desired, so to enhance mixing mechanism in microfluidic devices many schemes have been proposed to maximize the interfaces between solutions to allow diffusion to act quickly [13]. An interesting solution was proposed by Strook et al. [14] which propose a passive method for mixing streams of steady pressure-driven flows in microchannels at low Reynolds number stirring the flow with some bends on to bottom of the microchannel (see Figure 6).

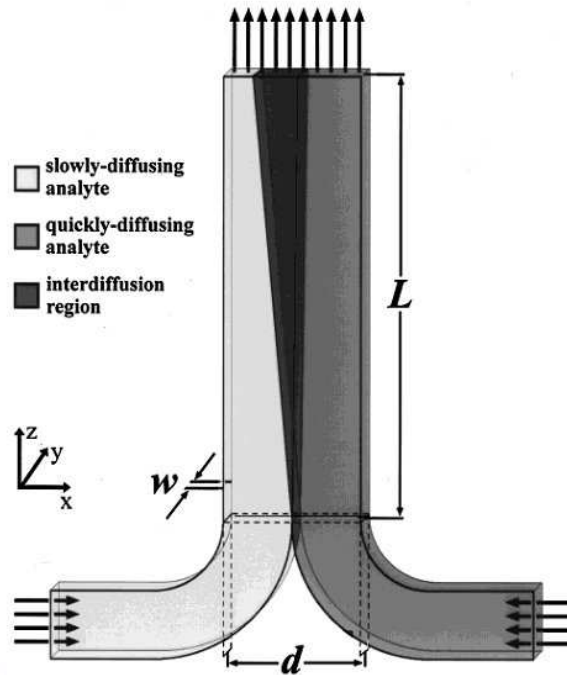


Figure 5 Mixing mechanism in microchannel: diffusion. The flow is steady state, projecting the interdiffusion along the length of the channel. The asymmetric development of the interdiffusion region is due to the difference in diffusion coefficients between the two diffusing species.

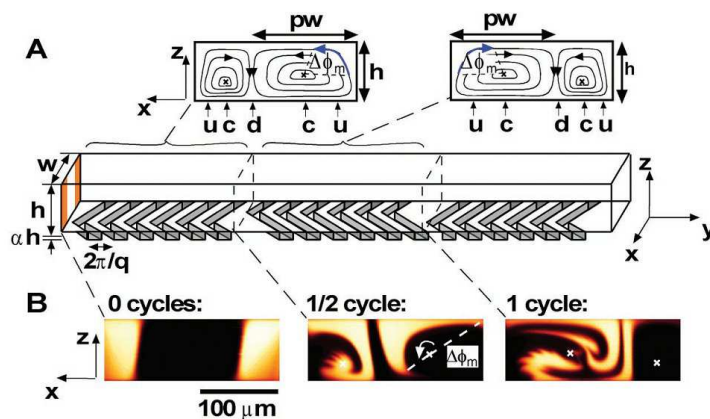


Figure 6 Staggered herringbone mixer (SHM). (A) Schematic diagram of one-and-a-half cycles of the mixer. A mixing cycle is composed of two sequential regions of ridges. (B) Confocal micrographs of vertical cross sections of fluorescent solution.

In microfluidic systems is often necessary to move concentrations of molecules around in microchannels. Hence, the velocity of the liquid carrying the molecules is not zero as assumed previously. Now, the solute molecules are transported both by diffusion due to concentration gradients and by convection due to the moving liquid. As a result the diffusion equation (12) must be changed into the convection-diffusion equation to handle this more general case. It can be obtained considering the convection contribute into the total flux  $\vec{J}$

$$\vec{J} = \vec{J}_{diff} + \vec{J}_{conv} = -D\vec{\nabla}c + \vec{u}c \quad (14)$$

And substituting into (11)

$$\frac{\partial c}{\partial t} + \vec{u} \cdot \nabla c = D\nabla^2 c \quad (15)$$

As for Reynolds number, it's possible now to introduce the dimensionless Péclet number,  $Pe$ , to characterize the importance of convection relative to diffusion. The Péclet number is defined as the ratio of the time it takes to diffuse the distance  $L$  relative to the time it takes to cover the same distance by convection:

$$Pe = \frac{\text{diffusion time}}{\text{convection time}} = \frac{L^2 / D}{L / u_0} = \frac{u_0 L}{D} \quad (16)$$

A high Péclet number means that convection dominates ( $L$  is large), while a low Péclet number means that diffusion dominates ( $D$  is large).

### 1.3 Modelling microfluidic circuit

The Navier-Stokes equation is notoriously difficult to solve analytically because it is a nonlinear differential equation. Analytical solutions can however be found in a few, but very important cases. It is important to study such idealized flows, since they provide basic understanding of the behaviour of liquids flowing in the microchannels of lab-on-a-chip systems. From these analytical solutions it's possible to create simple microfluidic networks models to study the fluid dynamic and transport. More complicated systems involving more than one differential equation need to be solved with numerical methods.

### 1.3.1 Analytical solutions

A fluid in mechanical equilibrium must be in equilibrium relative to the walls of the channel containing it, because otherwise it would continuously lose kinetic energy by heat conversion due to internal friction originating from viscous forces inside the fluid. The velocity field is therefore zero everywhere.

$$u(\vec{r}) = 0, \quad \text{for } \vec{r} \in \Omega \quad (17)$$

The Navier-Stokes equation (3) reduces to

$$0 = -\vec{\nabla}p - \rho g \hat{e}_z \quad (18)$$

Where  $\rho g \hat{e}_z$  is the gravity force along  $z$  direction. For an incompressible fluid, as water, it can be easily integrated, since it depends only on  $z$ , giving

$$p = p_0 - \rho g z \quad (19)$$

where  $p_0$  is the pressure at the arbitrarily defined zero-level  $z = 0$ . This relation points to an easy way of generating pressure differences in liquids often used in microfluidics devices.

Pressure-driven, steady-state flows in channels, also called Poiseuille flows or Hagen-Poiseuille flows, are an important class of analytical solutions to the Navier-Stokes equation. This class is very important for the basic understanding of liquid manipulation in lab-on-a-chip systems. In a Poiseuille flow the fluid is driven through a long, straight, and rigid channel by imposing a pressure difference between the two ends of the channel. The channel, taken parallel to the  $x$  axis with an arbitrary cross-sectional shape as illustrated in Figure 7, is assumed to be translation invariant in that direction. The constant cross-section in the  $yz$  plane is denoted  $C$  with boundary  $\partial C$ . A constant pressure difference  $\Delta p$  is maintained over a segment of length  $L$  of the channel. The gravitational force is not considered. The translation invariance of the channel in the  $x$  direction implies that the velocity field is a 1D flow field without the time dependence since steady state are considered.

$$\vec{u} = u_x(y, z) \hat{e}_x \quad (20)$$

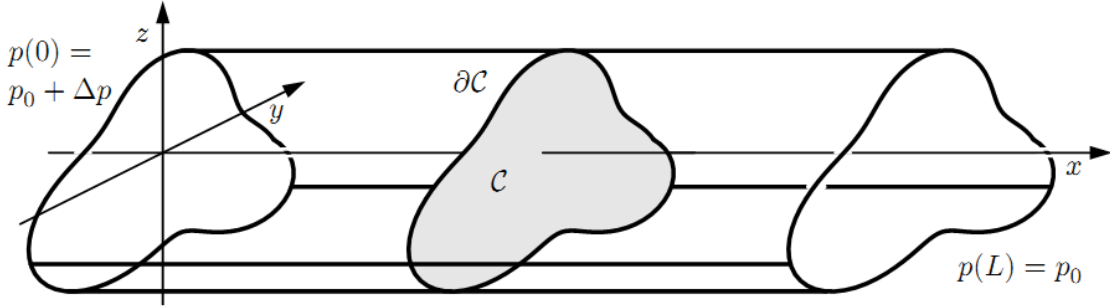


Figure 7 Poiseuille flow in a straight channel with an arbitrary cross-section [6].

Solving the Navier-Stokes equation (3) in the 1D case, without time-dependence and without body forces:

$$\eta[\partial_y^2 + \partial_z^2]u_x(y, z) = \partial_x p(x) \quad (21)$$

it's possible to note that the left-hand side is a function of  $y$  and  $z$  while the right-hand side is a function of  $x$ . So the solution can be found imposing the two sides of the Navier-Stokes equation equal to the same constant. The pressure must be a linear function of  $x$  and imposing the boundary condition, the following expression can be obtained

$$p(x) = \frac{\Delta p}{\eta L}(L - x) + p_0 \quad (22)$$

The final second order differential equation for velocity that accomplish the no-slip boundary condition is given by

$$\begin{aligned} [\partial_y^2 + \partial_z^2]u_x(y, z) &= -\frac{\Delta p}{\eta L} & \text{for } (y, z) \in C \\ u_x(y, z) &= 0 & \text{for } (y, z) \in \partial C \end{aligned} \quad (23)$$

For a channel of length  $L$  and a circular cross-section of radius  $a$ , the solution is a simple paraboloid

$$u_x(y, z) = \frac{\Delta p}{4\eta L}(a^2 - y^2 - z^2) \quad (24)$$

Instead for rectangular channel where the width-to-height aspect ratio is very large (as often happens in microfluidics) the infinite parallel channel approximation works well. In this case the solution is a simple parabola (Figure 8)

$$u_x(z) = \frac{\Delta p}{2\eta L}(h-z)z \quad (25)$$

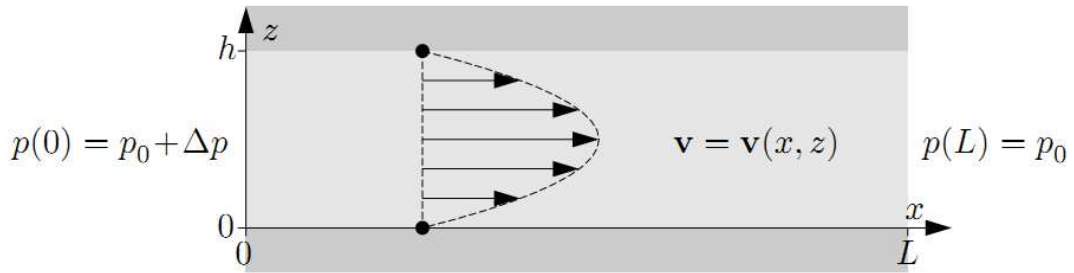


Figure 8 Infinite parallel flow [6].

### 1.3.2 Electric equivalent circuit

As explained in the previous paragraph, the fluid can be driven through a long, straight, and rigid channel by imposing a pressure difference between the two ends of the channel. It is described by the law:

$$\Delta p = R_{hyd} Q \quad (26)$$

where  $\Delta p$  is the pressure difference along the channel,  $R_{hyd}$  is the hydraulic resistance and  $Q$  is the flow rate. This law is completely analogous to the Ohm's law  $\Delta V = RI$  relating the electrical current  $I$  through a wire with the electrical resistance  $R$  and an electrical potential difference  $\Delta V$  along the wire. For example the hydraulic resistance of a microchannel with circular cross section can be calculated by the following equation:

$$R_{hyd} = \frac{8\mu L}{\pi} \cdot \frac{1}{a^4} \quad (27)$$

where  $a$  and  $L$  are the radius and length of the microchannel. Instead the hydraulic resistance of microchannel with rectangular cross section (as often happens in microfluidics) can be calculated by the following equation:

$$R_{hyd} = \frac{12\mu L}{1-0.63(h/w)} \cdot \frac{1}{h^3 w} \quad (28)$$

where  $L$ ,  $h$  and  $w$  are the length, height and width of the microchannel [6].

Other hydraulic resistance can be found in the Table 3.

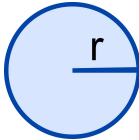
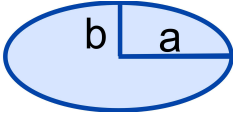
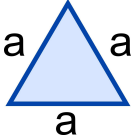
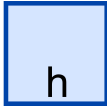
| Channel shape |   | $R_{hyd}$  |
|---------------|---|--|
| Circle        |    | $\frac{8}{\pi} \eta L \frac{1}{a^4}$                           |
| Ellipse       |   | $\frac{4}{\pi} \eta L \frac{1+(b/a)^2}{(b/a)^3} \frac{1}{a^4}$ |
| Triangle      |  | $\frac{320}{\sqrt{3}} \eta L \frac{1}{a^4}$                    |
| Rectangle     |  | $\frac{12\mu L}{1-0.63(h/w)} \cdot \frac{1}{h^3 w}$            |
| Square        |  | $\frac{12\mu L}{1-0.63} \cdot \frac{1}{h^4}$                   |

Table 3 A list over the hydraulic resistance for straight microchannels with different cross sectional shape [6].

As for electric resistors it's easy to show the validity for low Reynolds Number of the law of additivity of hydraulic resistors in a series coupling (Figure 9)

$$R = \sum_i R_i \quad (29)$$

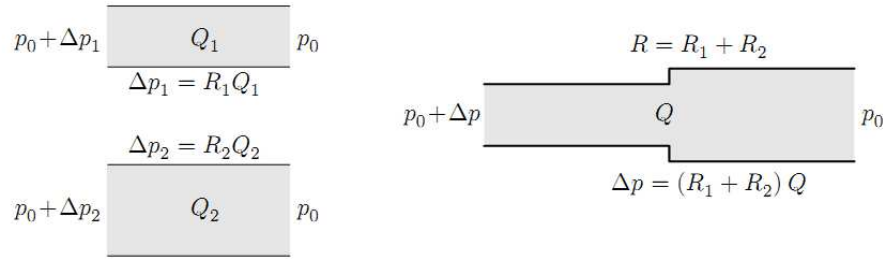


Figure 9 The series coupling of two channels with hydraulic resistance  $R_1$  and  $R_2$  [6].

and the validity of the law of additivity of inverse hydraulic resistances in a parallel coupling (Figure 10)

$$\frac{1}{R} = \sum_i \frac{1}{R_i} \quad (30)$$

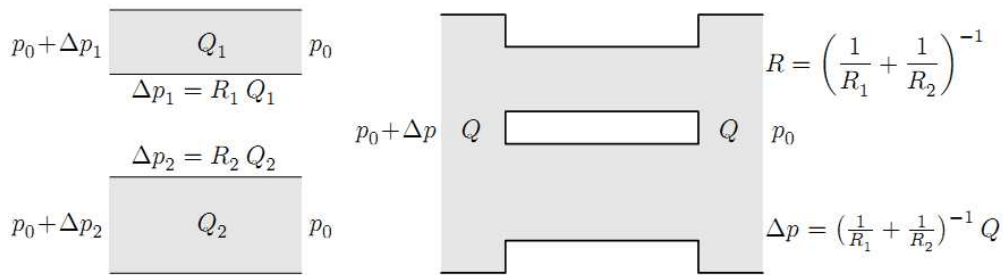


Figure 10 The parallel coupling of two channels with hydraulic resistance  $R_1$  and  $R_2$  [6].

For a given microfluidic network it's possible to draw the equivalent electric network: channels with hydraulic resistances  $R_{\text{hyd}}$  become resistors, flow rates  $Q$  become currents, and pumps delivering pressure differences  $\Delta p$  become batteries (see Figure 11). For any given fluidic network or circuit one can then apply Kirchhoff's laws:

- a) At any node in a microfluidic circuit, the sum of flow rates is zero;
- b) The sum of the pressure differences around any closed circuit is zero.

However the analogy with electric circuit is even more complete: it's possible to define a hydraulic capacitance and inductance exploiting the gas entrapment in the channels and elasticity of microchannel walls.

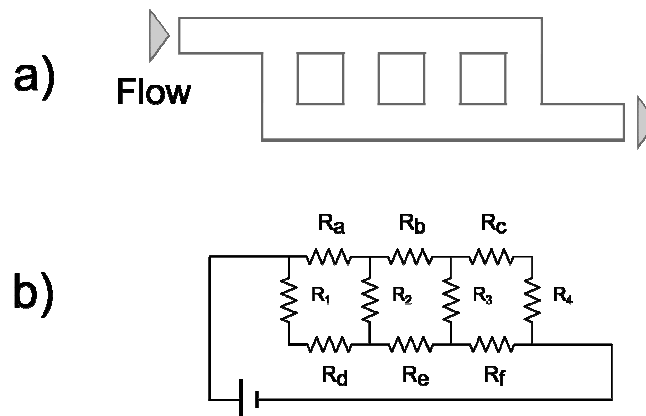


Figure 11 For a given microfluidic network (a) it's always possible to draw the equivalent electric network (b). Channels with hydraulic resistances  $R_{\text{hyd}}$  become resistors, flow rates  $Q$  become currents, and pumps delivering pressure differences  $\Delta p$  become batteries.

### 1.3.3 Numerical simulations

The finite element analysis is a powerful method for modelling and solving all kinds of scientific and engineering problems based on partial differential equations (PDEs). The solution approach is based either on eliminating the differential equation completely (steady state problems), or rendering the PDE into an approximating system of ordinary differential equations, which are then numerically integrated using standard techniques. The Finite Element Method is a good choice for solving partial differential equations over complicated domains, when the domain changes, or when the desired precision varies over the entire domain. The finite element analysis software package used in this work is FEMLAB. With FEMLAB it's possible extend conventional models for one type of physics into multiphysics models that solve coupled physics phenomena and do so simultaneously.

To find the solution, boundary conditions must be imposed; they define the interface between the model geometry and its surroundings. Neumann and Dirichlet conditions are allowed: the first specifies the values a solution needs to take on the boundary of the domain; the second instead specifies the values that the derivative of a solution is to take on the boundary of the domain. Three are the condition types that have been

imposed on Navier-stokes equation (3) used in these work: wall, velocity, pressure (no viscous stress) and laminar inflow and outflow.

### **Navier-Stokes boundary type: wall**

These boundary conditions describe the existence of a solid wall. In all studied cases it has been used the so-called wall-no-slip boundary condition for the velocity field for boundaries  $\partial\Omega$  that are solid walls

$$u(\vec{r}) = 0, \quad \text{for } \vec{r} \in \partial\Omega \quad (\text{no-slip}) \quad (31)$$

The microscopic origin of this condition is the assumption of lack of interactions between molecules and walls. Only for rarefied gases or narrow channels, where the mean free path of the gas molecules is comparable with the channel dimensions, is it necessary to abandon the no-slip boundary condition.

### **Navier-Stokes boundary type: velocity**

This boundary type describes different ways to specify conditions on a boundary where the fluid is supposed to enter or exit the domain. For these boundaries it's possible to specify the fluid's velocity equal to a given vector

$$\vec{u} = \vec{u}_0 \quad (32)$$

### **Navier-Stokes boundary type: pressure (no viscous stress)**

This boundary condition states the value of the pressure and that the viscous boundary force is zero:

$$p = p_0 \quad (33)$$

$$\eta \nabla^2 \vec{u} = 0 \quad (34)$$

### **Navier-Stokes boundary type: laminar inflow and outflow**

In microfluidic devices, flows often have a very low Reynolds number and a fully developed laminar profile. Thus it is reasonable to assume this profile in any inlet and outlet boundary. This condition simulate the effect of a fictitious channel outside of the

true geometry. The inlet and outlet lengths should be set large enough so that the flow can develop its laminar form.

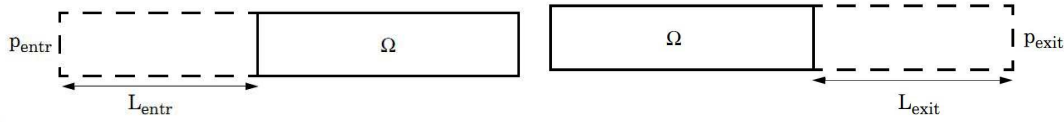


Figure 12 Sketch of the physical situation simulated when using the laminar inflow and out flow boundary condition.  $\Omega$  is the actual computational domain while the dashed domain is a fictitious domain [15].

Instead for which concerns convection and diffusion equation (15) there are three condition type that have been used in these work.

### Convection and diffusion boundary type: concentration

A user-specified concentration is imposed usually for inlet condition

$$c = c_0 \quad (35)$$

### Convection and diffusion boundary type: flux

When a flux has to be imposed through a boundary the condition to be applied is:

$$\vec{n} \cdot (c\vec{u} - D\nabla c) = N_0 \quad (36)$$

where  $\vec{n}$  is the unit normal vector to the surface.

### Convection and diffusion boundary type: insulation

This boundary condition typically applies at walls where you can assume that mass is not transported over the wall. It is a particular case of the previous case.

$$\vec{n} \cdot (c\vec{u} - D\nabla c) = 0 \quad (37)$$

### Convection and diffusion boundary type: convective flux

This boundary condition typically applies at outlets, where you can assume that mass is transported out of the domain by convection only.

$$\vec{n} \cdot (-D\nabla c) = 0 \quad (38)$$

However it's important to remember that modelling a real system means always approximate it at best of possibilities. A good model of a microsystems is composed always by more than one set of PDEs, but as the number of equations increases the computing power required may became unsustainable. In the major of case it's possible to reach a compromise between the model accuracy and computing degree.

## References

- [1] K. Ohno, K. Tachikawa, A. Manz, Microfluidics: Applications for analytical purposes in chemistry and biochemistry, *Electrophoresis*. 29 (2008) 4443-4453.
- [2] D.J. Beebe, G.A. Mensing, G.M. Walker, Physics and applications of microfluidics in biology, *Annu. Rev. Biomed. Eng.* 4 (2002) 261-286.
- [3] D.L. Polla, BioMEMS applications in medicine, in: *Proceedings of 2001 International Symposium on Micromechatronics and Human Science, 2001. MHS 2001, IEEE, 2001*: pp. 13-15.
- [4] I.A. Grimaldi, A.D.G. Del Mauro, G. Nenna, F. Loffredo, C. Minarini, F. Villani, Inkjet Etching of Polymer Surfaces to Manufacture Microstructures for OLED Applications, *AIP Conf. Proc.* 1255 (2010) 104-106.
- [5] D. Soltman, V. Subramanian, Inkjet-Printed Line Morphologies and Temperature Control of the Coffee Ring Effect, *Langmuir*. 24 (2008) 2224-2231.
- [6] H. Bruus, *Theoretical Microfluidics*, Oxford University Press, USA, 2007.
- [7] J.C.T. Eijkel, A. van den Berg, Nanofluidics: what is it and what can we expect from it?, *Microfluid Nanofluid.* 1 (2005) 249-267.
- [8] M. Gad-el-Hak, The Fluid Mechanics of Microdevices---The Freeman Scholar Lecture, *J. Fluids Eng.* 121 (1999) 5-33.
- [9] T.M. Squires, S.R. Quake, Microfluidics: Fluid physics at the nanoliter scale, *Rev. Mod. Phys.* 77 (2005) 977.
- [10] B.H. Weigl, R.L. Bardell, C.R. Cabrera, Lab-on-a-chip for drug development, *Advanced Drug Delivery Reviews.* 55 (2003) 349-377.
- [11] K. Malek, M.-O. Coppens, Knudsen self- and Fickian diffusion in rough nanoporous media, *J. Chem. Phys.* 119 (2003) 2801.
- [12] A.E. Kamholz, B.H. Weigl, B.A. Finlayson, P. Yager, Quantitative analysis of molecular interaction in a microfluidic channel: the T-sensor, *Anal. Chem.* 71 (1999) 5340-5347.
- [13] N.-T. Nguyen, Z. Wu, Micromixers—a review, *Journal of Micromechanics and Microengineering.* 15 (2005) R1-R16.
- [14] A.D. Stroock, S.K.W. Dertinger, A. Ajdari, I. Mezić, H.A. Stone, G.M. Whitesides, Chaotic Mixer for Microchannels, *Science.* 295 (2002) 647 -651.
- [15] COMSOL, FEMLAB 3 users guide, January, 2003.



## Chapter 2

### Microfabrication techniques

The current techniques for fabricating microfluidic devices include micro-machining, soft lithography, etc. This chapter starts with a small introduction to these fabrication methods and then carries on in depth about soft-lithography, a convenient non-photolithographic approach based for micro- and nano-fabrication extensively used in microfluidics. This chapter also presents fabrication methods of porous silicon. Porous silicon is an ideal material as transducer for biosensing due to its sponge-like morphology characterized by a high specific surface area that assures an efficient and rapid interaction with the species to detect; its fabrication process is compatible with microelectronics, which makes it an important material in lab-on-a-chip applications. Porous silicon based devices have been presented in the following book chapter:

- Ilaria Rea, Emanuele Orabona, Ivo Rendina, and Luca De Stefano (2011). Porous Silicon Integrated Photonic Devices for Biochemical Optical Sensing, Crystalline Silicon - Properties and Uses, Sukumar Basu (Ed.), ISBN: 978-953-307-587-7, InTech.

#### 2.1 Fabrication methods in microfluidics

Microfluidics technology uses all the microfabrication techniques developed and successfully applied, for example in microelectromechanical systems (MEMS) realization, by microelectronics industry. The first devices were fabricated in silicon and glass, largely used in microprocessors and MEMS devices, but now these materials have been largely displaced by plastics [1]. In the analyses of biological samples in water, glass and silicon devices are usually unnecessary or inappropriate. Silicon, in

particular, is expensive, and opaque to visible and ultraviolet light, so it cannot be used with conventional optical methods of detection. There are a large number of possible materials and processes that can be used in fabricating microfluidic circuits, including hot embossing of PMMA [2]; femtosecond irradiation and chemical etching of glass [3]; polymerisation of photoresist [4] and photo-definable PDMS [5], and so on.

In this chapter, all the steps needed for the fabrication of microfluidic chips in polydimethylsiloxane (PDMS) are presented. Shortly, the fabrication process of PDMS-based chips is called soft lithography where liquid, unpolymerized PDMS is poured onto a hard master mould, cured in an oven, and then peeled and sealed to a substrate. The whole process is fast, cheaper than silicon technology, and can be made many times with the same mould. The ability to bond PDMS to a wide range of substrates, including silicon and glass, makes it a practical optional material in a research laboratory for its easy handling, and its optical transparency makes it ideal in a wide range of settings. Nevertheless, PDMS chips are not so much used in industrial applications, mainly due to their lack of robustness and the limited scalability.

### **2.2 Soft lithography techniques**

Soft lithography, pioneered particularly by G.M. Whitesides and co-workers, is a group of fabrication methods concerned with forming structures with feature sizes generally on the micrometre scale. It provides fast methods for realising microfluidic chips, using a simple replica moulding process from a hard master. Once a mould has been realized, one can use it repeatedly to form many consecutive identical chips. Soft lithography techniques are a convenient, straightforward to apply, accessible to a wide range of users, and low-cost non-photolithographic approach based for micro- and nano-fabrication. These methods are based principally on the creation of an elastomeric block with patterned relief structures on its surface and on its possibility to use it to generate patterns and structures with feature sizes ranging from 30 nm to 100  $\mu\text{m}$ . Some soft lithography techniques are: microcontact printing ( $\mu\text{CP}$ ) [6], replica molding (REM)

[7], microtransfer molding ( $\mu$ TM) [8], micromolding in capillaries (MIMIC) [9], and solvent-assisted micromolding (SAMIM) [10].

The soft lithographic techniques offer immediate advantages in a number of applications: for example, patterning on scales  $<100$  nm, patterning on nonplanar surfaces, patterning of solid materials other than photoresists, patterning of liquid materials, patterning of surface functionalities, patterning over large areas, and formation of three-dimensional microstructures and systems. Table 4 compares the pros and cons of conventional photolithography and soft lithography.

|   | <b>Photolithography</b>           | <b>Soft Lithography</b>                                  |
|---|-----------------------------------|--|
| Definition of patterns                        | Rigid photomask                   | Elastomeric stamp or mould                               |
| Materials that can be patterned directly      | Photoresists                      | Photoresists   |
|   | SAMs on Au and SiO <sub>2</sub>   | SAMs on Au, Ag, Cu, GaAs, Al, Pd, and SiO <sub>2</sub>   |
|   |                                   | Precursor polymers                                       |
|   |                                   | Polymer beads  |
|   |                                   | Conducting polymers                                      |
|   |                                   | Colloidal materials                                      |
|   |                                   | Sol-gel materials  |
|   |                                   | Organic and inorganic salts                              |
|   |                                   | Biological macromolecules                                |
| Surfaces and structures that can be patterned | Planar surfaces<br>2-D structures | Both planar and nonplanar<br>Both 2-D and 3-D structures |
| Current limits to resolution                  | 100 nm                            | From 30 nm to 1 $\mu$ m                                  |

Table 4 Comparison between photolithography and soft lithography [11]

Soft lithography and its related technologies represent a different approach to micropatterning. The techniques of soft lithography complement those of photolithography and extend micropatterning into dimensions, materials, and

geometries to which photolithography cannot, in practice, be applied. The most famous and most important technique for microfluidics is the replica moulding technique. The standard soft lithography replica molding procedure can be summarized as follow:

1. Chip scheme is drawn on a computer, representing the fluidic circuit to be transferred to PDMS;
2. The design is transferred to a monochrome mask;
3. A master mould is formed in photosensitive epoxy (SU8) by photolithography using the photomask;
4. PDMS is cast from the master mould.

Cured PDMS is cut into chips, fluid inlets are punched in, and the device is bonded to a suitable substrate.

Before detailing the fabrication procedures for microfluidic chips, the chemistry and physical properties of PDMS are reviewed in the following.

### 2.2.1 Materials characteristics

#### Polydimethylsiloxane - PDMS

PDMS is available commercially from several companies but the most famous is the silicone elastomer kit from Dow Corning called Sylgard 184, containing a base and a curing agent which, once mixed, polymerize to form PDMS. The key chemical constituents are two and they are showed in Figure 13. Both components of the kit contain siloxane oligomers terminated with vinyl groups (Figure 13a). The curing agent also includes cross-linking siloxane oligomers (Figure 13b), which each contain at least three silicon-hydride bonds (Si-H). The base includes a platinum-based catalyst that cures the elastomer by an organometallic cross-linking reaction. When the base and the curing agent are mixed together, hydrosilation takes place between the vinyl (SiCH = CH<sub>2</sub>) and hydrosilane (SiH) groups of the copolymer pre-cursors, forming Si – CH<sub>2</sub> – CH<sub>2</sub> – Si linkages (see Figure 14). The hydrosilane groups provide multiple reaction sites, giving rise to three-dimensional cross-linking.

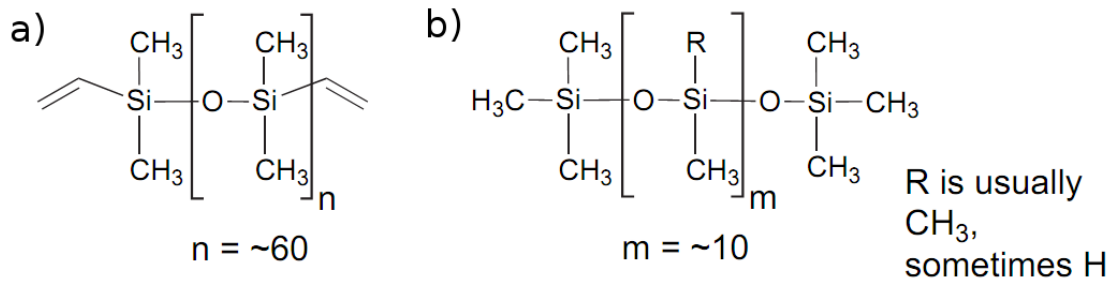


Figure 13 Key PDMS pre-cursors, where (a) is a vinyl-terminated siloxane oligomer and (b) is a shorter, partially hydrosilane-terminated siloxane oligomer. The base contains (a) and a platinum complex, whereas the curing agent contains (a) and (b). Each methyl-hydrosiloxane oligomer contains a minimum of three hydrosilane (Si-H) groups available as hydrosilation reaction sites [12].

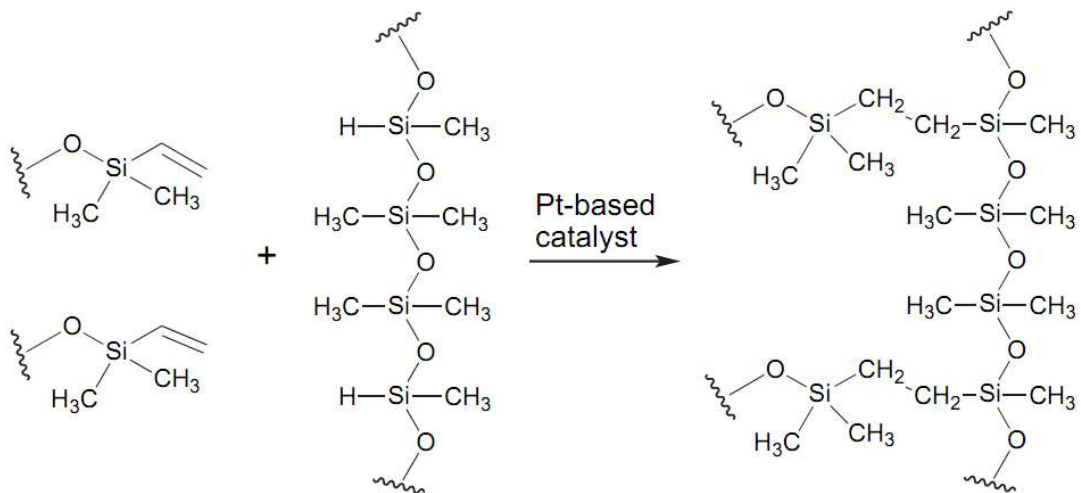


Figure 14 Hydrosilation reactions between dimethylsiloxane and methylhydrosiloxane copolymers to form cross-linked polydimethylsiloxane silicone elastomer. The relative ratios of the pre-cursors determine the rigidity of the final elastomer. The reaction does not produce any collateral-products and can be accelerated by heat [12].

One advantage of this type of reaction is that no waste products are generated. Changing the curing agent-to-base ratio alters the properties of the resulting cured elastomer: as the ratio of curing agent-to-base increases, more rigid elastomer results [13,14]. In

Table 5 are exposed the density and Young's modulus of PDMS with different mixing ratio.

| <b>Mixing ratio</b><br><b>curing agent : base</b> | <b>Density</b><br><b>(kg/m<sup>3</sup>)</b> | <b>Young's modulus</b><br><b>(Pa)</b> |
|---|---|---------------------------------------|
| 1:5   | $9.52 \cdot 10^{-2}$                        | $8.68 \cdot 10^5$                     |
| 1:7.5   | $9.18 \cdot 10^{-2}$                        | $8.26 \cdot 10^5$                     |
| 1:10  | $9.20 \cdot 10^{-2}$                        | $7.50 \cdot 10^5$                     |
| 1:12.5  | $9.27 \cdot 10^{-2}$                        | $5.49 \cdot 10^5$                     |
| 1:15  | $9.87 \cdot 10^{-2}$                        | $3.60 \cdot 10^5$                     |

Table 5 Density and Young's modulus of PDMS under various mixing ratio [13].

The properties of PDMS are surprisingly close to that could be obtained from glass and plastic. The cross-linking of many of these polymer chains makes a structure that is flexible and reversibly deformable. Table 6 summarizes the physical properties of cured PDMS. Many of the properties exhibited by PDMS are very desirable for fabricating microfluidic chips. Increased temperature will accelerate the cross-linking reaction. It is curable from less than room temperature to over 150°C. Sylgard 184 also has temperature dependant shrinkage as showed in Figure 15. For example curing at 140°C (~15 min) will make the stamp shrink almost exactly 3% [16]. The temperature-dependent curing time allows it to be easily mixed, poured onto a mould and cured through heating. Being elastomeric and reversibly deformable, it can be peeled from delicate mould features without damaging the mould or itself, creating a negative cast in PDMS of the mould. Features of the order of microns can be easily obtained through this replica moulding method. PDMS is non-toxic, making it a good choice for containing biological samples. It is also resistant to temperatures in excess of 200°C and to ethanol, making it easy to sterilize by either for biological applications.

| Property     | Characteristic  | Consequence   |
|--------------|---|---|
| Optical      | Transparent;<br>UV cut-off = 240nm  | Optical detection from 240 to 1100nm  |
| Electrical   | Insulating;<br>breakdown voltage = $2 \times 10^7$ V/m  | Allows embedded electrical circuits;<br>Electrophoresis possible on contained fluid   |
| Mechanical   | Elastomeric;<br>Young's modulus typically 750 kPa   | Conforms to surfaces;<br>Facilitates release from moulds;   |
| Thermal      | Insulator;<br>Thermal conductivity 0.2 W/(m·K);<br>Thermal expansion coeff. 310 $\mu\text{m}/(\text{m}^\circ\text{C})$ ;<br>Can withstand 200°C | Does not allow dissipation of optical absorption heating, or electrophoretic resistive heating;<br>Can be autoclaved for sterilisation  |
| Interfacial  | Low surface free energy 20 erg/cm <sup>2</sup>  | Releases from mould easily;<br>Can be reversibly sealed to materials  |
| Permeability | Impermeable to liquid water<br>Permeable to gases and non-polar solvents  | Contain aqueous solutions in channels; allows gas transport through material bulk;<br>Incompatible with many organic solvents   |
| Reactivity   | Inert<br>Oxidised by plasma exposure  | Unreactive toward most reagents, including ethanol;<br>Surface can be etched;<br>Can be modified to be hydrophilic and also reactive toward silanes;<br>Can be permanently bonded |
| Toxicity     | Non toxic   | Can be implanted in vivo;<br>Supports mammalian cell cultures.  |

Table 6 Physical properties of PDMS [15].

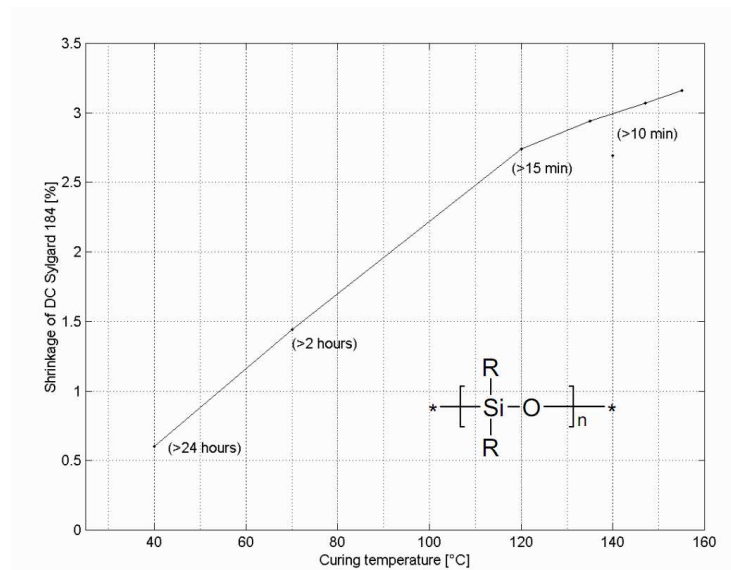


Figure 15 Percentage of shrinkage for Sylgard 184 vs curing temperature [16].

### SU8 photoresist

SU8 (Figure 16) is a high contrast, epoxy based photoresist designed for micromachining and other microelectronic applications, where a thick, chemically and thermally stable image is desired.

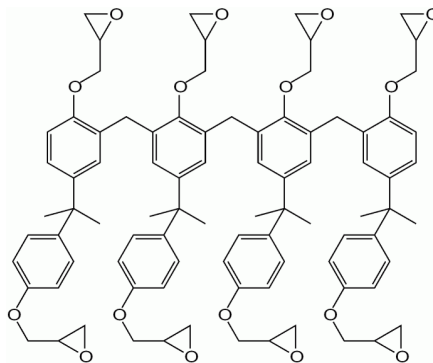


Figure 16 Chemical composition of the main constituent in SU8 photoepoxy. Eight oligomers are available for a high degree of crosslinking upon photoexposure.

SU8 is available in different viscosities, thus enabling a wide range of thicknesses (0.5 to 650  $\mu\text{m}$  with a single coat process [17]) that can be obtained, through spin coating on a substrate. SU8 has excellent imaging characteristics and is capable of producing very

high aspect ratio structures. SU8 is best suited for applications where it is casted, cured and left permanently on the device [18]. Upon UV exposure, cross-linking proceeds in two steps: formation of a strong acid during the exposure step, followed by acid-catalyzed, thermally driven epoxy cross-linking during the post exposure bake step. The substrate covered with photoresist, is spun at a rate of typically 1000-5000 rpm for 30 seconds. Part of the solvent is evaporated off during this spin cycle. The thickness of the photoresist layer is inversely proportional to the spin speed. SU8 is designed to obtain thickness values from 0.5 $\mu\text{m}$  to 650 $\mu\text{m}$ , some formulations are extremely viscous and require special attention compared to other photoresists. The most important issue is the formation of an edge bead to the silicon wafer. The edge bead is resist material accumulate at the edge of the substrate and can be a problem where high vertical resolution is desired, as it prevents the photomask being placed in close proximity to the sample, thus allowing loss of resolution due to diffraction. The best method for its removal was found to be simply dissolving it with acetone spraying carefully with a syringe on to the substrate edges. One of the best substrates, is silicon: it's possible to obtain excellent adhesion between SU8 and silicon. To obtain good adhesion between the SU8 and the silicon, it is essential that the substrate is cleaned by the so-called "piranha solution". A "piranha solution" is formed by mixing sulphuric acid ( $\text{H}_2\text{SO}_4$ ) and hydrogen peroxide ( $\text{H}_2\text{O}_2$ ), in a ratio of typically 3:1. Since the mixture is a strong oxidizer, it will remove most of the organic matter, and it will also hydroxylate the surfaces (-OH groups), making them hydrophilic. In order to minimize the adhesion and enhance the removal of PDMS from the mould, it can be silanized exposing it to trimethylchlorosilane (TMCS) vapours for few minutes [7]. In Figure 17 is illustrated the surface energy decreasing of a silicon substrate with native oxide on its surface before and after the TMCS vapours treatment.

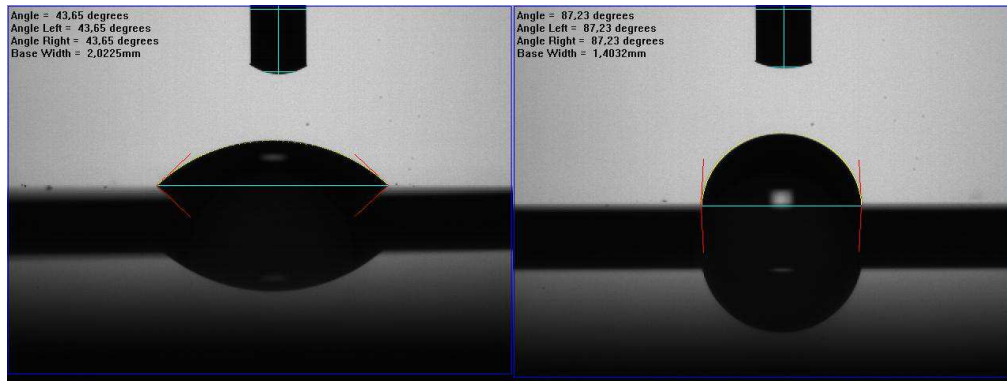


Figure 17 Contact angle of a piranha cleaned silicon substrate before and after the exposition to trimethylchlorosilane vapours for 10 minutes in a closed reactor.

## 2.2.2 Replica molding technique

In order to produce PDMS chips containing microfluidic channels, a mould has to be firstly realized. One way is making moulds by patterning Microchem SU8 epoxy-based photoresist on a silicon substrate using standard photolithography techniques. The basic procedure followed for producing a mould illustrated in Figure 18 is as follows:

1. **Spin Coating:** SU8 is spin coated onto the substrate to the desired thickness;
2. **Soft baking:** the photoresist is warmed on a hotplate to evaporate the solvent;
3. **Exposing:** SU8 is exposed with UV light to photomask patterns in a mask aligner;
4. **Post bake:** the photoresist is again warmed on a hotplate to cross-link and harden the exposed regions;
5. **Development:** solvent is used to dissolve unexposed regions, leaving a relief structure of SU8 of the transparent regions in the photomask pattern;
6. **Silanization:** mould is coated with silanizer to enhance the removal of PDMS.

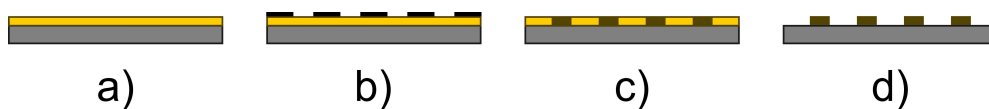


Figure 18 Scheme process to realize a mould using SU-8 photoresist.

As well described by many texts [16,19], the steps to mould a stamp in PDMS from a template (Figure 19) can be summarized as:

1. **Preparation of solution:** one part of curing agent and ten parts of base (by volume) have to be mixed rather carefully for at least a few minutes. A small error in the amounts will not affect the final result though.
2. **Degas of solution:** after the mixing, the silicone mixture full of air bubbles needs degassing under vacuum. During the degassing the silicone expands and starts to look like foam. When the step is finished the silicone is completely clear and transparent.
3. **Dispense the solution:** dispensing the silicone on to the template avoiding trapping air in the process. It must be leaved for a minute in order to get a flatter top surface. Stamps thickness can range from 0.1 to 5mm or more.
4. **Curing:** Sylgard 184 is heat cured. It is curable from less than room temperature to over 150°C.
5. **Peal off:** the final step is to peel off the stamp from the template starting by releasing all borders and then to continue at low speed.

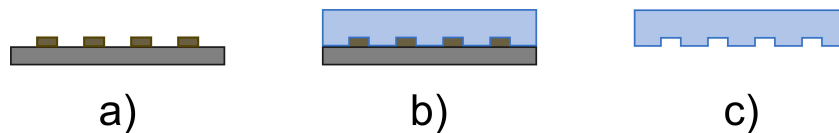


Figure 19 Scheme process to mould a stamp in PDMS.

### 2.2.3 Surface activation processes

The moulded PDMS can be sealed reversibly to itself or many other materials through van der Waals bonding, or sealed irreversibly to many materials through a short exposure to oxygen plasma.

#### Irreversible Bonding: Plasma-oxygen process

One technique most commonly used for getting irreversible seals is by exposing the surfaces to oxygen plasma. The samples are placed in a vacuum chamber and oxygen is

introduced. Microwaves dissociate the oxygen molecules to single atoms that react with the surfaces of the samples [20]. Silicon based material with Si-CH<sub>3</sub> groups react to form Si-OH groups (silanol groups) on the surface. As the silanol groups are polar in nature, they make the exposed surface highly hydrophilic and this can be observed by a drastic change in the water contact angle (Figure 20).

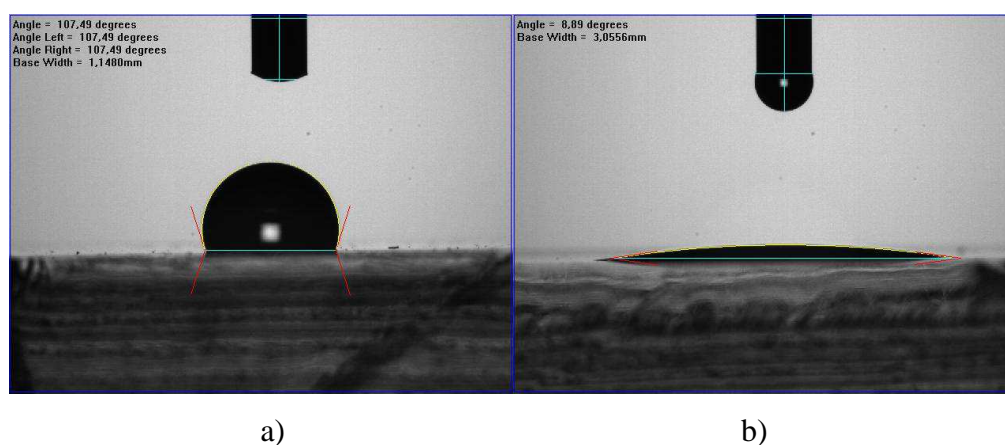


Figure 20 Water contact angle on PDMS a) before and b) after the plasma oxygen process.

The hydrophobic surface of PDMS (107°) turns to hydrophilic surface (9°) after the exposition to plasma oxygen for ten seconds. When two exposed surfaces are pressed together, silanol groups naturally form Si-O-Si plus water in a condensation reaction (Figure 21). These covalent bonds form the basis of a tight irreversible seal between layers. Typically such seals can withstand 30-50psi of air pressure and are practically inseparable. Silicon based materials can therefore be covalently bonded together after oxygen plasma treatment. Further, the hydroxyl part in the silanol group makes the surfaces hydrophilic and wetting by hydrophilic biological samples is facilitated but the effect is temporary and it recovers hydrophobicity after less than an hour [21]. However this time can be relaxed by the use of a polar solvent, such as methanol [22]. Covering the exposed surface by the solvent, immediately after exposure, has two effects: it prevents instantaneous bonding of the two layers when brought into contact, and it lubricates the boundary allowing the two layers to be moved laterally relative to one another.

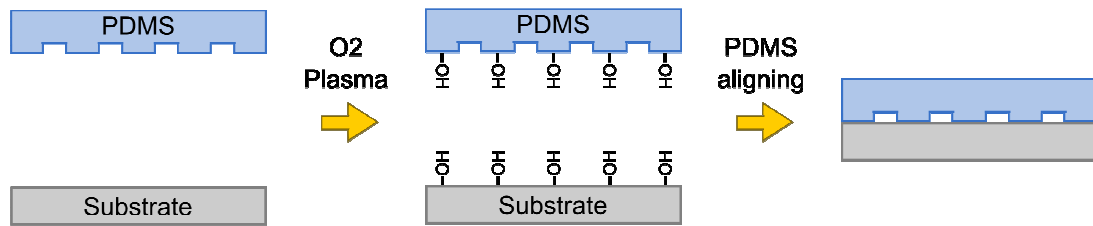


Figure 21 General scheme of irreversible bonding by plasma oxygen process.

Once correctly positioned, the composite is placed in an oven or hotplate, evaporating the solvent and allowing the two surfaces to bond.

### Reversible bonding: van der Waals forces

A simpler temporary bonding than the previous one is possible; it can be desirable in simpler fluidics applications or surface patterning. PDMS, being flexible, will conform to smooth surfaces and form van der Waals bonds. Such bonds are strong enough to contain a fluid, but not to withstand the positive pressures required to drive a fluid flow [23]. However, generating a negative pressure on a fluid outlet, by pulling up by a syringe for example, the fluid can pass through the embedded channels, without separating the PDMS from the substrate.

## 2.3 Photographic procedure for masks fabrication

PDMS is very cheap as material, but the related instrumentation can be very expensive: main costs are due to the realization of Chromium masks. Many solutions has been proposed to bypass this step, typically by UV laser writing coupled by motorized stages [24–26], however, the mask approach results the most simple and practical method. Deng et al. [27] proposed a new method for the fabrication of cheap photomasks using photographic films: CAD files are first printed ten times bigger than real size onto paper using an office printer with resolution of 1200 dots/in, and then reduced to right dimensions onto 35-mm films. After development these photographic films can be used as photomasks in contact photolithography. These masks do not have the resolution to

be suitable for the fabrication of complex microelectronic devices, but they are well suited for many medium/low resolution applications such as microfluidics. After this work, many others have been proposed [28,29] to improve the performance and to investigate possible applications. A practical method for a fine control in the reduction factor from paper to photographic film is based on a photographic enlarger (Durst C35) used in reverse mode in a darkroom. Its use is schematized in Figure 22.

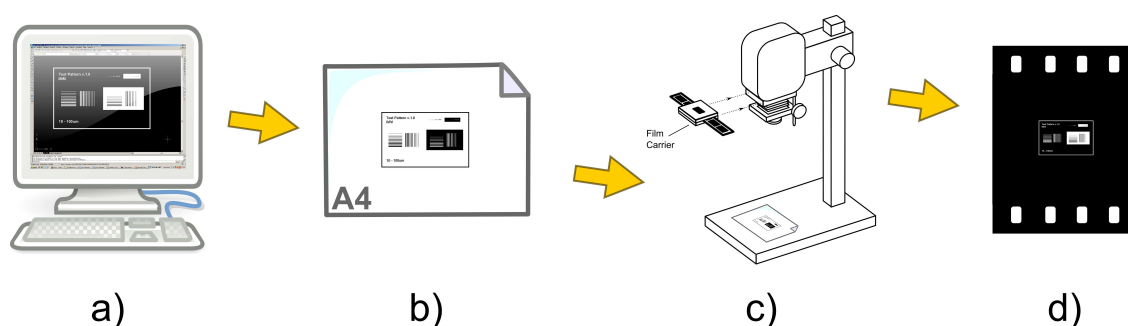


Figure 22 Scheme process to realize a mask with the photographic reduction technique: a) Cad designing of mask; b) Printing 10X on a4 paper; c) optical reduction on to photographic film; d) final result.

An enlarger is a specialized transparency projector used to produce photographic prints from film or glass negatives using the gelatin-silver process. It consists of a light source, normally an incandescent light bulb, a holder for the negative and a specialised lens for projection. The light passes through a film holder, which holds a photographic negative or transparency, having been previously exposed in a camera and developed. This instrument has been used in reverse mode, impressing the negative (Maco Genius Print Film) in the holder with the microfluidic channels printed on a paper. An enlargement factor of 10 has been chosen for the realization of masks, an illumination system composed by two 100W incandescent lamp oriented at  $45^\circ$  provide a quite uniform illumination on the printed paper. Then the reflected light impresses negative film creating a negative image of the microfluidic scheme. The film is a half tones without gray scale, and orthochromatic, which means that is sensitive to only blue and green light, and thus can be processed in darkroom with a red safelight. To obtain black enough zone to use it as a mask for UV light, it has been necessary to overexpose the

photographic film for 30 seconds. These photographic masks can be used with an UV light box avoiding the use of an expensive mask aligner. UV light boxes are normally used for printed circuit boards and are simply composed by UV lamps without any light collimation system. A test pattern (Figure 23a), containing lines and dots in black and white with dimensions from  $10\mu\text{m}$  to  $100\mu\text{m}$ , has been designed and transferred onto photographic film (Figure 23b) to optimize the process parameter.

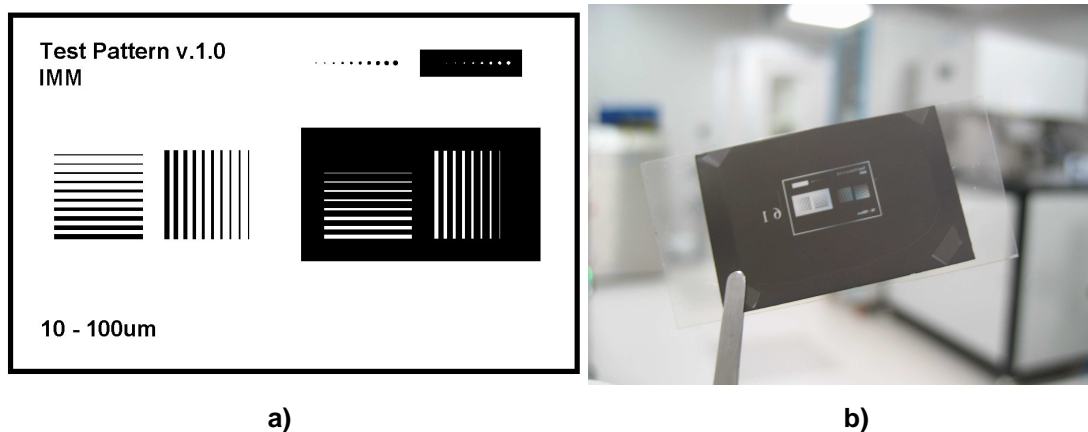


Figure 23 a) test pattern used for optimize the reduction parameter. It contains lines and dots in black and white with dimensions from  $10\mu\text{m}$  to  $100\mu\text{m}$ . b) photo of the impressed photographic film.

Dark (exposed) regions are due to the presence of small particles of a metallic silver, or dye clouds (see Figure 24a), developed from silver halide that have received enough photons. It's possible to observe the film grain that is obviously absent in classical photolithographic masks. It has an average thickness of  $410\text{nm}$  and a roughness of  $120\text{nm}$  (see Figure 24b). However in transparent regions where silver is absent, black dots with a diameter of  $1.8\pm 1.4\mu\text{m}$  are found. These defects that shall be transferred by mask aligner on to the photoresist are ignored from the UV box: the uncollimated light from this device erases all micron and submicron features present on the mask. This is a disadvantage for high resolution photolithography but is an advantage for low resolution applications.

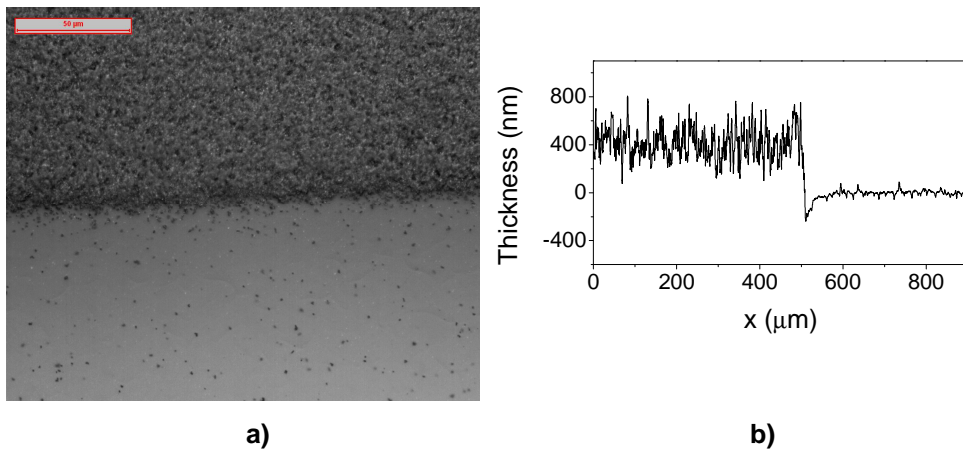


Figure 24 a) Optical photograph and b) thickness profiles measured by the profilometer of the transition from dark exposed region to transparent unexposed region on the photographic film.

In the photographic mask the edge are not so straight and well defined and there is a transition region of few microns from dark to transparent region(Figure 25a); however, as showed in Figure 25b, the impressed photoresist edges are quite well defined and it is not present any edge roughness. Then the combination of photographic masks with an UV light box can be a powerful tool for the realization of microfluidic devices.

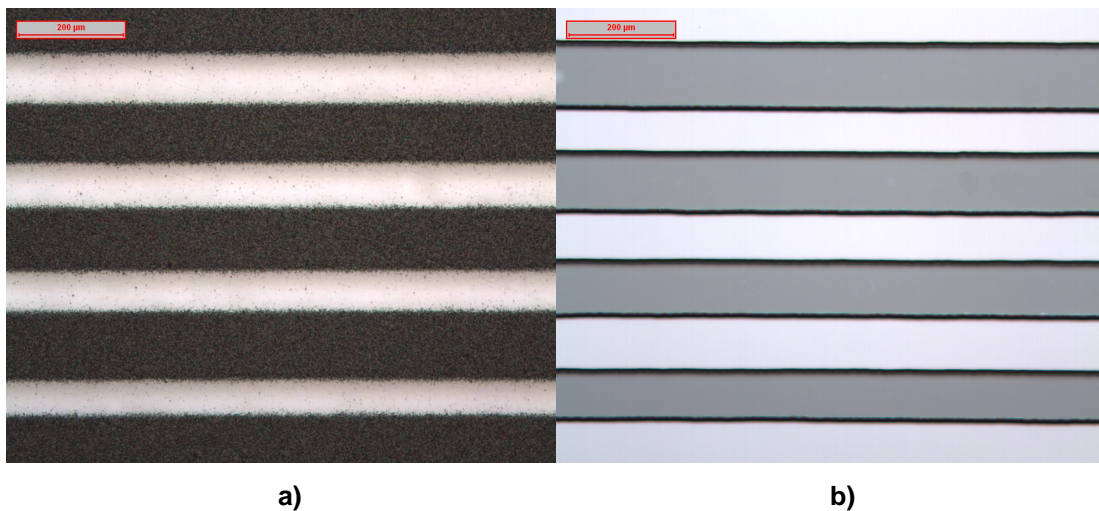


Figure 25 a) photographic mask with alternating dark and transparent regions and b) relative substrate with impressed photoresist (SU8, thickness: 10μm).

## 2.4 Porous silicon fabrication

Porous silicon (PSi) was discovered by accident in 1956 at Bell Labs, USA, during a study on the electropolishing of crystalline silicon in an HF-based solution. They observed under several conditions a crude product in the form of thick black, red or brown film on the surface of the material [30]. In the following years, after a study of Leigh Canham on an efficient tunable room temperature light output from the material [31], thousands of papers were published on porous silicon and its potential applications in microelectronics, optoelectronic devices, chemical and biological sensing [32]. The PSi is an ideal material as transducer for biosensing due to its sponge-like morphology characterized by a specific surface area of  $100\text{m}^2/\text{cm}^3$  that assures an efficient and rapid interaction with the species to detect. Another advantage of PSi is its complete compatibility with fabrication processes of microelectronics, which makes it an important material in lab-on-a-chip application. PSi can be simply described as a network of air holes in a silicon matrix. In most cases, the porous silicon structure is formed by electrochemical dissolution of doped crystalline silicon wafers in hydrofluoric acid (HF) based solution. The scheme of the cell used for the electrochemical etching is illustrated in Figure 26.

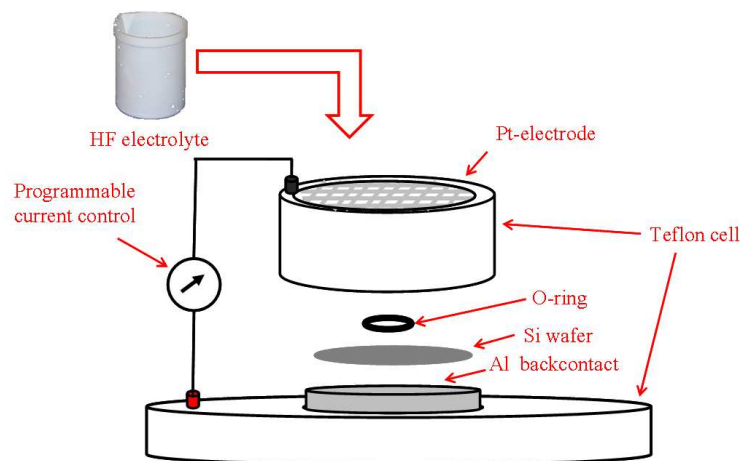


Figure 26 Electrochemical etching setup.

In this type of cell the silicon wafer is the anode; it is placed in back-side contact on an aluminium plate while the front side is sealed with an o-ring and exposed to the anodising electrolyte. The cathode is made of platinum. In the anodic I-V curve of silicon in HF based solution, shown in Figure 27, it's possible to distinguish three regions (called A, B, C). Pore formation takes place in region A. At anodic overpotentials in excess of the current "peak," region C, silicon electropolishes. At intermediate overpotentials, region B, a "transition" zone exists where pore formation and electropolishing compete for control over the surface morphology. The resulting structure within this region is generally porous in nature but the pore diameters increase rapidly as the electropolishing potential is approached.

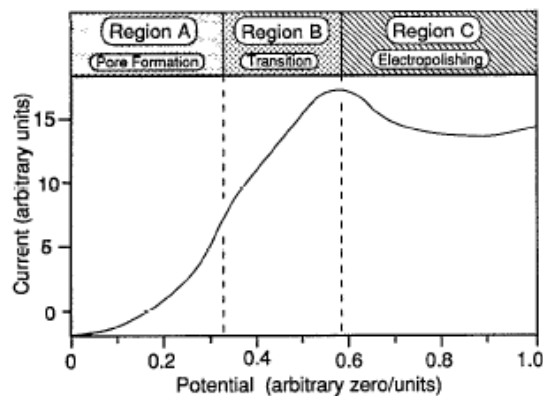


Figure 27 Anodic I-V curve for silicon in HF. In the region A pore formation occurs. In region C there is the silicon electropolishing. The region B is a transition zone where pore formation and electropolishing compete [33].

The PSi shows a great variety of morphologies dependent on the doping type and level of the silicon substrate and the electrochemical etching parameters. Usually for a given substrate and electrolyte, only one type of pore structure can be obtained. The IUPAC (International Union of Pure and Applied Chemistry) guidelines define ranges of pore sizes that exhibit characteristic absorption properties: pores characterized by a diameter  $\leq 2\text{nm}$  define microporous silicon; for sizes in the range 2-50 nm the PSi is mesoporous; pores diameters  $> 50\text{ nm}$  are typical of macroporous silicon.

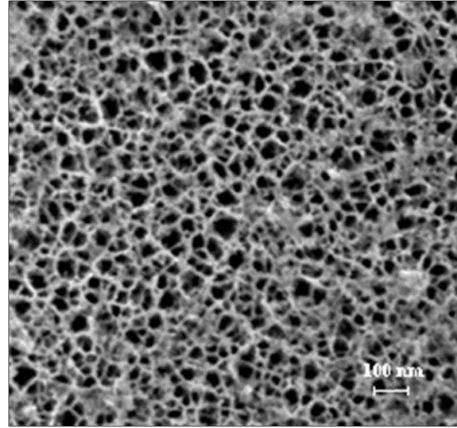


Figure 28 Scanning electron microscope image of a porous silicon surface.

The porosity is defined as the fraction of void within the porous layer. And it is given by the equation:

$$P = \frac{V_{void}}{V_{PSi} + V_{void}} \quad (39)$$

The average dielectric constant of a porous silicon layer is linked to the porosity by the Bruggeman effective medium approximation (EMA) [34]

$$(1-P) \left( \frac{\epsilon_{Si} - \epsilon_{PSi}}{\epsilon_{Si} + 2\epsilon_{PSi}} \right) + P \left( \frac{\epsilon_{void} - \epsilon_{PSi}}{\epsilon_{void} + 2\epsilon_{PSi}} \right) = 0 \quad (40)$$

where  $\epsilon_{Si}$ ,  $\epsilon_{PSi}$ , and  $\epsilon_{void}$  are the dielectric constants of silicon, porous silicon and void, respectively. This approximation is acceptable until the size of the PSi pores is much smaller than the wavelengths of incidence light in the near IR-UV regions; in this range, the electromagnetic radiation does not distinguish between silicon and void, and it is possible to treat the PSi as an homogeneous medium. Figure 29 shows the dependence of the PSi refractive index on porosity given by the Bruggeman model.

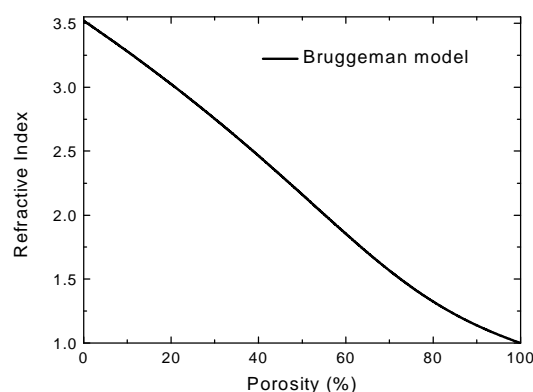


Figure 29 Dependence of the PSi refractive index on the porosity given by the Bruggeman effective medium approximation [32].

### 2.4.1 Porous silicon as an optical transducer

A biosensor is an analytical devices incorporating a biological material (e.g. tissue, microorganism, enzyme, nucleic acid, antibody, etc.) or a biomimic, intimately associated with, or integrated within, a physicochemical transducer or transducing microsystem which may be optical, electrochemical, thermometric, piezoelectric or magnetic. They can be used in many applications such as clinical diagnostics, environmental monitoring, and food quality control. Among others, photonic sensing devices offer specific features which make them very attractive:

- optical measurements are not invasive and can be used in many environments;
- opto-instrumentation is immune to electromagnetic interferences so that they are highly requested for applications such as *in vivo* monitoring inside a patient body.
- Moreover, optical sensors are generally characterized by very short analysis time and high sensitivity.

The optical detection principles are based either on fluorescence-labelled systems or on label free direct optical monitoring. Fluorescence detection has been the main approach in medical diagnostic, biotechnology and drug discovery for a long time. However,

these labelling strategies often alter the characteristics and natural activities of the query molecules. Moreover, the labelling procedure is laborious and lengthy. In contrast to the label-based techniques, the label-free detection methods depend on the measurement of a property of the query itself, such as mass or dielectric property. Label-free techniques avoid interference due to the tagging molecules, and determine reaction kinetics of biomolecular interactions in real-time [35].

The PSi is an ideal material as optical biosensor transducer and it allows the label-free detection; its principal advantages are:

- low-cost material and fabrication process;
- large specific surface area ( $\sim 500 \text{ m}^2/\text{cm}^3$ );
- rapidly and effectively interaction with chemical species;
- evident changes in several physical properties usable for label-free sensing (reflectivity, photoluminescence, electrical conductivity, optical waveguiding...);
- easy integration in hybrid systems (MEMS, MOEMS,  $\mu$ TAS, lab-on-chip etc...);
- compatibility with microelectronic technologies;
- chemically modification of its surface possible to enhance selectivity in analyte detection.

The label-free sensing mechanism used is based on the change of the PSi refractive index on exposure to the substances to be detected, due to their infiltration into the pores; the consequence of the refractive index variation is a change in the reflectivity/transmittivity spectrum of the devices.

Photonic structures as PSi resonant photonic structures as Fabry-Perot interferometers [36], Bragg reflectors [37], optical microcavities [38], and Thue-Morse sequences [39] have been realized exploiting intensively multilayer fabrication capability. This is possible because the PSi fabrication process is self-stopping; an as etched PSi layer is depleted of holes and any further etching only occurs at the pores tips [40]. The refractive index modulation of a PSi multilayered structure can be realized by alternating different proper currents densities during the electrochemical etching of crystalline silicon.

Bragg mirror optical structures have been realized alternating periodically layers of low and high porosity values which correspond to high ( $n_H$ ) and low ( $n_L$ ) refractive index. The related thicknesses must satisfy the relation  $2(n_H d_H + n_L d_L) = m\lambda_B$ , where  $m$  is the order of the Bragg condition (Figure 30a).

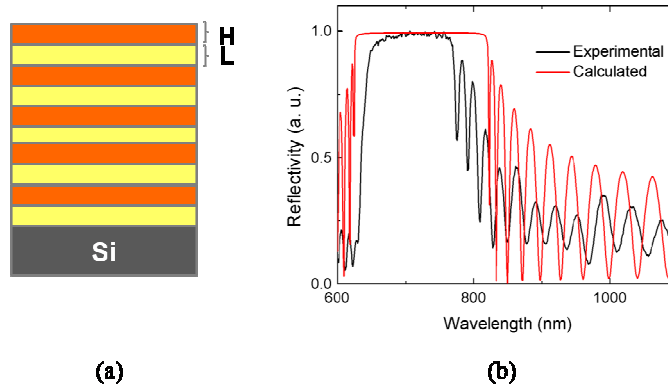


Figure 30 (a) Schematic section of a Bragg mirror. (b) Experimental (black line) and simulated (red line) normal incidence reflectivity spectrum from a Bragg mirror.

The reflectivity spectrum of a Bragg mirror is characterized by the presence of a stop band centred on the Bragg wavelength  $\lambda_B$  (Figure 30b) [41].

### 2.4.2 Porous silicon surface functionalization

The major drawback of the “as etched” PSi is its chemical instability: hydrogen-terminated PSi surface is slowly oxidized at room temperature by atmospheric oxygen, resulting in an increasing blue shift of the optical spectrum with time [42]. To stabilize it is usually completely thermal oxidized at 900°C. This process however induces a reduction in pore diameter and porosity. A key step in the fabrication of the PSi biosensor is the functionalization, which is a covalent immobilization of the bioprobe, of its surface with the biological probe in order to make the device selective for the species of interest. An example of functionalization scheme with a DNA-probe is reported in Figure 31.

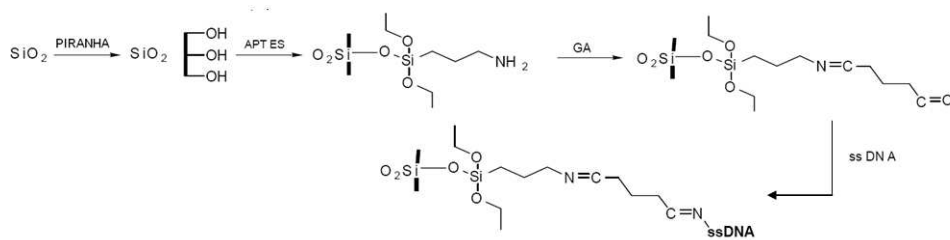


Figure 31 Scheme of the functionalization process of PSi surface with DNA probe single strand.

In this process the PSi surface, stabilized by means of a thermal oxidation at 900°C, was immersed in Piranha solution for 40 min in order to assure the formation of Si-OH bonds. The chip was rinsed with deionized water and dried in a nitrogen stream. Then, the PSi surface was silanized in a 5% solution of APTES (3-aminopropyltriethoxysilane) and anhydrous toluene for 30 min at room temperature. After the reaction time, the chip was washed twice in toluene to remove unlinked APTES, and baked at 100 °C for 10 min. The chip was thus immersed in a 2.5% glutaraldehyde (GA) solution in 20 mM HEPES buffer (pH 7.4) for 30 min. The GA reacts with the amino groups on the silanized surface and coats the internal surface of the pores with another thin layer of molecules. The PSi surface was incubated overnight with a 200 μM amino terminated DNA single strand solution (30 μL). From the optical point of view, each step cause a shift of the reflectivity spectrum: the thermal oxidation causes blue-shifts due to the lower value of the SiO<sub>2</sub> refractive index ( $n_{ox}=1.46$ ) with respect to the Si refractive index ( $n_{Si}=3.9$ ), on the contrary, the functionalization steps (APTES+GA, and DNA probe) produce red shifts due to an increasing of the average refractive index of the layers.

## 2.5 Porous silicon based microarray

The progress in sophisticated micro and nanotechnologies over the last 20 years has led to the development and diffusion of small integrated devices for chemical and biological analyses. Lab on a chip and micro-total-analysis systems are bright examples of what is nowadays more and more required both by industry and academic researches [43]. A

subset of these devices is represented by microarrays, originally developed for gene expression profiling [44]: these miniaturized platforms offer the advantages of very high throughput, cost-effective analysis with low consumption of reagents, and quite rapid operative times. Even if DNA microarrays are being rapidly superseded by next generation sequencing technologies in the industrial market, especially in massive parallel sequencing of large numbers of DNA fragments from complex samples or transcriptomes, they are still working-horses devices for small laboratory application in genomics, proteomics, pathogen detection, and also microbial ecology research [45]. From the historical point of view, DNA microarrays were developed utilizing different types of probes, depending on the specific field of investigation, such as oligonucleotides, complementary DNA, long sequences, directly spotted on the support surface, or even growth on it, with a density of sensitive elements from few tenths up to millions of probes. The first generation of microarrays required radioactive or fluorescent labelling, in both cases long, invasive, and costly procedures. To overcome the intrinsic limits of this technology, such as chromophores photobleaching and quenching, label-free optical methods, like surface plasmon resonance imaging, ellipsometry, and microfluidic assisted x-ray diffraction have been proposed. [46–49]. In general, DNA microarrays technology is undergoing significant changes by improving not only the signal detection but also the support materials, the functionalization procedures, the scanning methods, and, last but not least, the integration of microfluidic circuits with the standard devices.

A microarray of porous silicon Bragg reflectors on a crystalline silicon substrate has been realized using a technological process based on standard photolithography and electrochemical anodization of the silicon. The array density is of 170 elements / cm<sup>2</sup> and each element has a diameter of 200 μm. The porous silicon structures have been used as platform to immobilize an amino terminated DNA single strand probe. All fabrication steps have been monitored by spectroscopic optical reflectometry.

### 2.5.1 Fabrication process

To integrate PSi elements in a microarray, a proper technological process had to be designed. The silicon substrate was a highly doped p<sup>+</sup>-type wafer with a resistivity of 0.01 Ωcm, <100> oriented and 400 μm thick. Two different materials have been used as masking material during the electrochemical etching: Silicon nitride and SU8 photoresist. The process flow chart of the PSi μ-array fabrication using SU8 photoresist as a masking layer is schematized in Figure 32.

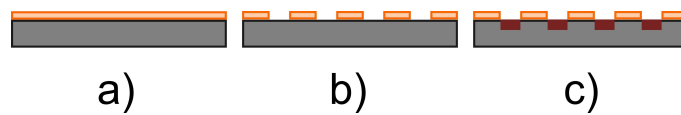


Figure 32 Technological steps of the PSi μ-array fabrication process using SU8 photoresist. a) SU8 photoresist spin coating; b) photolithographic process; c) local electrochemical etching of silicon.

The SU8 photoresist, 10 μm thick, was spin coated on the substrate (Figure 32a) and patterned by a standard photolithographic process (Figure 32b). Finally, the silicon wafer was electrochemically anodized in a HF-based solution (50 wt. % HF : ethanol = 1:1) in dark and at room temperature (Figure 19 (d)). The process steps are very few but to avoid stress during photolithography a long recipe with relaxation time has been adopted [50]. The result of the electrochemical etching is shown in Figure 33. An evident under-etching has been observed around the element; however the PSi region is uniform.

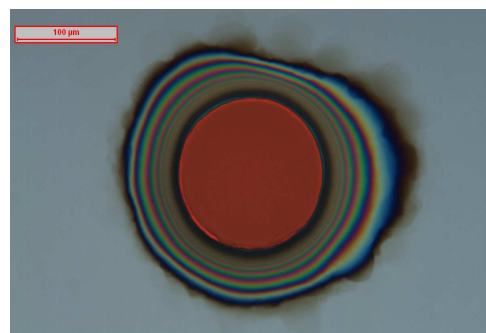


Figure 33 A porous silicon element realized masking the silicon with SU8 photoresist

Instead the process flow chart of the PSi  $\mu$ -array fabrication using silicon nitride as a masking layer is schematized in Figure 34.

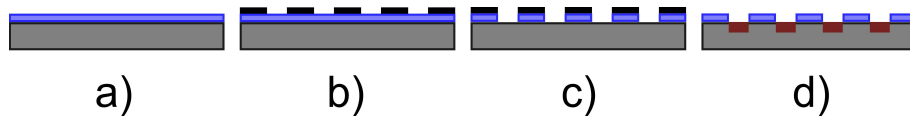


Figure 34 Technological steps of the PSi  $\mu$ -array fabrication process using silicon nitride. a) silicon nitride deposition by PECVD; b) photolithographic process; c) RIE etching of silicon nitride layer; d) local electrochemical etching of silicon.

The silicon nitride film, 1.6  $\mu\text{m}$  thick, was deposited by PECVD on the substrate (Figure 34a). A standard photolithographic process was used to pattern the silicon nitride film (Figure 34b), which has been subsequently etched by RIE process in  $\text{CHF}_3/\text{O}_2$  atmosphere (Figure 34c). Finally, the silicon wafer was electrochemically anodized as previously described. Some detailed SEM images of a microchamber with porous silicon at the bottom are illustrated in Figure 35 [51].

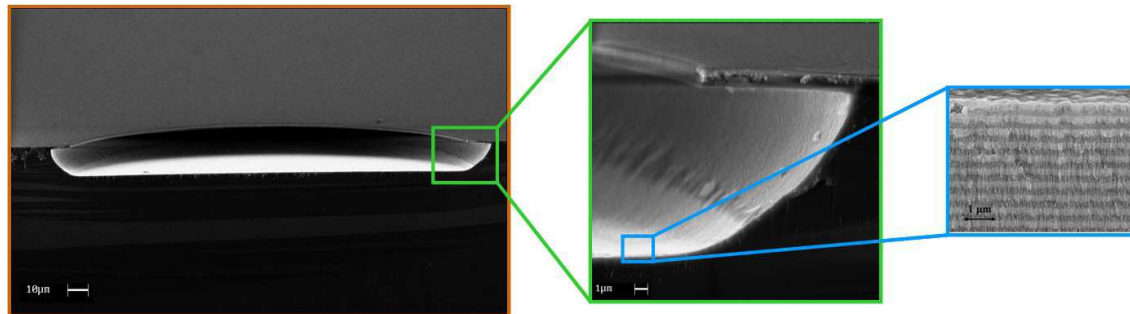


Figure 35 SEM images of one microchamber. In the first inset, a particular of the microchamber wall and the silicon nitride mask layer. In the second inset the structure of the porous layers.

The process is not as simple as the previous one, and more than one technological step are required. However as been shown in the results is better than with photoresist. The optical microscope image of the microarray and the reflectivity spectra of some Bragg mirror elements are reported in Figure 36.

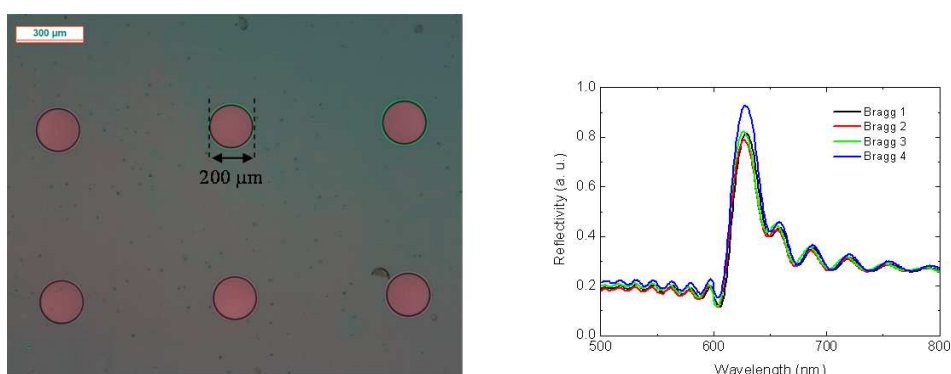


Figure 36 Optical microscope image of the microarray and reflectivity spectra of the PSi Bragg mirrors.

Each element is a Bragg reflectors of 200  $\mu\text{m}$ , realized by alternating high (H) refractive index layers (low porosity) and low (L) refractive index layers (high porosity); a current density of 80 mA/cm<sup>2</sup> was applied to obtain low refractive index layers ( $n_L=1.6$ ) with a porosity of 71 %, while one of 60 mA/cm<sup>2</sup> was applied for high index layers ( $n_H=1.69$ ) with a porosity of 68 %. The device was then fully oxidized in pure O<sub>2</sub>. The reflectivity spectra at normal incidence of the Bragg devices are characterized by a resonance peak at 627 nm and a FWHM of about 25 nm. The spectra demonstrate also the uniformity of the electrochemical etching on the whole microarray surface.

## References

- [1] S.K. Sia, G.M. Whitesides, Microfluidic devices fabricated in Poly(dimethylsiloxane) for biological studies, *Electrophoresis*. 24 (2003) 3563-3576.
- [2] S. Qi, X. Liu, S. Ford, J. Barrows, G. Thomas, K. Kelly, et al., Microfluidic devices fabricated in poly(methyl methacrylate) using hot-embossing with integrated sampling capillary and fiber optics for fluorescence detection, *Lab Chip*. 2 (2002) 88.
- [3] C. Hnatovsky, R.S. Taylor, E. Simova, P.P. Rajeev, D.M. Rayner, V.R. Bhardwaj, et al., Fabrication of microchannels in glass using focused femtosecond laser radiation and selective chemical etching, *Appl. Phys. A*. 84 (2006) 47-61.
- [4] M. Stoneman, M. Fox, C. Zeng, V. Raicu, Real-time monitoring of two-photon photopolymerization for use in fabrication of microfluidic devices, *Lab Chip*. 9 (2009) 819.

- [5] A.A.S. Bhagat, P. Jothimuthu, I. Papautsky, Photodefinable polydimethylsiloxane (PDMS) for rapid lab-on-a-chip prototyping, *Lab Chip*. 7 (2007) 1192.
- [6] A. Perl, D.N. Reinhoudt, J. Huskens, Microcontact Printing: Limitations and Achievements, *Advanced Materials*. 21 (2009) 2257-2268.
- [7] S.R. Quake, A. Scherer, From Micro- to Nanofabrication with Soft Materials, *Science*. 290 (2000) 1536 -1540.
- [8] X. Zhao, Y. Xia, G.M. Whitesides, Fabrication of three-dimensional microstructures: Microtransfer molding, *Advanced Materials*. 8 (1996) 837-840.
- [9] E. Kim, Y. Xia, G.M. [Harvar. U. Whitesides, *Micromolding in capillaries: Applications in materials science*, 1996.
- [10] E. King, Y. Xia, X. Zhao, G.M. Whitesides, Solvent-assisted microcontact molding: A convenient method for fabricating three-dimensional structures on surfaces of polymers, *Advanced Materials*. 9 (1997) 651-654.
- [11] Y. Xia, G.M. Whitesides, *Soft Lithography*, *Annu. Rev. Mater. Sci.* 28 (1998) 153-184.
- [12] D.J. Campbell, K.J. Beckman, C.E. Calderon, P.W. Doolan, R.M. Ottosen, A.B. Ellis, et al., Replication and Compression of Surface Structures with Polydimethylsiloxane Elastomer, *Journal of Chemical Education*. 76 (1999) 537.
- [13] D. Armani, C. Liu, N. Aluru, Re-configurable fluid circuits by PDMS elastomer micromachining, in: *Twelfth IEEE International Conference on Micro Electro Mechanical Systems, 1999. MEMS '99, IEEE, 1999: pp. 222-227.*
- [14] Chang W-J, Akin D, Sedlak M, Ladisch M. R, Bashir R, Poly(dimethylsiloxane) (PDMS) and Silicon Hybrid Biochip for Bacterial Culture.
- [15] J.C. McDonald, G.M. Whitesides, Poly(dimethylsiloxane) as a Material for Fabricating Microfluidic Devices, *Accounts of Chemical Research*. 35 (2002) 491-499.
- [16] L. Krogh, P. Asberg, *My Little Guide to Soft Lithography (or Soft Lithography for Dummies)*, Linköping University. (2003).
- [17] SU-8 2000 Permanent Epoxy Resists:: MicroChem.
- [18] P. Zandels, The photoresist SU-8 for thick-film applications.
- [19] E. Lam, T. Ngo, Manufacturing a PDMS microfluidic device via a Silicon Wafer Master, (2007).
- [20] B.-H. Jo, L.M. Van Lerberghe, K.M. Motsegood, D.J. Beebe, Three-dimensional micro-channel fabrication in polydimethylsiloxane(PDMS) elastomer, *Journal of Microelectromechanical Systems*. 9 (2000) 76-81.
- [21] D.T. Eddington, J.P. Puccinelli, D.J. Beebe, Thermal aging and reduced hydrophobic recovery of polydimethylsiloxane, *Sensors and Actuators B: Chemical*. 114 (2006) 170-172.
- [22] J.Y. Kim, J.Y. Baek, K.A. Lee, S.H. Lee, Automatic aligning and bonding system of PDMS layer for the fabrication of 3D microfluidic channels, *Sensors and Actuators A: Physical*. 119 (2005) 593-598.
- [23] J. Kuncova-Kallio, P.J. Kallio, PDMS and its Suitability for Analytical Microfluidic Devices, in: *28th Annual International Conference of the IEEE Engineering in Medicine and Biology Society, 2006. EMBS '06, IEEE, 2006: pp. 2486-2489.*

- [24] E.S. Park, D. Jang, J. Lee, Y.J. Kim, J. Na, H. Ji, et al., Maskless optical microscope lithography system, *Rev. Sci. Instrum.* 80 (2009) 126101.
- [25] S.E. Chung, W. Park, H. Park, K. Yu, N. Park, S. Kwon, Optofluidic maskless lithography system for real-time synthesis of photopolymerized microstructures in microfluidic channels, *Appl. Phys. Lett.* 91 (2007) 041106.
- [26] A. Ambrosio, E. Orabona, P. Maddalena, A. Camposeo, M. Polo, A.A.R. Neves, et al., Two-photon patterning of a polymer containing Y-shaped azochromophores, *Applied Physics Letters*. 94 (2009) 011115.
- [27] T. Deng, H. Wu, S.T. Brittain, G.M. Whitesides, Prototyping of Masks, Masters, and Stamps/Molds for Soft Lithography Using an Office Printer and Photographic Reduction, *Analytical Chemistry*. 72 (2000) 3176-3180.
- [28] A.M. Christenson, B.H. Augustine, Rapid Prototyping of Masks from Various 35mm Film Types for Use in Photolithography, in: National Conference On Undergraduate Research (NCUR) 2000. University of Montana, April 26-29, 2000. Missoula, Montana, n.d.
- [29] K.F. Hoettges, R.M. Gwilliam, K.P. Homewood, D. Stevenson, Fast prototyping of microfluidic devices for separation science, *Chromatographia*. 53 (2001) 424–426.
- [30] A. Uhlir, Electrolytic shaping of germanium and silicon, *Bell Syst. Tech. J.* 35 (1956) 333.
- [31] L.T. Canham, Silicon quantum wire array fabrication by electrochemical and chemical dissolution of wafers, *Applied Physics Letters*. 57 (1990) 1046-1048.
- [32] I. Rea, Porous Silicon based Optical Devices for Biochemical Sensing, PhD Thesis on Novel Technologies for Materials, Sensors, and Imaging, University of Naples “Federico II,” 2008.
- [33] R.L. Smith, S.D. Collins, Porous silicon formation mechanisms, *Journal of Applied Physics*. 71 (1992) R1-R22.
- [34] D.E. Aspnes, J.B. Theeten, F. Hottier, Investigation of effective-medium models of microscopic surface roughness by spectroscopic ellipsometry, *Physical Review B*. 20 (1979) 3292-3302.
- [35] X. Yu, D. Xu, Q. Cheng, Label-free detection methods for protein microarrays, *Proteomics*. 6 (2006) 5493-5503.
- [36] K.P. Dancil, D.P. Greiner, M.J. Sailor, A porous silicon optical biosensor: detection of reversible binding of IgG to a protein A-modified surface, *Journal of the American Chemical Society*. 121 (1999) 7925–7930.
- [37] P.A. Snow, E.K. Squire, P.S.J. Russell, L.T. Canham, Vapor sensing using the optical properties of porous silicon Bragg mirrors, *J. Appl. Phys.* 86 (1999) 1781.
- [38] L.D. Stefano, I. Rendina, L. Moretti, A.M. Rossi, Optical sensing of flammable substances using porous silicon microcavities, *Materials Science and Engineering B*. 100 (2003) 271-274.
- [39] L. Moretti, I. Rea, L. Rotiroti, I. Rendina, G. Abbate, A. Marino, et al., Photonic band gaps analysis of Thue-Morse multilayers made of porous silicon, *Opt. Express*. 14 (2006) 6264-6272.
- [40] V. Lehmann, U. Gosele, Porous silicon formation: A quantum wire effect, *Applied Physics Letters*. 58 (1991) 856-858.

- [41] I. Rea, E. Orabona, I. Rendina, L. De Stefano, Porous Silicon Integrated Photonic Devices for Biochemical Optical Sensing, in: Crystalline Silicon - Properties and Uses, Sukumar Basu, InTech, 2011.
- [42] L. Canham, Properties of Porous Silicon, Inspec/Iee, 1998.
- [43] D. Mark, S. Haeberle, G. Roth, F. von Stetten, R. Zengerle, Microfluidic lab-on-a-chip platforms: requirements, characteristics and applications, Chem. Soc. Rev. 39 (2010) 1153.
- [44] C. Fournier-Wirth, J. Coste, Nanotechnologies for pathogen detection: Future alternatives?, Biologicals. 38 (2010) 9-13.
- [45] S.W. Roh, G.C.J. Abell, K.-H. Kim, Y.-D. Nam, J.-W. Bae, Comparing microarrays and next-generation sequencing technologies for microbial ecology research, Trends in Biotechnology. 28 (2010) 291-299.
- [46] G. Rong, J.D. Ryckman, R.L. Mernaugh, S.M. Weiss, Label-free porous silicon membrane waveguide for DNA sensing, Appl. Phys. Lett. 93 (2008) 161109.
- [47] G. Rong, A. Najmaie, J.E. Sipe, S.M. Weiss, Nanoscale porous silicon waveguide for label-free DNA sensing, Biosensors and Bioelectronics. 23 (2008) 1572-1576.
- [48] M. Bally, M. Halter, J. Vörös, H.M. Grandin, Optical microarray biosensing techniques, Surface and Interface Analysis. 38 (2006) 1442-1458.
- [49] R. Dootz, A.C. Toma, T. Pfohl, Structural and dynamic properties of linker histone H1 binding to DNA, Biomicrofluidics. 5 (2011) 024104.
- [50] V.V. Starkov, E.Y. Gavrilin, J. Konle, H. Presting, A.F. Vyatkin, U. König, SU8 photoresist as an etch mask for local deep anodic etching of silicon, Physica Status Solidi (a). 197 (2003) 150-157.
- [51] I. Rea, A. Lamberti, I. Rendina, G. Coppola, M. Gioffre, M. Iodice, et al., Fabrication and characterization of a porous silicon based microarray for label-free optical monitoring of biomolecular interactions, Journal of Applied Physics. 107 (2010) 014513-014513-4.

## **Chapter 3**

# **A microfluidics assisted porous silicon array for optical label-free biochemical sensing**

The result of the fruitful mixing between biosensing and microfluidics is exposed in this Chapter: the integration of a microfluidic system onto a porous silicon microarray, which fabrication processes have been reported in Chapter 2, is step-by-step illustrated, and its features are investigated. Experimental proofs and numerical calculation have been performed. These results have been published in:

- Rea, E. Orabona, A. Lamberti, I. Rendina, L. De Stefano, A microfluidics assisted porous silicon array for optical label-free biochemical sensing, *Biomicrofluidics*. 5 (2011) 034120.
- E. Orabona, I. Rea, I. Rendina, L. De Stefano, Numerical Optimization of a Microfluidic Assisted Microarray for the Detection of Biochemical Interactions, *Sensors*. 11 (2011) 9658-9666.

### **3.1 Design a microfluidic circuit for biochemical interactions**

In the past two decades microfluidics has emerged as a powerful tool for biosensing [1] and biophotonics [2]. Microfluidic devices require small reagent volumes, short reaction times and allow high throughput due to their parallel mode of operation. Microfluidics represent a fundamental tool to integrate almost all the functionality of a laboratory onto a single chip, i.e., a lab-on-a-chip. Microfluidics also hold promise for many other applications, such as the manipulation of nanomaterials [3,4]. In recent years, the study of microfluidic systems for biosensing has become an active research field. Biosensors exploit a variety of different detection mechanisms such as microcantilever based

transducers [5], surface plasmon resonance sensors [6], and porous silicon based biosensors [7,8]. In these devices, the selectivity, *i.e.*, the ability to quantify a particular target analyte in a complex mixture, is due to some specific interaction between a bioprobe, such as a DNA single strand or a protein or an enzyme, and its own ligand. Even if the basic principles of molecular interaction detection are completely different, a common key issue is thus the analyte-ligand binding kinetic. The specific and selective recognition of analytes occurs at the reacting surface of the biosensor, which is a solid-liquid interface. The reaction kinetics can be described as a two-step process; namely, a mass-transport process, which takes into account the diffusion or the dragging of molecules in the fluids, and a chemical surface reaction process, which depends strictly on molecular interactions.

Many works concerning the modelling of a microfluidic biosensor have appeared recently. The main aim of these studies usually was to improve some aspect of the sensing performance, such as sensitivity, time response, and dependence on external factors. How the assay parameters determine the amount of captured analytes [9], the optimization of a microfluidic channel in case of a nanowire biosensor [10], the electro-thermal effect on diffusion enhancing [11], and a novel design for fiber-optic localized plasmon resonance biosensor [12] are some topics that have been studied.

Among biosensors, the microarray technology has demonstrated a great potential in drug discovery, proteomics research, and medical diagnostics. The reason of this success is the very high throughput of these devices due to the large number of samples that can be analyzed simultaneously in a single parallel experiment. The microarray technology is based on the immobilization of a huge amount of bioprobes on a solid platform, which can be obtained by *in situ* direct synthesis of the biomolecules or by binding them on a functionalized area.

The convergence between microfluidics and microarrays has been relatively straightforward due to their multiple shared features, but the implementation of a microfluidic circuit on an array device is not trivial nor simple: a specific design is often required to meet biological constraints and fabrication technique demands. In this context, numerical simulations by finite element methods (FEM) allow a space and time

characterization of the biomolecule distribution and interaction in the circuit. Hu *et al.* explained in [13] the different antigen-antibody binding kinetic between four sensing elements, proposing a “zigzag” array configuration to improve binding uniformity; Lee *et al.* proposed a recirculating flow system for a microfluidic DNA microarray to improve the rate of hybridization [14]; Srivannavit *et al.* instead proposed a microfluidic reactor array for massively parallel *in situ* synthesis of oligonucleotides obtaining a quite uniform binding kinetics on to the array [15].

In this regard, a numerical study by FEM analysis of the binding interaction between active sites on the array surface elements with biochemical species in microfluidic networks is highly required in order to understand the role of geometrical and dynamical parameters. While the literature works generally consider interactions between biochemical species under flow conditions, in the simulations elaborated in this work the binding kinetics is under static conditions, with an initial step involving flow of a liquid solution to fill the channel, followed by a flow velocity decreasing to a zero value. The results with respect to the dynamic approach have been compared. Many experiments, especially those requiring consumption of a very low volume of reagent for economic or technical reasons, are driven in static, or quasi-static, steady flow conditions, so that the aim of the work is a useful design tool for both situations. On the basis of the results obtained, a new microfluidic layout for parallel flow, able to provide efficient and uniform analyte distribution on the sensing part of microfluidic assisted microarrays, has been proposed.

### **3.1.1 Binding kinetic inside microchannels**

The modelling of what happens before transduction of a biomolecular interaction in a biosensor requires considering at least three physical processes: (1) the surface reactions, i.e., the binding of a biomolecule onto the functionalized surface; (2) the fluid flow in microchannels, which takes into account the mass transport in the microfluidic circuit; (3) the diffusion of chemical species, which is the only process for bringing an analyte to the active site(s). The interaction (1) between one chemical species A ( $\text{mol}/\text{m}^3$ ), present in a buffer solution, and a second chemical species B ( $\text{mol}/\text{m}^2$ ), bound

to the sensing area, producing a complex C created by the two molecular species, can be described by the first order time-dependent Langmuir Equation (2):



$$\frac{\partial C}{\partial t} = k_a A \cdot (B - C) - k_d C \quad (2)$$

where C is measured in mol/m<sup>2</sup>, k<sub>a</sub> is the association rate constant (M<sup>-1</sup>s<sup>-1</sup>), and k<sub>d</sub> is the dissociation rate constant (s<sup>-1</sup>). This equation can be used for antigen-antibody [10,13] or protein-ligand reactions [11] or other biochemical interactions. The equilibrium complex concentration C<sub>eq</sub> can be expressed as:

$$C_{eq} = \frac{AB}{A + k_d / k_a} \quad (3)$$

where the ratio k<sub>d</sub>/k<sub>a</sub> represents the inverse of the affinity constant. The response of a biosensor is proportional to the amount of the compound C formed on the sensing regions. It is crucial to understand the behaviour of the complex formation rate C(t) and equilibrium concentration C<sub>eq</sub> in the microfluidic configuration assigned in order to maximize the sensor response as a function of the fabrication parameters.

The fluid flow can be modelled using the Navier-Stokes equations (see Chapter 1). The values of fluid constants are assumed as those of water: ρ = 10<sup>3</sup> kg/m<sup>3</sup> and μ = 10<sup>-3</sup> Pa·s. The flow is considered laminar with a parabolic profile at the inlet and an average velocity u<sub>0</sub>, since the flow in the microchannel is in the low Reynolds number region. Boundary conditions for the equations are zero pressure (p = 0) at the outlet and no-slip walls (u = 0) elsewhere.

The transport of a chemical species A in bulk liquid phase is described by the convection and diffusion equation (see Chapter 1) using the following boundary conditions:

$$\begin{aligned} A &= A_0 \quad \text{at the inlet;} \\ \vec{n} \cdot (D\nabla A) &= 0 \quad \text{at the outlet;} \\ \vec{n} \cdot (A\vec{u} - D\nabla A) &= 0 \quad \text{at the microchannel walls;} \end{aligned} \quad (4)$$

$$\vec{n} \cdot (A\vec{u} - D\nabla A) = -\frac{\partial C}{\partial t} \text{ at the reaction surfaces.}$$

where  $\vec{n}$  is the unit normal vector to the surface.

In order to simulate a static process, inlet conditions  $A_0$  and  $u_0$  has been multiplied for the function  $1 - H(t - t_{fill}, t_{scale})$ . The  $H(t - t_{fill}, t_{scale})$  is a smoothed version of the Heaviside step function where  $t_{fill}$  is the necessary time to fill the channel given by  $L/u_0$  (L is the total device length) and  $t_{scale}$  is 1 second. As illustrated in Figure 37 the function is 0 for  $t < t_{scale}$ , and 1 for  $t > t_{scale}$ ; in the interval  $-t_{scale} < t < t_{scale}$ , the function is a smoothed function with a continuous first derivative, defined by a fifth-degree polynomial.

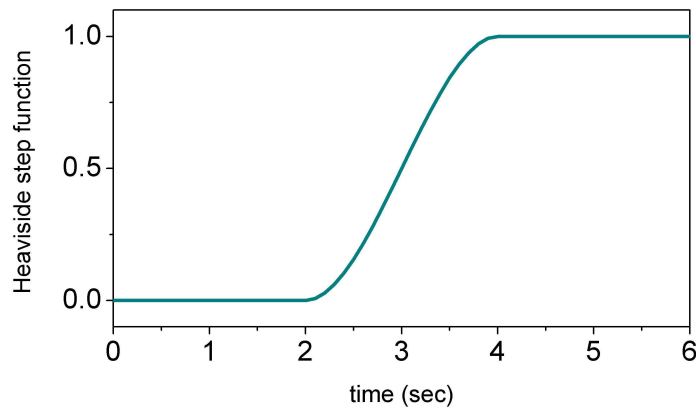


Figure 37 A smoothed Heaviside step function with  $t_{fill} = 3\text{sec}$ ,  $t_{scale} = 1\text{sec}$ .

In this way, it has been possible to simulate the injection of the solution of A for  $t_{fill}$  seconds in the microchannel and then the subsequent static incubation. Under dynamic conditions a constant flow velocity in the microchannels is assumed. Numerical calculations have been performed using the FEMLAB™ (Comsol Inc.) finite element software package combining the three differential equations into a single model.

The microarray considered is composed by sixteen elements arranged in  $4 \times 4$  matrix: each circular element has a radius of  $100 \mu\text{m}$  and they are spaced  $600 \mu\text{m}$  apart. In this

work, two different microfluidic configurations are considered; an example of the first one is sketched in Figure 38a. The microfluidic channels are 250  $\mu\text{m}$  wide, 10  $\mu\text{m}$  high, and 3 mm long and connect the elements as show in Figure 38b. The distance between the inlet and the first element is the same as between the last element and outlet which has been considered equal to 300  $\mu\text{m}$ . The 3D geometry has been simplified to 2D assuming negligible variations in the concentration across the width of the microchannel. For simulations, typical values for  $k_a$  and  $k_d$  ( $k_a = 5 \times 10^5 \text{ M}^{-1} \text{ s}^{-1}$ ,  $k_d = 10^{-4} \text{ s}^{-1}$ ) [16], a typical diffusion coefficient for  $D = 10^{-11} \text{ m}^2/\text{s}$  and an active site surface concentration  $B = 1 \times 10^{-8} \text{ mol/m}^2$  have been assumed.

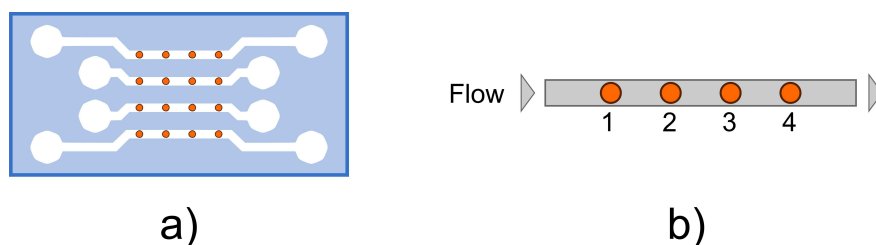


Figure 38 (a) An exemplary scheme of the microfluidic assisted microarray, (b) scheme of the channel with four sensing elements used in the model.

It has been also assumed  $A_0 = 10 \text{ nM}$  and  $u_0$  ranging from 0.1 to 10 mm/s: the formation of compound C in the sensing region by changing the inlet velocity has been studied: this parameter because it doesn't directly influence the equilibrium complex concentration  $C_{eq}$  and can be easily controlled in real experiments by an automatic pump. Other parameters, such as the diffusion coefficient or the affinity constant, can be adapted according to the chemical species considered. The results of the amount of C on the surface of four elements under static steady flow conditions in a single channel are shown in Figure 39. The simulation has shown that there is a clear decrease in the formation of compound C which is proportional to the inlet distance from the first to the fourth element, respectively.

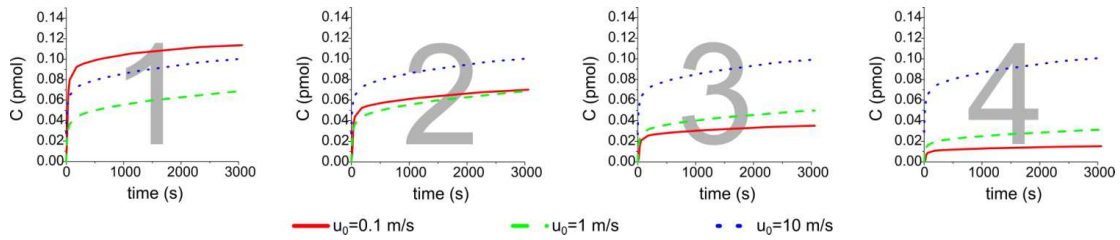


Figure 39 Comparison of the formation of complex C simulating a static incubation from the first to the last element in a linear microchannel for different inlet velocity values.

The effect is due to a concentration decrease along the channel of the chemical species A as shown in Figure 40: by increasing the inlet velocity up to 10 mm/s more homogeneous values among the four active surfaces can be obtained [17]. A change of the inlet position will cause only a time shift in the graphs of Figure 39.

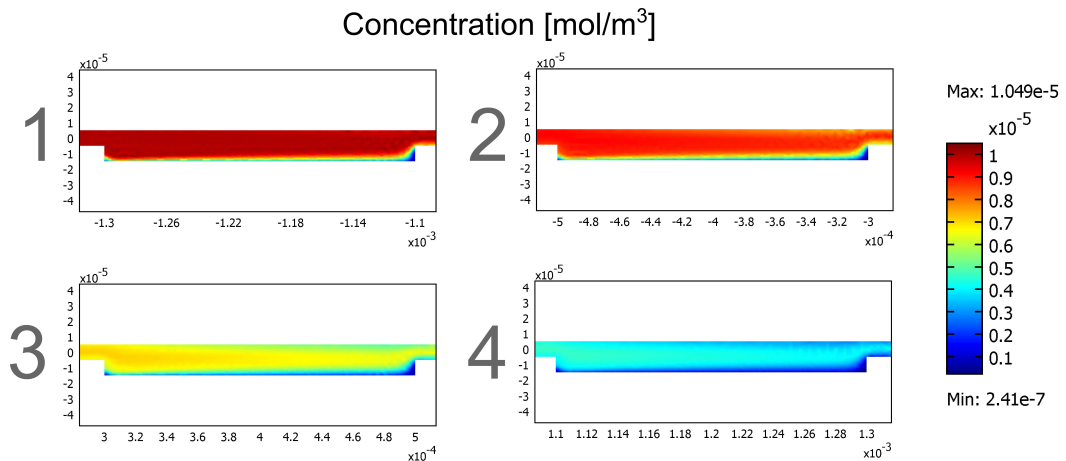


Figure 40 Concentration distribution of molecular species A in the microchambers at 3 seconds just after the injection. A significant difference in concentration is well evident. The numerical simulation has been obtained with an inlet velocity of  $1 \cdot 10^{-3}$  m/s.

### 3.1.2 Optimization of microfluidic circuit by numerical simulations

The second layout considered is viewed as an improvement of the device using the same elements configuration, but changing the microfluidic network. In this design, a parallel approach (see Figure 41a) with four parallel channels, which transport the

chemical species, have been proposed, thus avoiding the formation of a different surface density of the compound C on the sensing elements.

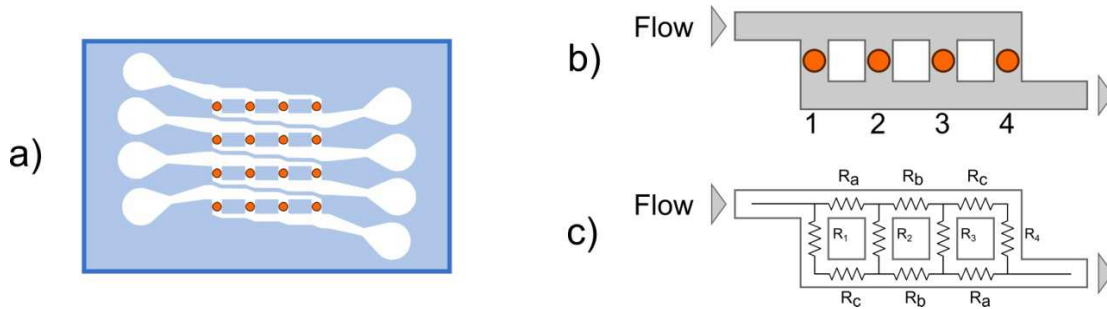


Figure 41 An example scheme of the microarray with the new microfluidic layout proposed, (b) the scheme of the channel with four sensing elements used in the model, and (c) its electrical model.

Since under static flow conditions, a homogeneous distribution of C along the channel depends on the average inlet velocity: to have the same density of C in the parallel active sites, the same local velocity is necessary.

As described in Chapter 1 the microfluidic network can be modelled as an electrical network (Figure 41b). For the sake of simplicity,  $R_i$ ,  $L_i$ ,  $h_i$ ,  $w_i$ , represent the resistance, the length, the height and the width of the  $i$ -channel, respectively, where  $i$  can be 1, 2, 3, 4, for the channels, in correspondence with the four elements, or  $a$ ,  $b$ ,  $c$  for the channels that connect them, as shown in Figure 3(b) (a symmetric microfluidic network has been designed to allow inversion of inlet and outlet as desired). Using Kirchoff's circuit laws, the condition of equal flows  $Q$  ( $Q_1 = Q_2 = Q_3 = Q_4$ ) is satisfied when  $R_c = 3R_a$ . The resistances of the channels  $a$ ,  $b$  and  $c$  have been tuned only by changing the width  $w$ : in this way has been avoided a superfluous increase of the microfluidic network complexity. The 1, 2, 3, and 4 channel dimensions were taken equal and the same of the first layout proposed ( $w = 250 \mu\text{m}$  and  $h = 10 \mu\text{m}$ ). The previous relation thus becomes:

$$w_a = 3w_c - 2 \cdot 0.63h \quad (10)$$

for the widths of channels  $a$  and  $c$ . No condition must be imposed on  $w_b$ , a mean value between  $w_a$  and  $w_c$  has been chosen. The design, based on Equations (9) and (10), of a microfluidic circuit which can homogeneously distribute the biomolecules in each

active area, has been tested by numerically solving the incompressible fluid flow using 3D Navier Stokes equations. The model has been verified assuming  $w_c = 100 \mu\text{m}$  (then  $w_a = 287.4 \mu\text{m}$ ,  $w_b = 193.7 \mu\text{m}$ ), and  $h = 10 \mu\text{m}$ ; a surface map, giving the velocity field illustrated in Figure 42a.

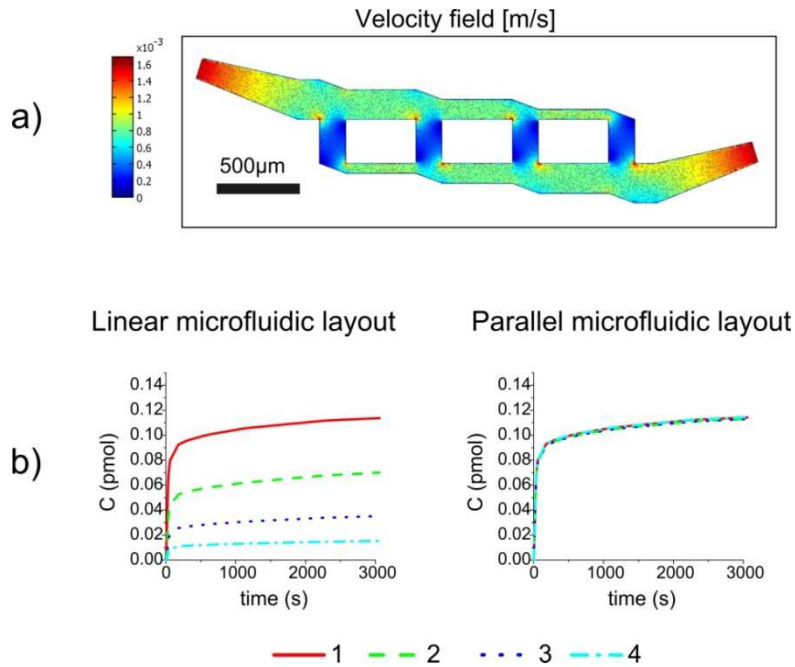


Figure 42 a) Fluid dynamic simulation by FEMLAB™ of the new proposed microfluidic layout. b) Comparison of binding kinetics obtained simulating a static incubation from the first to the last element in linear and the parallel microfluidic systems, respectively.

From these calculations, it results that the four current flows are equal within a confidence range of less than 5%. The electrical network analogy can be thus used for the fabrication of a compact microfluidic circuit which feeds the chemical substance B in parallel. The comparison between the binding kinetics of formation of C in the four active areas in the case of the two microfluidic layouts for  $u_0 = 1 \text{ mm/s}$  is presented in Figure 42b. From Figure 42b, where the binding kinetic using a static flow condition is presented, it is clearly evident that the parallel microfluidic layout, which assures a homogeneous velocity field across each active area, also give rise to an equal C complex formation in all the sensing elements. The advantages of a parallel configuration are also evident in case of dynamic flow conditions. The microfluidic

circuit behaviour quantifying the formation of complex C in the four active zones for a 1 mm/s solution flow has been simulated. The results are reported in Figure 43.

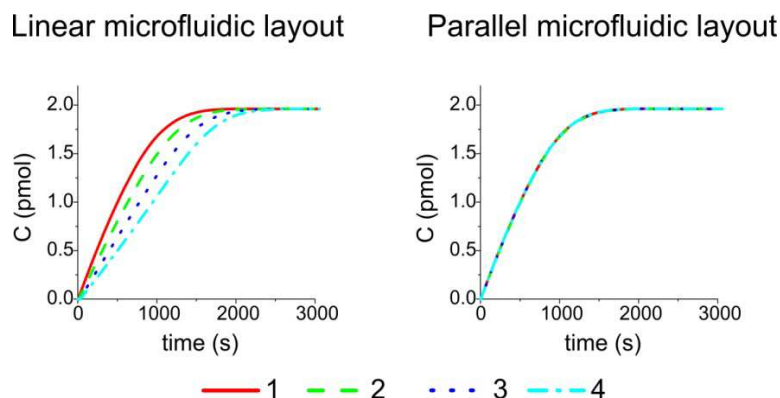


Figure 43 Comparison of C formation binding kinetics obtained by simulating a dynamic incubation from the first to the last element in linear and parallel microfluidic system, respectively.

In a dynamic regime, the four active areas reach the same amount of C are different time points, and the saturation condition is obtained with a time difference of 48% between the last element (2040 s) with the respect to the first element (1380 s). By parallel microfluidics it is possible to almost cancel this delay: all the elements saturate in the same interval (the time delay is less than 1%). the binding kinetics under dynamic flow conditions dependence on the inlet velocity in the case of a parallel microfluidic system has been investigated; the results are shown in Figure 44.

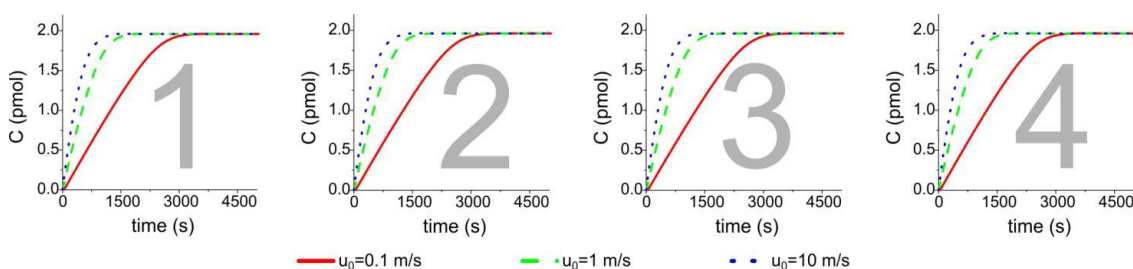


Figure 44 Comparison of the formation of complex compound C simulating a dynamic incubation from the first to the last element in a parallel microfluidic system for different inlet velocity values.

The simulations have confirmed that there are no substantial differences among the four elements in this case, and also a substantial decrease of saturation time can be noted upon increasing the inlet velocity: the saturation value is reached in 2,880 s for  $u_0 = 0.1$  mm/s, in 1,380 s for  $u_0 = 1$  mm/s, and in 1,020 s for  $u_0 = 10$  mm/s. The effect is also evident in the concentration map of A illustrated in Figure 45.

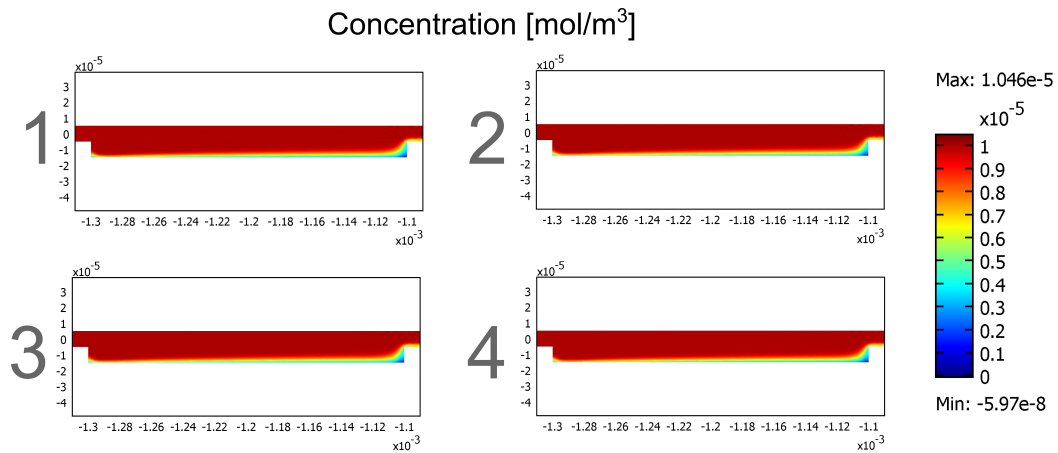


Figure 45 Concentration distribution of molecular species A in the microchambers at 3 seconds just after the injection using the parallel microfluidic layout. A significant difference in concentration is not present. The numerical simulation has been obtained with an inlet velocity of  $1 \cdot 10^{-3}$  m/s.

In conclusions it's possible to state that the inlet velocity plays a fundamental role in the optimization of the microfluidic microarray both for static and dynamic regimes. Then dynamic flow condition approach seems to be the best in terms of homogeneity and time parameters for the microfluidic biosensor, but the static approach can be useful in case where very low sample consumption is necessary [17].

### 3.2 Microfluidic integration on to a porous silicon based microarray

The following paragraph is dedicated to the integration of a porous silicon (PSi) microarray, made of Bragg mirrors, with a microfluidic circuit made of

polydimethylsiloxane (PDMS): the combination of optics and microfluidics can boost technology towards new devices for biosensing [18–20]. The integration of a PSi transducer in an optical microsystem is never straightforward nor trivial from the technology point of view [21,22]: the applied microfluidic system, which strongly reduces the functionalization time, chemicals and biological products consumption, should also preserve all the features of the PSi label-free optical detection. On the other side, the integration of such optical transducers in a microsystem is an unavoidable step towards the realization of an industrial prototype, which could be considered for production purposes.

A microarray of porous silicon (PSi) Bragg mirrors on a crystalline silicon substrate has been realized using a technological process described in Chapter 2. In this process the PSi surface, stabilized by means of a thermal oxidation at 900°C, was immersed in Piranha solution (4:1 sulphuric acid to hydrogen peroxide) for 40 min in order to assure the formation of Si-OH bonds. The chip was rinsed with deionized water and dried in a nitrogen stream. Then, the PSi surface was silanized in a 5 % solution of APTES (3-aminopropyltriethoxysilane) and anhydrous toluene for 30 min at room temperature. After the reaction time, the chip was washed twice in toluene to remove unlinked APTES, and baked at 100°C for 10 min. The microfluidic system has been realized with replica molding technique in polydimethylsiloxane illustrated, as the microarray fabrication process, in Chapter 2. The surfaces of PDMS layer and microarray were activated by exposing to oxygen plasma for 10 s to create silanol groups (Si-OH), as shown in the schematic reported in Figure 46a, aligned under a microscope using an x-y-z theta stage with an accuracy of 5 µm, and sealed together by keeping the two surfaces in contact without any external pressure (Figure 46b). Figure 46c shows a schematic of the PSi array integrated with the microfluidic circuit. The microfluidic device consists of four channels 250 µm wide, 10 µm high, and 3 mm long, each one connecting four Psi elements with a diameter of 200 µm and spaced by 600 µm. The images (a) and (b) in Figure 47 show top and lateral views of the microfluidic device compared to a one cent euro coin size (16.25 mm diameter).

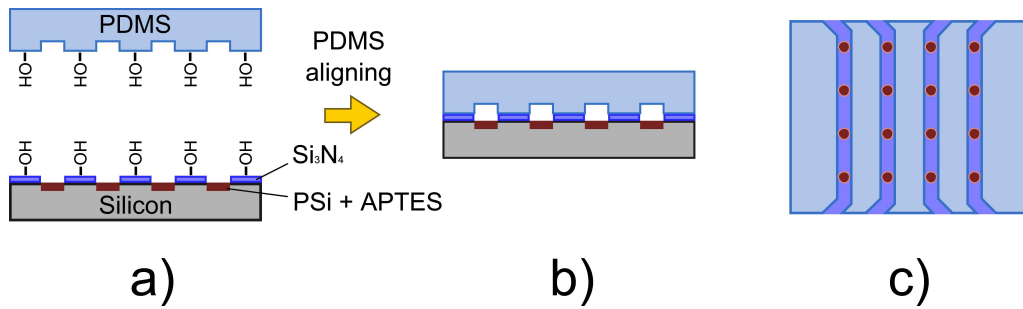


Figure 46 Schematic illustration of the fabrication process used to integrate the PSi array with a PDMS microfluidic system: (a) plasma activation of the surfaces; (b) section and top view (c) of the sealed device.

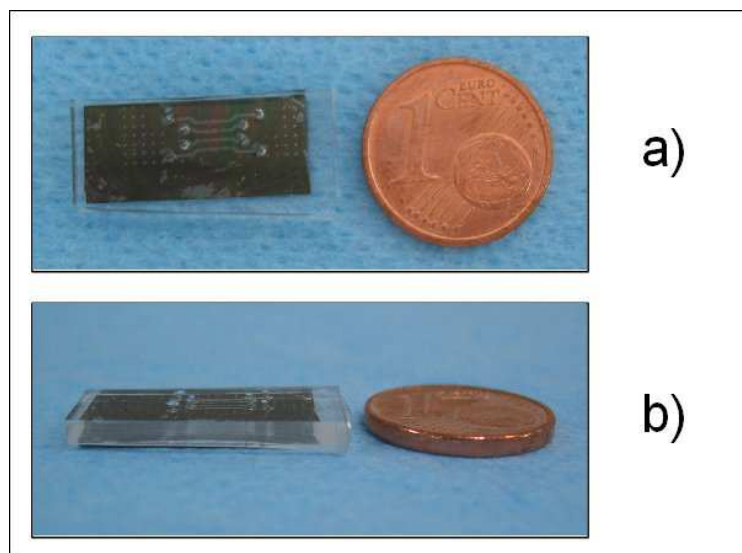


Figure 47 a) top and b) lateral views of the microfluidic assisted porous silicon array.

The reflectivity spectra of the Bragg reflectors were measured at normal incidence by means of a Y optical reflection probe, connected to a white light source and to an optical spectrum analyzer. The spectra were collected over the range 600-1000 nm with a resolution of 0.2 nm. The light spot size has been focused on the single PSi device using a 10× microscope objective. The presence of the PDMS layer, which completely seals the array, does not greatly affect the optical spectra of the PSi Bragg reflectors: the

reflectivity spectra of a PSi element before and after the sealing process, reported in Figure 3, show a small peak shift of about 3 nm, which is due to humidity condensation.

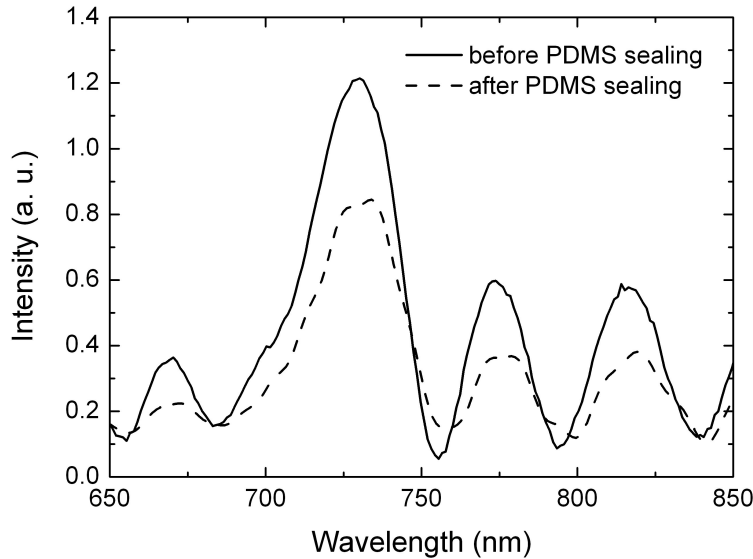


Figure 48 Reflectivity spectra of a PSi element before (solid line) and after (dashed line) the sealing with the PDMS microfluidic system.

The shift can be removed by a peristaltic pump applied to a close channel, but it rapidly restores when the channel inlet is open. An attenuation of about 30% in the reflected intensity can also be noted, due to the light scattering and absorption in the PDMS layer. The resonance peak wavelength is, on average among all the PSi Bragg, equal to  $730 \pm 2$  nm, the error being the standard deviation. Moreover, the microfluidic channels greatly facilitate the functionalization process of PSi elements (Figure 49): the biochemical solutions containing the glutaraldehyde, as a cross-linker, and the DNA single strands, as bioprobes, can be directly injected into the microfluidic circuit so that only few microlitres are necessary to fill the microchannel zone (about 15 nl) and the inlet and outlet channels (less than 5  $\mu$ l). PSi optical transducers are completely covered by the passivation solution just using a smaller volume with respect to more than 30  $\mu$ l required in the functionalization of not integrated PSi devices [23,24]: in this way, the reagents consumption and avoided every manual handling have been reduced.

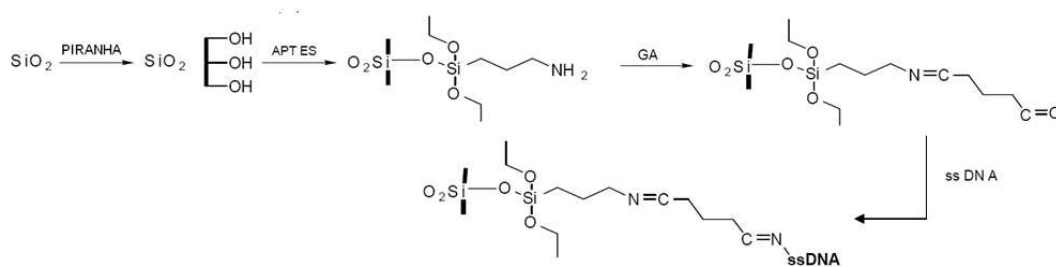


Figure 49 Scheme of the functionalization process of PSi surface with DNA probe single strand.

### 3.2.1 Biofunctionalization of the microfluidic PSi-array

The PSi microarray elements were bio-functionalized by injecting the solutions into the microfluidic channels using a peristaltic pump. Firstly, the microchannels have been filled with a 2.5% glutaraldehyde solution in 20mM HEPES buffer (pH 7.5) for 30 min; the excess glutaraldehyde was flushed away by  $15 \mu\text{l buffer min}^{-1}$  for 5 min. Then,  $5 \mu\text{l}$  of DNA probe (5'-GGACTTGCCCCGAATCTACGTGTCC-3'- $\text{NH}_2$ ; 200  $\mu\text{M}$  in 10mM HEPES buffer, pH8) were introduced into each channel and incubated for 3h at room temperature. The un-attached DNA was removed by flow-through washing with  $15 \mu\text{l buffer min}^{-1}$  for 5 min and with DI water for 2 min.  $5 \mu\text{l}$  of complementary (5'-GGACACGTAGATTCGGGCAAGTCC-3'; 200  $\mu\text{M}$  in 10mM HEPES buffer, pH 7.5) and non-complementary (5'-CACTGTACGTGCGAATTAGGTGAA-3'; 200  $\mu\text{M}$  in 10 mM HEPES buffer, pH 7.5) DNA were pumped into two different channels of the device and incubated for 1 h. The microchannels have been rinsed in buffer and DI water to remove the excess of biological matter.

The grafting of DNA single strand probes on the PSi surface has been verified by spectroscopic reflectometry: the biological molecules attached to pore walls induce an increasing of the effective refractive index of the layers and, as consequence, a red-shift of the reflectivity spectrum of each PSi optical transducers. In Figure 50, the spectra of four PSi Bragg reflectors, belonging to the same microchannel, before and after the DNA functionalization process have been reported: an average red-shift of  $18 \pm 2 \text{ nm}$

has been measured, which is a value higher than  $10.4 \pm 0.6$  nm obtained in the case of a not integrated PSi microarray [25].

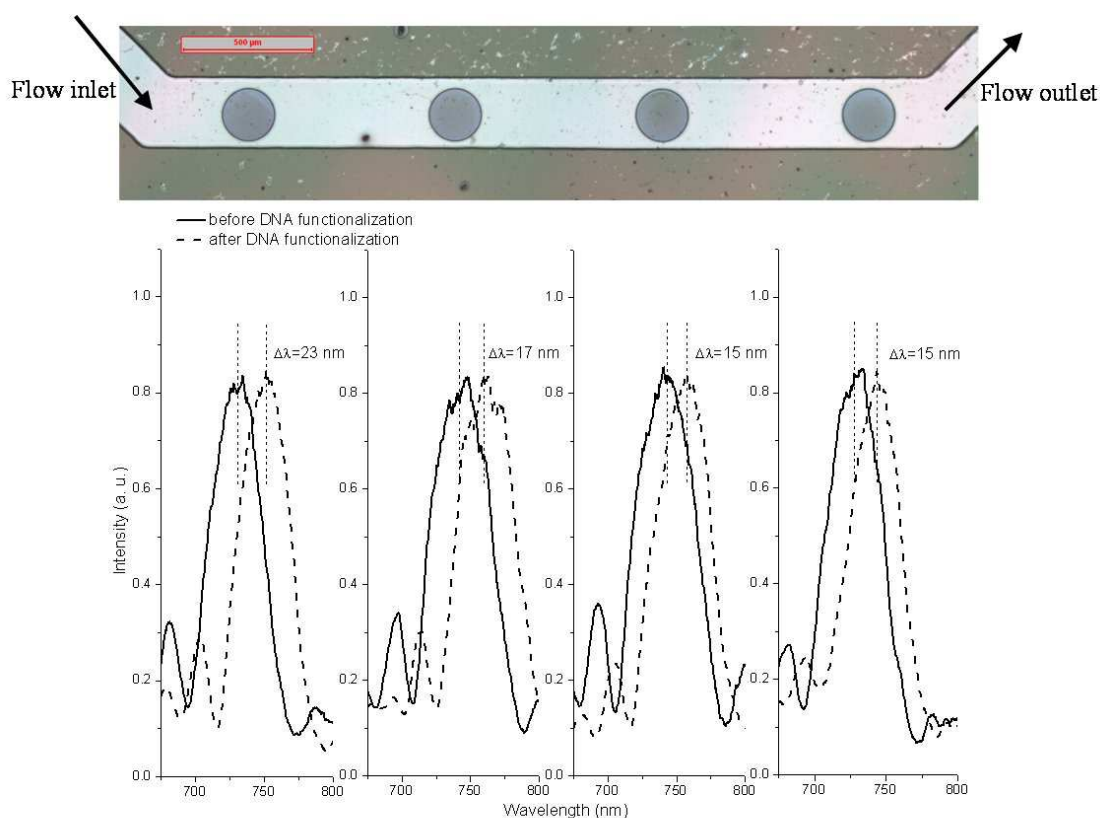


Figure 50 Top image: optical micrograph of a microfluidic channel. Bottom image: reflectivity spectra of the PSi elements before (solid line) and after (dashed line) the DNA probe functionalization.

The red-shift increase observed in the integrated device is simply due to a higher ratio [GA active sites available/ DNA probe concentration], with respect to the case of the array without microfluidics. A significant shortening of the process time has been observed: the bioprobes have been incubated for only 3h instead of the overnight treatment reserved to free PSi samples. The reduction of the incubation time can be justified by considering the diffusion of the DNA molecules in a solution according to the Fick's law [26]; the diffusion time of a DNA single strand (25 mer, 7.7 kDa), characterized by a diffusion coefficient of about  $10^{-11}$  m<sup>2</sup>/s at room temperature [27], is,

in fact, three orders of magnitude lower in a nanolitre volume with respect to a microlitre one. Anyway, the microfluidic circuit cannot be simply schematized as a small volume; for this reason, it was experimentally determined, which was the incubation time to be used by measuring the red-shifts of the optical spectra after 2, 3, 4, and 8 h. The 3h incubation was chosen, since it has been found that the red-shift after 4h was equal to that obtained after 3h and greater than that measured after 2h. The sample incubated for 8h shown a red-shift less than the 2h sample, which means that the PSi matrix was partially dissolved by the buffer.

The red-shift due to DNA functionalization is not equal for all the Bragg spectra: its magnitude decreases from 23 nm to 15 nm along the flow propagation direction. The phenomenon can be due to the decreasing of the DNA probes concentration in the propagation flow caused by the interaction with the GA into the channel [28].

### 3.2.2 Binding kinetic analysis

In order to better understand how the functionalization process proceeds in the microchannels, two different numerical calculations have been performed. The functionalization dynamic which the interaction between the bioprobes (the DNA) and the active sites (the glutaraldehyde), has been investigated as illustrated in the previous paragraph, can be summarized by the following expression:



where A is the DNA-probe concentration into the channel, B is the glutaraldehyde surface density on the porous silicon walls, and C is the surface density of the bound bioprobes. A proper boundary condition must be applied to the convection and diffusion equation:

$$\vec{n} \cdot (A\vec{u} - D_{PSi} \nabla A) = -\frac{\partial C}{\partial t} \quad (6)$$

D ( $10^{-11}$  m<sup>2</sup>/s) and D<sub>PSi</sub> ( $6.0 \times 10^{-12}$  m<sup>2</sup>/s) are the diffusion coefficients of the chemical specie A in bulk phase and in the PSi pores. The flow is considered laminar with a parabolic profile at the inlet and an average velocity  $u_0$  (inlet velocity =  $3 \cdot 10^{-3}$  m/s). In

first simulation only the first few seconds of the bio-functionalization process have been considered, since the liquid flow rapidly tends to zero and the probes can only diffuse in the available volume. In this approach, the bound probe surface density  $C$  can be neglected in the last two terms:

$$\frac{\partial C}{\partial t} = k_a A \cdot B - \cancel{k_a A \cdot C} - \cancel{k_d C} \quad (7)$$

Each PSi element has been modelled as a flat surface on which the  $D_{PSi}$  diffusion coefficient of the DNA probe has been supposed constant, since the functionalization process can be considered uniform along the pore walls [29], and corrected with respect to its value in bulk solution ( $D$ ) according to the hindered diffusion theory [30,31]. In order to take into account the large specific surface area of the PSi element ( $S_{SA} = 100 \text{ m}^2/\text{cm}^3$ ) [32], a very high surface density of active sites,  $B$ , i.e., the ratio between the glutaraldehyde molecules bound on the PSi element,  $N_B$ , and its area, has been used in calculations, using the equation

$$B = \frac{N_B}{a} = C_B \cdot d \cdot S_{SA} \quad (8)$$

where  $C_B$  is the density of active sites experimentally measured in a porous silicon layer ( $20 \cdot 10^{-5} \text{ mol/m}^2$ ) [33],  $a$  is the area of the PSi element ( $0.3 \cdot 10^{-3} \text{ cm}^2$ ), and  $d$  is its thickness ( $4.3 \cdot 10^{-4} \text{ cm}$ ). An association constant  $k_a = 10^5 \text{ M}^{-1} \cdot \text{s}^{-1} = k_a^{(\text{calc})}$  [34] has been assumed, and that there are no changes in the amount of DNA probes bound to the PSi surface on increasing or decreasing the association rate value of some magnitude orders have been verified, as it can be deduced from the graph reported in Figure 51. In particular, from this graph, it is possible to estimate the association rate value ( $k_a^{(\text{sat})}$ ), which corresponds to the saturation of the binding sites available.  $k_a^{(\text{sat})}$  is two orders of magnitude lower with respect to that used in calculations. Figure 52, the maps of DNA probes concentration available in the first (a) and last (b) microchambers are reported together with the respective mean concentration variations along the length and the depth of the channel.

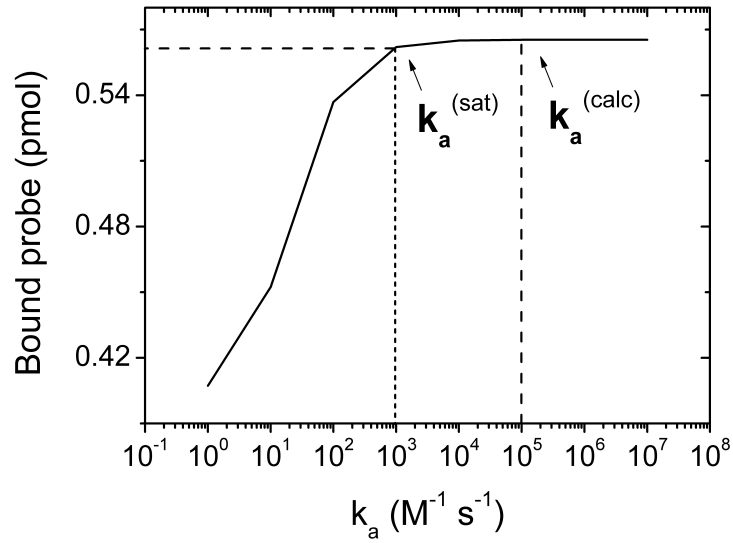


Figure 51 DNA probes bound to the porous silicon surface calculated for different values of the association rate,  $k_a$ .

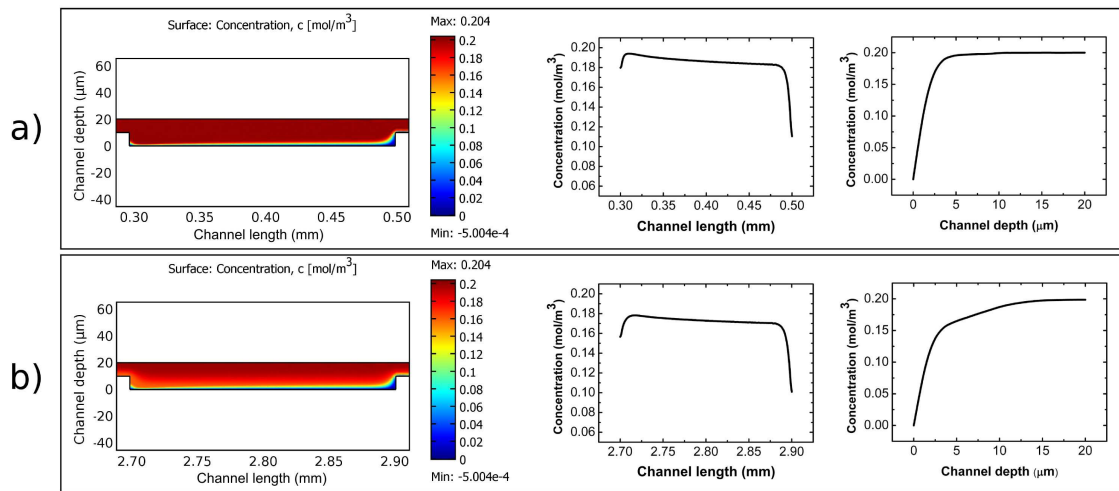


Figure 52 Comparison between the DNA concentration distribution in the first (a) and last (b) microchambers just after the injection of the probe. A significant difference in DNA probes concentration is well evident. The numerical simulation has been obtained with an inlet velocity of  $3 \cdot 10^{-3}$  m/s.

The distribution of DNA probes in the microchamber has been obtained by numerically solving the equations with constants values previously reported, in particular, the inlet velocity was  $u_0 = 3 \cdot 10^{-3}$  m/s. It's clearly possible to observe an inhomogeneous distribution of DNA probes, which can be attributed to the starting concentration gradient of the probes, that is, strictly related to the inlet velocity.

As explained in the previous paragraph to have probes concentration uniform along the fluidic channel this effect, the inlet velocity should be increased up to  $3 \cdot 10^{-2}$  m/s: the difference between DNA probe concentrations bound on the surfaces of the first and last PSi devices is about 5%. The results of the calculations are illustrated in Figure 53.

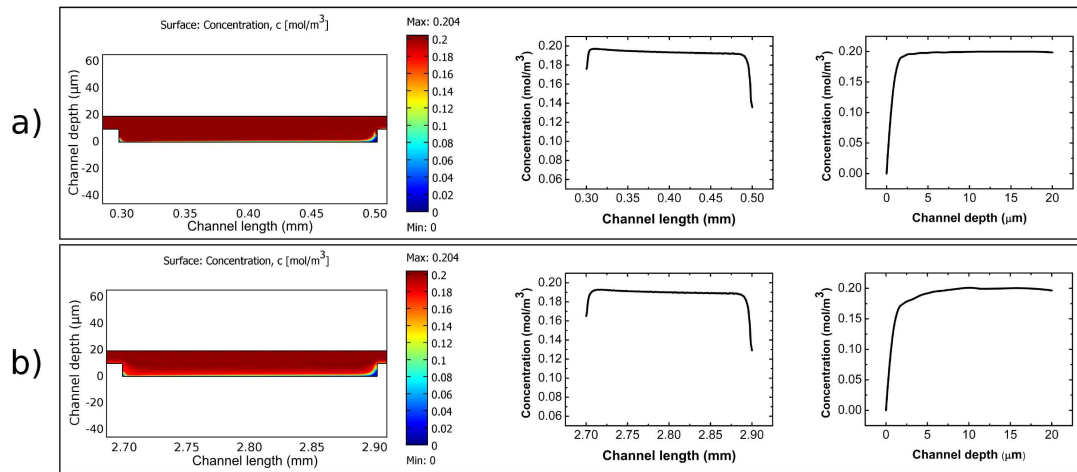


Figure 53 Maps of DNA concentration distribution in the first (a) and last (b) microchambers together with the mean concentration variations versus the length and the depth of the channel. The data have been calculated using an inlet velocity of  $3 \cdot 10^{-2}$  m/s.

Even if higher inlet velocity values could damage the device because they correspond to high pressure values by the Hagen-Poiseuille law, the circuit integrity has been tested up to  $u_0 = 5.4 \cdot 10^{-1}$  m/s. Bio-functionalization experiments repeated by using values equal or greater than  $3 \cdot 10^{-2}$  m/s produced peaks shift of all PSi elements, which differ less than 8% among them [28]. Even if it is not possible to exclude completely the DNA absorption by channel walls, it is reasonable believe that in experiment the surface interaction does not affect the DNA concentration for at least two reasons: PDMS is able to effectively adsorb only small hydrophobic molecules, of the order of hundreds

of Daltons [35], while the DNA probe used has a molecular weight of 7.7 kDa; moreover, DNA is a highly charged hydrophilic molecule with a reduced spontaneous ability to interact with hydrophobic surfaces [36].

In the second simulations the compound formation  $C$  on the porous silicon walls varying the inlet velocity and the diffusion coefficient has been studied. These parameters have been chosen because they do not influence directly the equilibrium complex concentration  $C_{eq}$ . The results about the first and the last PSi element on the channel are exposed in Figure 54.

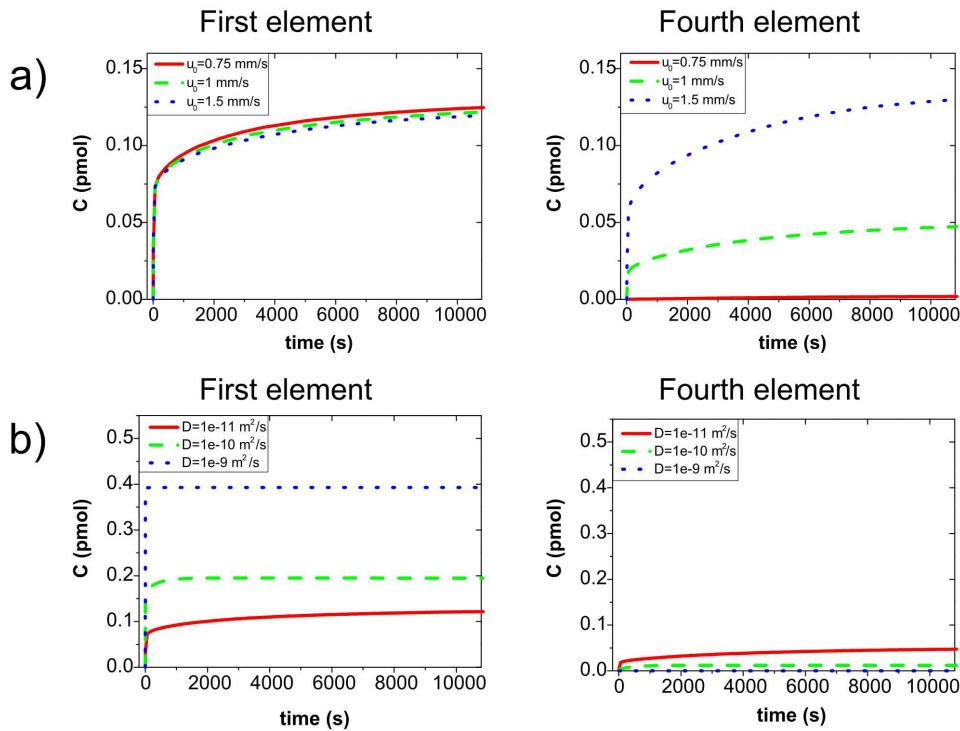


Figure 54 Comparison between the first and last PSi elements for different values of a) inlet velocity and b) diffusion.

The simulation about the binding kinetic has showed that there is a decreasing of the formation of compound  $C$  from the first to the fourth elements. This is caused by a concentration decreasing of chemical species  $A$  in solution along the channel. This effect is reduced by increasing inlet mean velocity until 1.5mm/s reducing slightly the amount of complex  $C$  on the first element. Diffusion also influences strongly the

binding kinetic: an increase of coefficient cause a drastic worsening of uniformity [37,38]. Vice versa a decreasing of coefficient improve the C uniformity along the channel but it can't be taken as a method to obtain a uniform amount of complex linked to the porous silicon walls, because the diffusion of a chemical species can be changed as we want.

### 3.2.3 DNA hybridization

After the bio-functionalization with DNA probe, the DNA-DNA hybridization has been studied by injecting into the microchannel 200  $\mu\text{M}$  of complementary sequence. Figure 55 shows the reflectivity spectra of a P*Si* Bragg reflector before the functionalization process, after the DNA functionalization, and after the complementary DNA interaction.

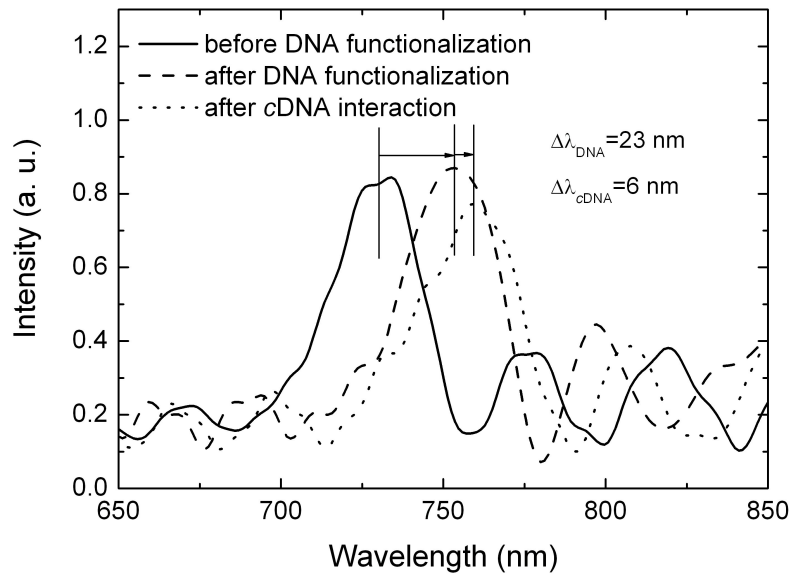


Figure 55 Reflectivity spectra of a P*Si* element before (solid line) and after (dashed line) the DNA probe attachment, and after (dotted line) the hybridization with the complementary DNA.

A red-shift of  $6.0 \pm 0.2$  nm can be detected after the specific DNA-DNA interaction by the first P*Si* element, while an average red-shift of  $5 \pm 1$  nm has been recorded by the other three. A negligible shift, less than 0.2 nm (data not reported in the figure), is the result of a control measurement, which has been done exposing another

functionalized microchannel to non-complementary DNA, demonstrating that the integrated PSi array is able to discriminate between complementary and non-complementary interactions. In a previous work, the sensitivity of an optical PSi based DNA hybridization sensor has been experimentally estimated obtaining the value 1.1 nm/ $\mu$ M, which corresponds to a limit of detection of few nM hundreds, in case of a 0.2 nm resolution on the wavelength shift [24]. This value is of the same order of those reported for other DNA biosensors realized using different technologies. [39,40]. A low variability among results of DNA-DNA recognition experiments is a key issue for microarrays application in immunoassays diagnostic or proteomics: the DNA hybridization has been followed by others microfluidic PSi arrays, realized using the same fabrication process previously reported, obtaining results comparable with those shown in Figure 55. In particular, by averaging over these results, a standard deviation of 4 nm has been estimated for the spectrum red-shift due to the DNA functionalization, while a standard deviation of 1 nm has been calculated for the red-shift related to the DNA-cDNA interaction [28].

## References

- [1] K.-K. Liu, R.-G. Wu, Y.-J. Chuang, H.S. Khoo, S.-H. Huang, F.-G. Tseng, *Microfluidic Systems for Biosensing, Sensors*. 10 (2010) 6623-6661.
- [2] J. Godin, C. Chen, S.H. Cho, W. Qiao, F. Tsai, Y. Lo, *Microfluidics and photonics for Bio-System-on-a-Chip: A review of advancements in technology towards a microfluidic flow cytometry chip, Journal of Biophotonics*. 1 (2008) 355-376.
- [3] A.A.R. Neves, A. Camposeo, S. Pagliara, R. Saija, F. Borghese, P. Denti, et al., *Rotational dynamics of optically trapped nanofibers, Opt. Express*. 18 (2010) 822-830.
- [4] O.M. Maragó, F. Bonaccorso, R. Saija, G. Privitera, P.G. Gucciardi, M.A. Iatì, et al., *Brownian Motion of Graphene, ACS Nano*. 4 (2010) 7515-7523.
- [5] K.M. Hansen, T. Thundat, *Microcantilever biosensors, Methods*. 37 (2005) 57-64.
- [6] J. Homola, *Present and future of surface plasmon resonance biosensors, Analytical and Bioanalytical Chemistry*. 377 (2003) 528-539.

- [7] L. De Stefano, P. Arcari, A. Lamberti, C. Sanges, L. Rotiroti, I. Rea, et al., DNA Optical Detection Based on Porous Silicon Technology: from Biosensors to Biochips, *Sensors*. 7 (2007) 214-221.
- [8] I. Rea, A. Lamberti, I. Rendina, G. Coppola, M. Gioffre, M. Iodice, et al., Fabrication and characterization of a porous silicon based microarray for label-free optical monitoring of biomolecular interactions, *Journal of Applied Physics*. 107 (2010) 014513-014513-4.
- [9] H. Parsa, C.D. Chin, P. Mongkolwisetwara, B.W. Lee, J.J. Wang, S.K. Sia, Effect of volume- and time-based constraints on capture of analytes in microfluidic heterogeneous immunoassays, *Lab Chip*. 8 (2008) 2062.
- [10] D.R. Kim, X. Zheng, Numerical Characterization and Optimization of the Microfluidics for Nanowire Biosensors, *Nano Letters*. 8 (2008) 3233-3237.
- [11] C.-K. Yang, J.-S. Chang, S.D. Chao, K.-C. Wu, Two dimensional simulation on immunoassay for a biosensor with applying electrothermal effect, *Appl. Phys. Lett.* 91 (2007) 113904.
- [12] C.-T. Huang, C.-P. Jen, T.-C. Chao, W.-T. Wu, W.-Y. Li, L.-K. Chau, A Novel Design of Grooved Fibers for Fiber-Optic Localized Plasmon Resonance Biosensors, *Sensors*. 9 (2009) 6456-6470.
- [13] G. Hu, Y. Gao, D. Li, Modeling micropatterned antigen-antibody binding kinetics in a microfluidic chip, *Biosensors and Bioelectronics*. 22 (2007) 1403-1409.
- [14] H.H. Lee, J. Smoot, Z. McMurray, D.A. Stahl, P. Yager, Recirculating flow accelerates DNA microarray hybridization in a microfluidic device, *Lab Chip*. 6 (2006) 1163.
- [15] O. Srivannavit, M. Gulari, Z. Hua, X. Gao, X. Zhou, A. Hong, et al., Microfluidic reactor array device for massively parallel in situ synthesis of oligonucleotides, *Sensors and Actuators B: Chemical*. 140 (2009) 473-481.
- [16] D.G. Myszka, Survey of the 1998 optical biosensor literature, *J. Mol. Recognit.* 12 (1999) 390-408.
- [17] E. Orabona, I. Rea, I. Rendina, L.D. Stefano, Numerical Optimization of a Microfluidic Assisted Microarray for the Detection of Biochemical Interactions, *Sensors*. 11 (2011) 9658-9666.
- [18] L.K. Chin, A.Q. Liu, C.S. Lim, C.L. Lin, T.C. Ayi, P.H. Yap, An optofluidic volume refractometer using Fabry-Pérot resonator with tunable liquid microlenses, *Biomicrofluidics*. 4 (2010) 024107.
- [19] Y. Chen, L. Lei, K. Zhang, J. Shi, L. Wang, H. Li, et al., Optofluidic microcavities: Dye-lasers and biosensors, *Biomicrofluidics*. 4 (2010) 043002.
- [20] A.Q. Jian, X.M. Zhang, W.M. Zhu, M. Yu, Optofluidic refractometer using resonant optical tunneling effect, *Biomicrofluidics*. 4 (2010) 043008.
- [21] L. De Stefano, D. Alfieri, I. Rea, L. Rotiroti, K. Malecki, L. Moretti, et al., An integrated pressure-driven microsystem based on porous silicon for optical monitoring of gaseous and liquid substances, *Physica Status Solidi (a)*. 204 (2007) 1459-1463.
- [22] L. De Stefano, K. Malecki, F.G. Della Corte, L. Moretti, I. Rea, L. Rotiroti, et al., A Microsystem Based on Porous Silicon-Glass Anodic Bonding for Gas and Liquid Optical Sensing, *Sensors*. 6 (2006) 680-687.

- [23] L. De Stefano, P. Arcari, A. Lamberti, C. Sanges, L. Rotiroti, I. Rea, et al., DNA Optical Detection Based on Porous Silicon Technology: from Biosensors to Biochips, *Sensors*. 7 (2007) 214-221.
- [24] E. De Tommasi, L. De Stefano, I. Rea, V. Di Sarno, L. Rotiroti, P. Arcari, et al., Porous Silicon Based Resonant Mirrors for Biochemical Sensing, *Sensors*. 8 (2008) 6549-6556.
- [25] R. Dootz, A.C. Toma, T. Pfohl, Structural and dynamic properties of linker histone H1 binding to DNA, *Biomicrofluidics*. 5 (2011) 024104.
- [26] N. Sperelakis, *Cell Physiology Source Book, Third Edition: Essentials of Membrane Biophysics*, 3rd ed., Academic Press, 2001.
- [27] R.M. Robertson, S. Laib, D.E. Smith, Diffusion of isolated DNA molecules: Dependence on length and topology, *Proceedings of the National Academy of Sciences*. 103 (2006) 7310 -7314.
- [28] I. Rea, E. Orabona, A. Lamberti, I. Rendina, L. De Stefano, A microfluidics assisted porous silicon array for optical label-free biochemical sensing, *Biomicrofluidics*. 5 (2011) 034120.
- [29] H. Ouyang, C.C. Striemer, P.M. Fauchet, Quantitative analysis of the sensitivity of porous silicon optical biosensors, *Applied Physics Letters*. 88 (2006) 163108.
- [30] R.E. Beck, J.S. Schultz, Hindered Diffusion in Microporous Membranes with Known Pore Geometry, *Science*. 170 (1970) 1302 -1305.
- [31] S. Sundaresan, Modeling the hydrodynamics of multiphase flow reactors: Current status and challenges, *AIChE Journal*. 46 (2000) 1102-1105.
- [32] J. Salonen, V.-P. Lehto, Fabrication and chemical surface modification of mesoporous silicon for biomedical applications, *Chemical Engineering Journal*. 137 (2008) 162-172.
- [33] N.H. Voelcker, I. Alfonso, M.R. Ghadiri, Catalyzed Oxidative Corrosion of Porous Silicon Used as an Optical Transducer for Ligand–Receptor Interactions, *ChemBioChem*. 9 (2008) 1776-1786.
- [34] G. Hu, Y. Gao, D. Li, Modeling micropatterned antigen-antibody binding kinetics in a microfluidic chip, *Biosensors and Bioelectronics*. 22 (2007) 1403-1409.
- [35] M.W. Toepke, D.J. Beebe, PDMS absorption of small molecules and consequences in microfluidic applications, *Lab Chip*. 6 (2006) 1484-1486.
- [36] C. Wittmann, S. Alegret, *Immobilisation of DNA on chips*, Springer Science & Business, 2005.
- [37] E. Orabona, I. Rea, I. Rendina, L. De Stefano, Modelling biochemical interactions in a microfluidic assisted porous silicon microarray for optical sensing, in: *2011 International Workshop on BioPhotonics, IEEE*, 2011: pp. 1-3.
- [38] E. Orabona, I. Rea, I. Rendina, L. De Stefano, A porous silicon based microfluidic array for the optical monitoring of biomolecular interactions, in: *Proceedings of SPIE Vol. 8073; Optical Sensors 2011*, 2011: pp. 807314-807314-6.
- [39] T.M.A. Gronewold, A. Baumgartner, E. Quandt, M. Famulok, Discrimination of Single Mutations in Cancer-Related Gene Fragments with a Surface Acoustic Wave Sensor, *Anal. Chem*. 78 (2006) 4865-4871.

- [40] Y. Uludağ, X. Li, H. Coleman, S. Efstathiou, M.A. Cooper, Direct acoustic profiling of DNA hybridisation using HSV type 1 viral sequences, *Analyst*. 133 (2007) 52-57.

# Chapter 4

## A microfluidic circuit for synthetic biology

Synthetic biology concerns the design and realization of new biological systems, and their functions, which cannot be found in nature. It is a new area of biological research that needs strong multi-disciplinarity, linking several science and technical fields. Microfluidics usefulness for classic biology research is a well-known reality, and new prospective are also opening for synthetic biology [1]. Microfluidic is for example a perfect tool for the cell culture due to spatial and temporal control of cell growth. In this chapter an integrated computational and experimental strategy based on a microfluidic device to achieve control of a synthetic biological system has been proposed. This theoretical and experimental strategy has been applied to study and model a synthetic network constructed in yeast cells and has been published in two proceedings:

- “A Microfluidic Device for the Real-Time control of a Synthetic Gene Network”  
E. Orabona, F. Menolascina, L. De Stefano, D. di Bernardo; Network tools and applications in biology NETTAB-BCC 2010 - Biological Wikis, Aracne;
- “An optical microsystem for cell monitoring“ E. Orabona, F. Menolascina, L. De Stefano D. di Bernardo; 3rd EOS Topical Meeting on Optical Microsystems (O $\mu$ S'09), 2009;

### 4.1 Cells culturing in microfluidic devices

Over the past decade, microfluidics has emerged as a technology with the potential to make significant impact on cell biology research. The ability to manipulate small volumes of fluid in micron-sized channels, capillaries, and other geometries has led to

new methods of designing and performing biological experiments, and is paving the way for innovative approaches to understand fundamental biology. Microfluidic devices are becoming increasingly high-throughput, integrated, and close to the realization of lab-on-a-chip systems that were promised at the beginning of the microfluidics revolution. Although research in microfluidics was initially dominated by studies in chemistry, and by analyses of physics at the microscale, the integration of cell biology with microfluidics has recently become a major focus within the scientific community. The initial motivation to study chemical and physical phenomena in microfluidics was borne out of an inherent need to first understand the fundamental aspects at the microscale before starting on research work that involved complex biological systems, such as a living cell. But once knowledge was made available on how to exploit the chemical and physical aspects of microfluidics, it was natural for microfluidics and biology to intersect and establish its own area of interdisciplinary research. Cells and their internal structures have physical dimensions on the order of microns, and thus can be suitably manipulated, tested and probed in microfluidic environments using tools developed with microscale technology. In moving from macro- to microscale, there is an incredible control ability over spatial and temporal gradients and patterns that cannot be realized in conventional Petri dishes and well plates. It is necessary to understand the intricacies of the cell microenvironment, how it differs across physical scales *in vitro*, and how best to control it using benefits of the microscale to merge biology and microfluidic in a new fascinating science [2].

So far, progress in the area of biology-related microfluidic systems has been mostly in proof-of-principle demonstrations, with large research efforts toward testing the behavior of various cell types in different geometries and on different platforms. However, general progress has been somewhat hindered by the lack of a complete understanding of why living cells behave differently when moved from macroscale culture to confined microscale geometries. Culturing cells in microfluidic devices requires an understanding of certain fundamental principles that span multiple disciplines, including biology, biochemistry, physics and engineering. Cell culture techniques cannot be directly transferred to microfluidic environments without

consideration of the physics of the microscale. It is rather important to remember that only a century ago the idea of cultivating a living cell outside of a living organism was met with enormous scepticism and resistance. Today, cell culture is part of a huge biotechnology industry that relies on it for mass production of proteins and vaccines, and preparation of cell-based assays for drug screening applications. Moreover, cell culture techniques are an integral part of fundamental and applied cell biology research. Much of our current understanding of biology comes from *in vitro* experimentation with cells in Petri dishes and well plates: biology laboratories spend significant amounts of effort and resources on designing and performing experiments based on the *in vitro* methods that are available to them.

Proponents of *in vivo* methodology often cite as a major weakness of *in vitro* techniques the inability of a Petri dish to fully capture all the aspects of the *in vivo* cellular microenvironment. Cell culture allows the researcher to isolate specific factors for experimentation outside the complex *in vivo* microenvironment. By doing so, scientists can make logical hypotheses of the effects of those factors, and through controlled experimentation elucidate the mechanisms that regulate cell function. The goal in cell culture is twofold: to recapitulate as closely as possible the cellular microenvironment while also maintaining enough simplicity so that experimental replicates can be performed to achieve statistically significant results in a reasonable amount of time.

Microfluidic platforms are tools that are gaining popularity for studying cellular biology. These devices have achieved amazing progress in application to cell culture in recent years and allow to realize a precise control of the environment surrounding individual cells. Cultured cells are used in a variety of contexts such as cell biology, synthetic biology, tissue engineering, biomedical engineering, and pharmacokinetics for drug development. Cells exist *in vivo* in carefully maintained microenvironments within the three dimensional cell communities. Cells grow through interactions and communication with other cells within the living organisms that have complex and well organized two-dimensional (2D) or three-dimensional (3D) microscale systems composed of multilayers, membranes, protein channels, and many other elements. Current *in vitro* cell culture environments lack the richness required to successfully

mimic their *in vivo* counterparts. As most cell-based biological research is performed by isolating cells, placing them in a culture flask with medium, and then incubating the culture flask, there are no cellular structures to be adhered to in the culture dish and no other cell types with which to interact *in vitro* cultured cells. Consequently, *in vitro* cultured cells frequently alter their cellular properties related to their growth rate, morphology, and intracellular metabolic activities. Therefore, novel approaches are needed to establish a more *in vivo*-like microenvironment than presently available.

Microtechnology can facilitate the study of cell behavior *in vitro* because it provides the necessary tools for recreating *in vivo*-like micro environments. Therefore, microfluidic devices for cell culture studies are rapidly gaining importance in drug development and biological research applications, such as drug toxicity or metabolism studies, and stem cell differentiation studies [3]. Microfluidic systems offer the ability to create cell-cell, cell-substrate, and cell-medium interactions with a high degree of precision. Such environment is analogous to *in vivo* conditions: the small size of the channels permit nutrients to diffuse to nutrient-poor areas. Moreover, microfluidic technology can be used to supply and transfer media, buffers, and even air while the waste products by cellular activities are drained in a way resembling the human circulatory system. Therefore, microfluidic cell culture systems have the ability to precisely control the environment around individual cells that cannot be achieved under traditional culture conditions and offer numerous benefits (Table 7) [4]. Three different microfluidic cell culture systems are generally considered: micropatterned cell culture on substrate surface, microchannels cell culture and microchambers cell culture [5].

### **Culture cells on micropatterned substrates surface**

Advances in microfabrication and microfluidic technology have allowed highly controlled cellular micropatterning. Microscale cell patterns are commonly obtained by culturing cells on a substrate having a pattern with cell adhesive and non-adhesive regions molecule. Two examples of microscale cell patterns are illustrated in Figure 56 [6].

| Property of microfluidic systems                                     | Benefit for cell culture   |
|--|--|
| Small chip size and microchannels on the cellular length scale       | <ul style="list-style-type: none"> <li>- reduced sample/reagent consumption</li> <li>- numerous cells coculture in a single device</li> <li>- faster transfer of cell culture medium and heat, i.e. short equilibration time</li> </ul>  |
| 2D or 3D network structure   | Simulating in-vivo cell growth and development   |
| The feasibility to integrate multiple microfluidic devices on a chip | <ul style="list-style-type: none"> <li>- Integrate with fluid handling operations for efficient and high throughput cellular analysis</li> <li>- Integrate with detection functionality for in situ monitoring of cellular events</li> <li>- Integrate with heating functionality for temperature control of the cellular microenvironment etc.</li> </ul> |
| Material transparency  | Observation and monitoring of cellular events in real-time by microscope and fluorescent measurement.  |

Table 7 Benefit for cell culture provided by microfluidic systems.

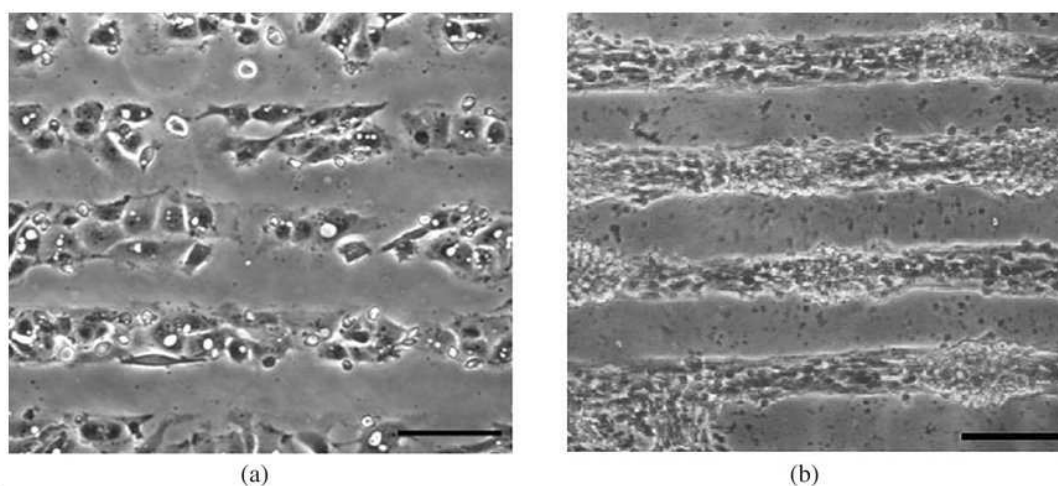


Figure 56 Micro-scale cell patterns. The cell patterns were obtained on PDMS substrates patterned for (a) epithelial cells and (b) chick forebrain cells.

Adhesion and cell-to-cell communication is currently the most studied area of microscale biology and this can be studied mimicking in vivo-like the patterning cells capabilities. Although photolithography is one of the most well-established techniques

for microfabrication, its application in protein or cell patterning is more expensive and less bio-compatible than soft lithography technique. Typically, a soft lithographic method has been used to fabricate microstructures that are moulded with a patterned PDMS stamp by means of capillary force for protein and cell patterning. This method can make the cells arranged according to the pattern, the moulded structure acts as a physical and biological barrier or the adhesion of proteins and cells and the exposed substrate surface acts as adsorption promoters. Since conventional techniques for preparing patterned substrates require complex surface chemistry to immobilize both cells adhesive molecules and inhibitory molecule patterns on the cell culture substrate surface, a microcontact printing technique is used to create patterns on PDMS substrates to permit cell attachment and growth, and exploited the natural tendency of PDMS to inhibit cell adhesion.

### **Culture cells in microchannels**

Microfluidic channels are especially attractive since they can be easily multiplexed with integrated fluid handling operations for efficient and high throughput cellular analysis, imaged for in situ monitoring of cellular events, and can recapitulate a physiological cellular microenvironment with controllable distribution of biochemical molecules and shear stresses at the cellular resolution. Cells have been cultured within microenvironments specifically to observe cell behaviour in the confines of a microchannel. An example is illustrated in Figure 57 [7].

### **Culture cells in microchambers**

The in vivo tissue environment can be described by convective transport of nutrients in capillary vessels that are in close proximity with cells (usually within 100  $\mu\text{m}$ ). Culture cells in microchambers that etched in microchip can provide a stable cell culture microenvironment and enable parallel and high throughput cellular research. Several microfluidic cell culture systems have incorporated an array of simple chambers, which have been designed to simulate the mass transfer characteristics of the in vivo tissue environment and diffusive transport across the interstitial space to individual cells.

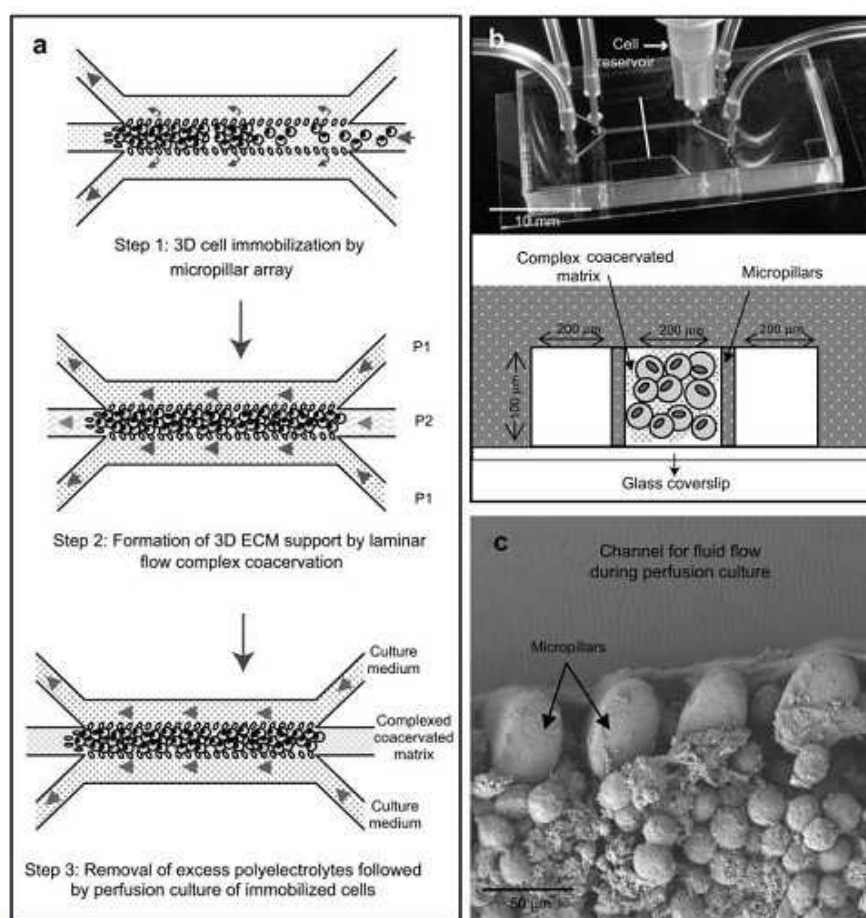


Figure 57 A 3D microfluidic channel-based cell culture system. (a) Cells were three-dimensionally immobilized in a microfluidic channel by dynamic seeding through a micropillar array. (b) Prototype with a cross-sectional illustration (indicated by white line). (c) SEM micrograph of hepatocytes three-dimensionally immobilized in a microfluidic channel with an array of elliptical micropillars.

Some microfluidic perfusion culture systems use cell culture chambers that are isolated from the bulk fluid flow so that cells are not subjected to direct convective flow. In such designs, mass transport distances are similar in all directions, resulting in more uniform microenvironment for cell growth. In Figure 58 is illustrated a  $10 \times 10$  microfluidic cell culture array was bonded to a coverglass and mounted on a transparent ITO heater [8].

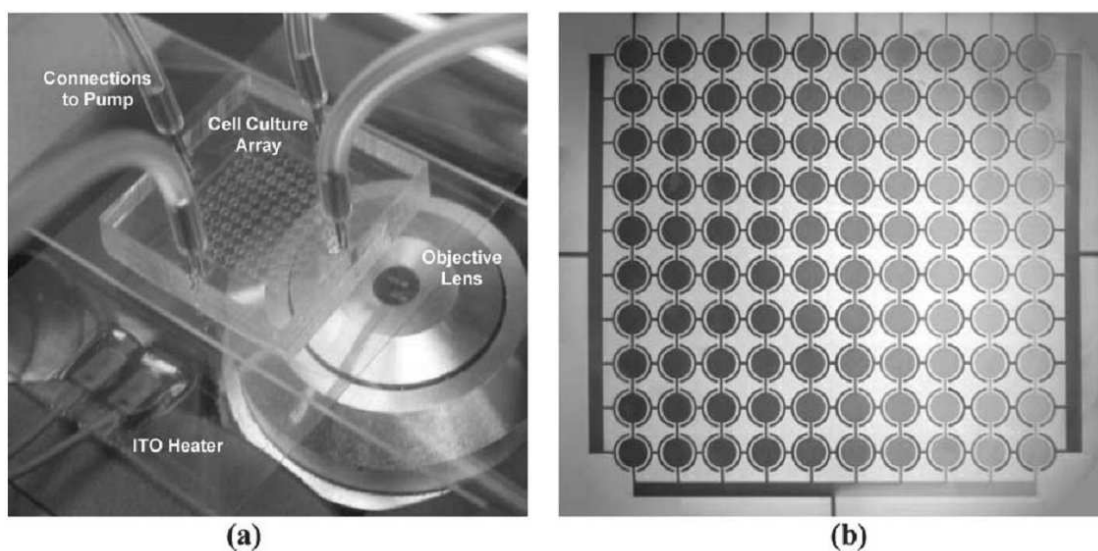


Figure 58 Pictures of a 10×10 microfluidic cell culture array.

## 4.2 In vitro testing of a genetic network

The development of high-throughput data-collection techniques, as microarrays, allows for the simultaneous interrogation of the status of a cell's components at any given time. In turn, new technology platforms, such as protein chips help to determine how and when these molecules interact with each other. Various types of interaction networks, (including protein–protein interaction, metabolic, signalling and transcription-regulatory networks) emerge from the sum of these interactions. None of these networks are independent, instead they form a 'network of networks' that is responsible for the behaviour of the cell. The theory is the same of complex networks, that has made advances in the past few years uncovering the organizing principles that govern the formation and evolution of various complex technological and social networks. This unexpected universality indicates that similar laws may govern most complex networks in nature, which allows the expertise from large and well-mapped non-biological systems to be used to characterize the intricate relationships that govern cellular functions [9]. Further examples include genetic regulatory networks, in which the nodes are individual genes and the links are derived from the expression correlations that are

based on microarray data, or protein domain networks that are constructed on the basis of protein domain interactions (see Figure 59).

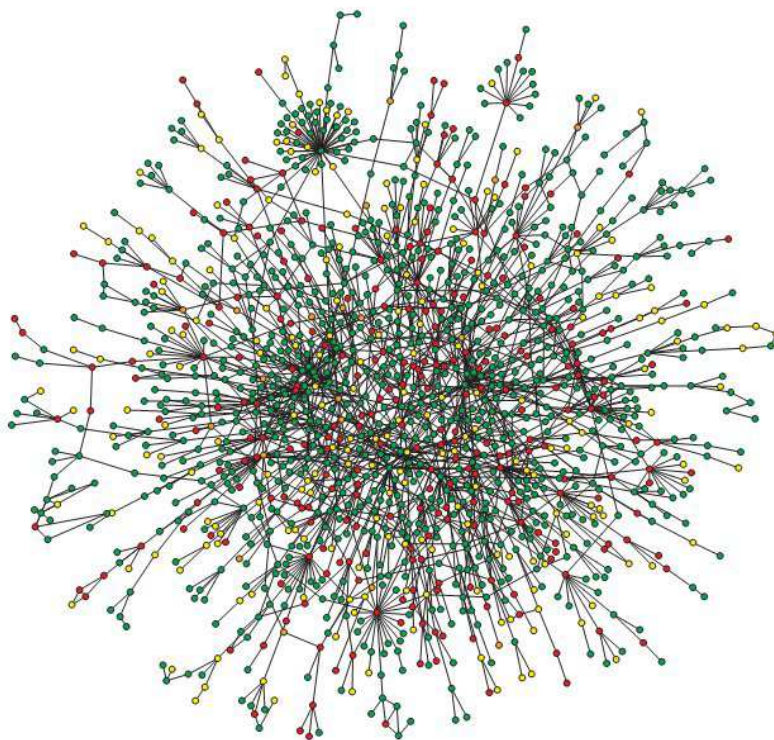


Figure 59 A map of protein–protein interactions in *Saccharomyces cerevisiae*, illustrates that a few highly connected nodes (which are also known as hubs) hold the network together.

In the recent years, the studying and modelling gene networks are become an active research field. In this context, the control of biological networks is an ambitious objective: drive a gene expression at will (e.g. have the cell produce a desired concentration of a protein, or a desired time-evolution of protein concentration) starting from a mathematical model of the biological process, by applying appropriate conditions (for example varying concentration of small molecules). This can be achieved by applying principles from control systems theory to induce gene networks to follow a pre-determined behaviour. Unfortunately, obtaining this result in-vivo is very difficult since a suitable benchmark gene network is needed to test the working hypothesis on, moreover a technological platform needs to be developed to achieve a

fine control over the concentration of input compounds in the extracellular environment and to observe and quantify cell populations dynamics for long experiments ( $t > 24\text{h}$ ) analyzing at regular and frequent time intervals (in the order of minutes). These requirements do not make it trivial and is probably the main reason for previous attempts in this field being mostly computational works.

IRMA (In-vivo Reverse engineering Method Assessment) [10] is a synthetic five-gene network developed in yeast *S. Cerevisiae* meeting all the requirements for a control system benchmark: it is integrated in a eukaryote organism, it is the most complex synthetic network built so far, it can be either switched on or off by galactose or glucose administration and a detailed mathematical model is available for it. All these characteristics rendered IRMA the ideal candidate as benchmark for the testing of a control strategy in-vivo. As a matter of fact, IRMA can be interpreted as an Single Input - Single Output system: galactose and glucose can be used to switch the network ON or OFF respectively and these dynamics can be tracked by estimating the amount of a green fluorescent protein (GFP) fused to the CBF1, one IRMA's genes. IRMA has been developed as a testbed synthetic network in yeast for the design and validation of reverse engineering and modelling approaches [11–13]. Its diagram of genomic interaction is illustrated in Figure 60. A new hybrid dynamical model describing the behaviour of the synthetic circuit has been derived. Four alternative control strategies stemming from classic control theory (namely relay control, both ideal and non-ideal and Pulse Width Modulation (PWM) control, with and without a “Proportional, Integrative, Derivative” (PID) controller) have been designed. These control strategies were designed to achieve two objectives: setpoint regulation and tracking. The objective of setpoint regulation is to produce a desired amount of a protein (GFP), monitored by fluorescence, which the cell cannot achieve by growing only in galactose or in glucose, but only dynamically switching between glucose and galactose administration appropriately. The switching sequence is computed in real-time by the control algorithm following the scheme. The objective of tracking is to produce a desired, but time-varying, concentration of a protein. Again the control algorithm produces the switching sequence.

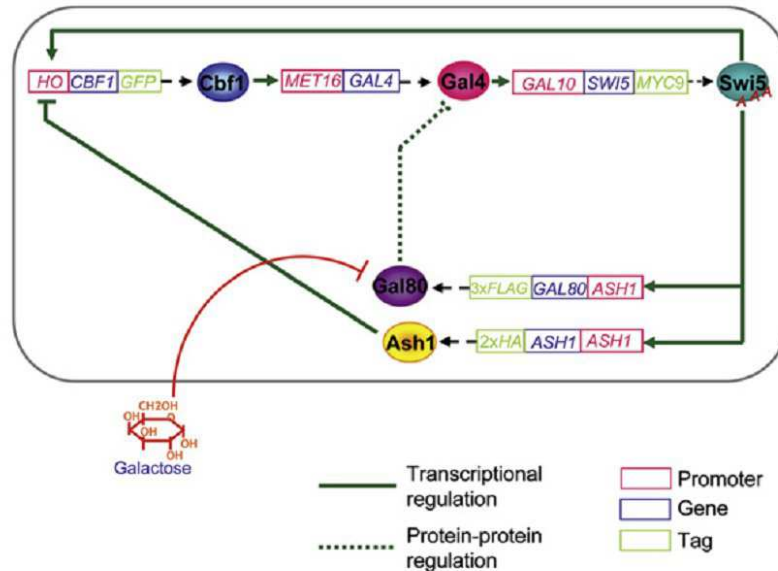


Figure 60 Schematic diagram of genomic integrations of IRMA genes.

The control algorithm has been designed to tackle some of the most common issues found in biological networks namely: non-linearities, transcriptional delays and switch-like transcription activation functions (leading to discontinuities). Therefore, this framework can in principle be applied to a wide variety of control problems in systems biology. In-silico results shown excellent capabilities in terms of both setpoint and tracking error minimization. All of the algorithms have been implemented taking into account the technological platform, thus achieving a full integration of inhomogeneous components like macro-mechanical valves and micro-engineered fluidic devices.

In order to test the in silico results, a simple “open-loop” experiment where the switching sequence accounts for 180 min galactose pulse and 180 min glucose supply has been tested. Cells were imaged at 5 minutes time intervals and GFP-associated fluorescence was quantified as shown in Figure 61.

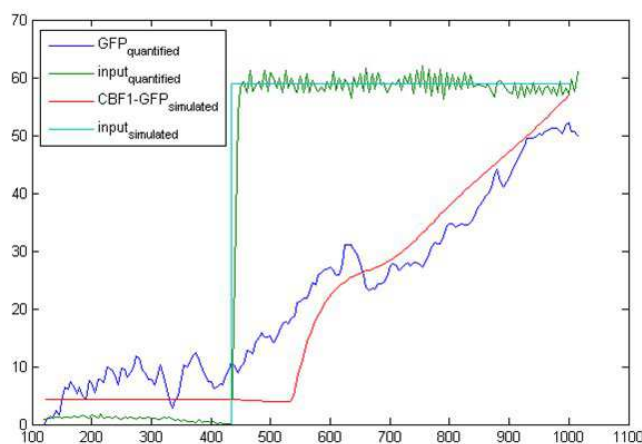


Figure 61 The experimental galactose concentration (in black) and CBF1-GFP cellular concentration (in red) are plotted against the simulated input (in green) and output (in blue) signals.

Numerical estimation of the fluorescence profile over time provided evidence for a satisfactory agreement between theoretical predictions and in-vivo quantification. The full closed-loop experiment, where the switching sequence is computed in real-time, is ongoing. Certainly a control framework will be successfully applied to control the behaviour of living cells and to better investigate complex biological pathways [14].

#### 4.2.1 A microfluidic trap for yeast cells

The developed device is schematized in Figure 62a and it has been realized in polydimethylsiloxane using the replica molding technique fully developed in Chapter 2. Basic operations of this device include cell loading and feeding. The cells loading step is performed injecting them into the outlet port. When an enough number of cells is captured by the “Tesla” microchemostat (Figure 62b) [15] the flow is stopped. The Tesla microchemostat is an improvement of the classic Tesla diode loop [16,17]. The design is such that the side-arm of the loop forms a trapping region that constrains a population of cells to a small area. Fluid flow is used to continuously purge cells that grow beyond the trapping region boundaries so that the device can function as a standard chemostat.

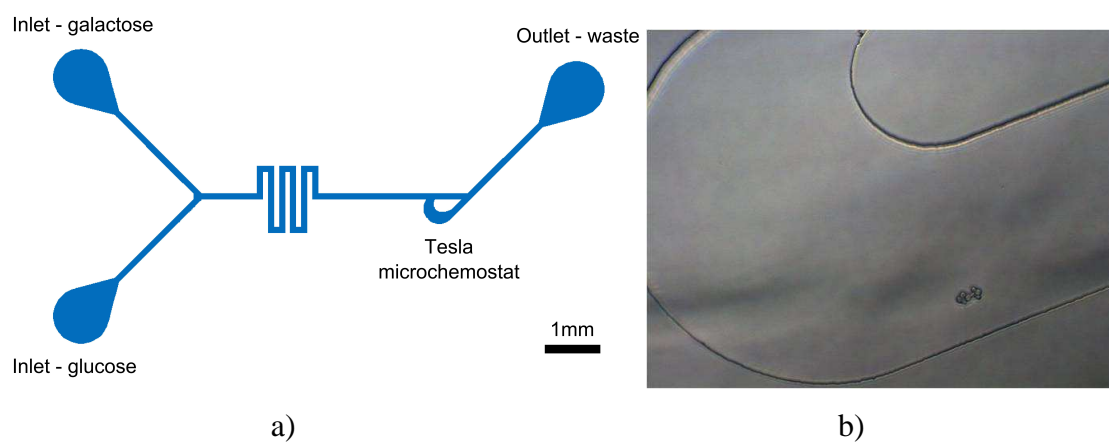


Figure 62 a) microfluidic scheme of the device for yeast cell culture; b) optical microscopic images of Tesla microchemostat with some trapped cells.

After the loading step the stimulation of yeasts is realized by feeding. Two inlets has been realized for galactose and glucose and they can be mixed at will changing relative pressure differences. Relative concentration of compounds is modulated by computer controlled manipulation of the pressure that drives the flow in the common channel. By using this approach it's possible to gain a deep control over chemical concentration sensed by cells. In Figure 63 are illustrated the experimental and simulated mixing ratio for three simple case: only galactose, glucose only, galactose only, and mixed at 50%. The meander channel that follows to the “Y” region is a folded channel to permit complete mixing of molecular species with low area consumption. This device, coupled with an epifluorescence microscope provided with optical autofocus capabilities, allows to operate in “free-run” mode over long time periods without the need for external adjustment. Protein levels can be monitored by GFP, taking advantage of transparency of chip to the optical wavelengths, which has been fused to one of the genes in the cells. In Figure 64 is illustrated the platform implemented for the control algorithm. A computer program encoding the control strategy runs on the PC that controls the valves managing the delivery of the compounds in the microfluidic device.

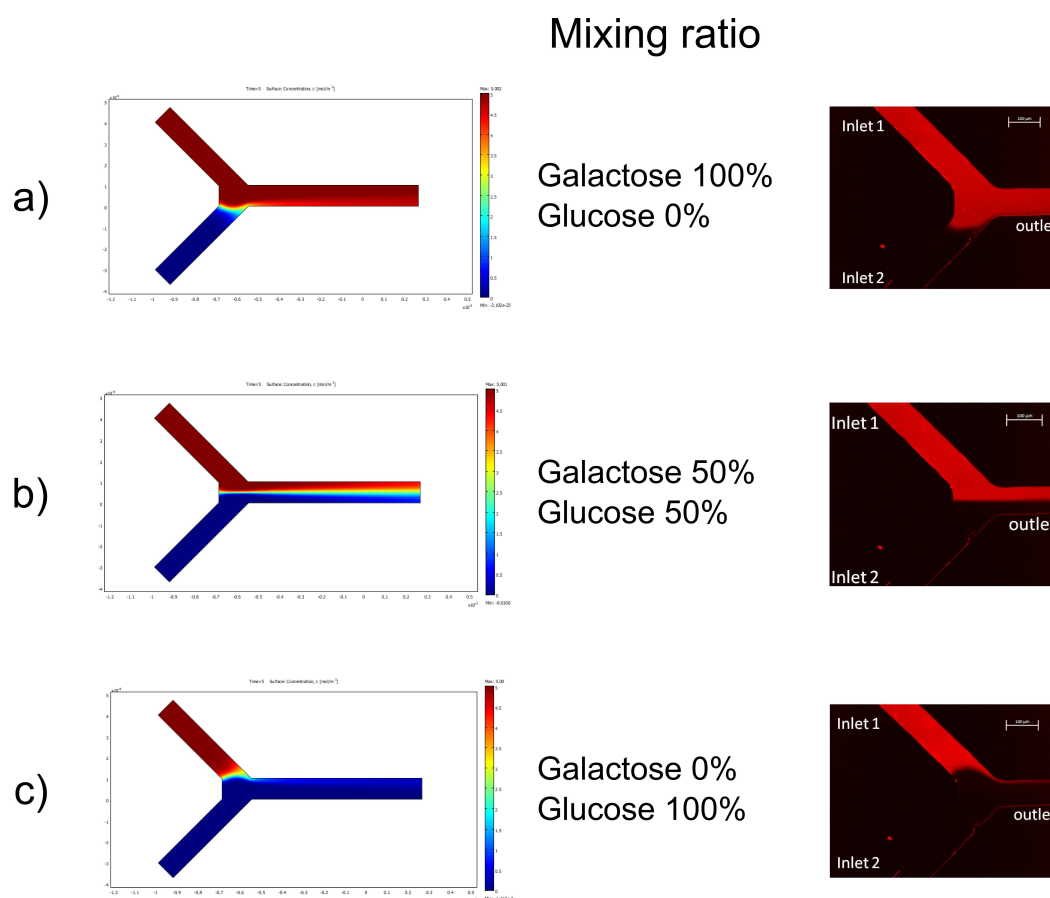


Figure 63 Simulated and experimental mixing ratio for Galactose and Glucose inputs.

The microfluidic chip hosts yeast cells in a specific micro-chamber imaged via an inverted microscope that periodically sends images to the PC. The computer closes the loop by estimating the GFP fluorescence and comparing this signal with the reference one in order to compute the next input signal to be sent to the valves. A variation of the previous design has been realized adding an outlet channel, as illustrated in Figure 65, changing the channels cross from “Y” to “Ψ”. This extra channel is useful to increase the relative pressure difference that should be provided to obtain galactose or glucose feeding only. This bigger difference makes easier to control other intermediate mixing ratios. In this case another meander region has been necessary to increase the channel resistance and in this way to minimize the sample consumption.

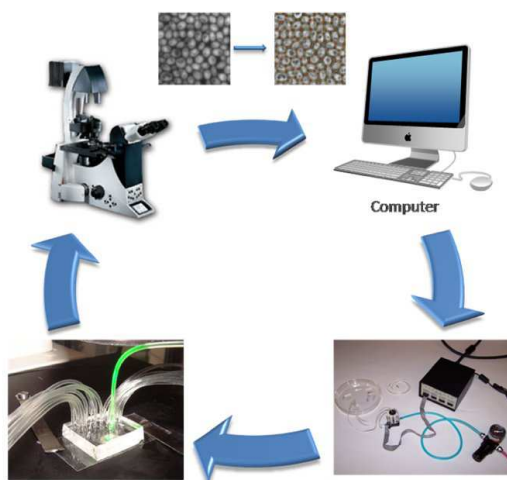


Figure 64 Schematic view of the platform implemented for the control laws.

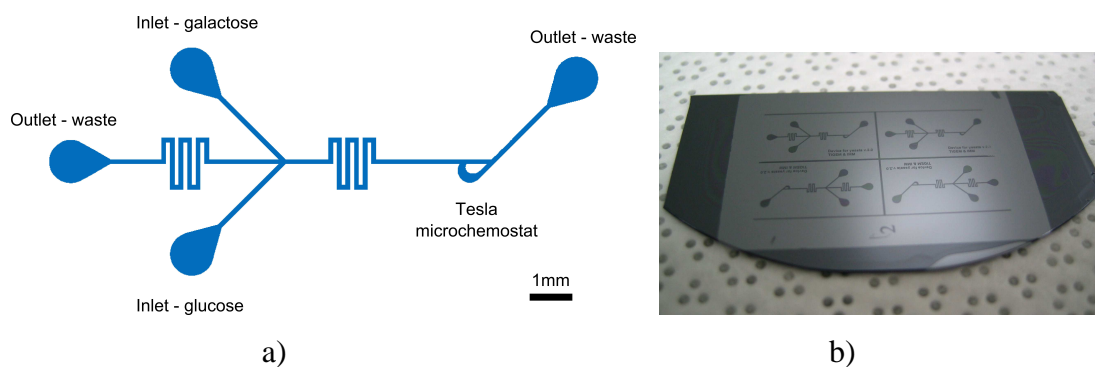


Figure 65 a) microfluidic scheme variation of the device for yeast cells culture with two outlet channels and b) its master in SU-8 on silicon containing 4 devices.

As for the previous configuration a finite element simulation has been performed for fluid dynamics and convection and diffusion equations (Figure 66). Leaving the same pressure values at the inlets the length of the channel necessary to reach the complete mixing of galactose and glucose reduces to half. This happens because the flow velocity decrease to half in the central channel.

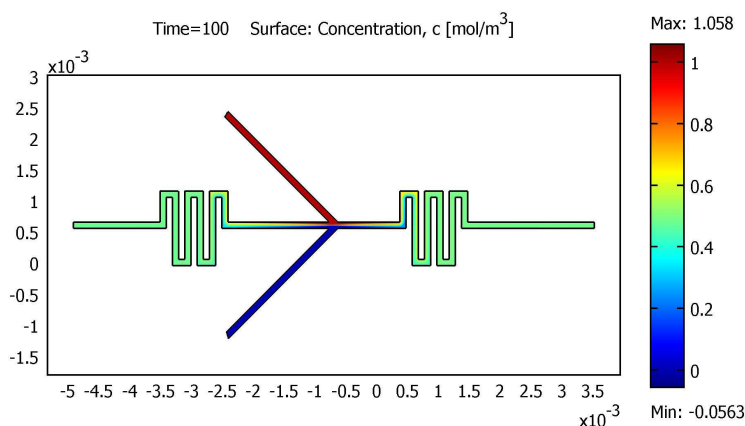


Figure 66 Finite element simulation about convection and diffusion inside the microchannels.

## References

- [1] S. Gulati, V. Rouilly, X. Niu, J. Chappell, R.I. Kitney, J.B. Edel, et al., Opportunities for microfluidic technologies in synthetic biology, *Journal of The Royal Society Interface*. (2009).
- [2] E.W.K. Young, D.J. Beebe, Fundamentals of microfluidic cell culture in controlled microenvironments, *Chem Soc Rev*. 39 (2010) 1036-1048.
- [3] D.J. Beebe, G.A. Mensing, G.M. Walker, Physics and applications of microfluidics in biology, *Annu. Rev. Biomed. Eng.* 4 (2002) 261-286.
- [4] Manguo Huang, Shangchun Fan, Weiwei Xing, Overview and study focuses of microfluidic-based cell culture systems, in: *Fourth International Conference on Bio-Inspired Computing, 2009. BIC-TA '09*, IEEE, 2009: pp. 1-5.
- [5] J. El-Ali, P.K. Sorger, K.F. Jensen, Cells on chips, *Nature*. 442 (2006) 403-411.
- [6] M.N. De Silva, R. Desai, D.J. Odde, Micro-Patterning of Animal Cells on PDMS Substrates in the Presence of Serum without Use of Adhesion Inhibitors, *Biomedical Microdevices*. 6 (2004) 219-222.
- [7] Y.-C. Toh, C. Zhang, J. Zhang, Y.M. Khong, S. Chang, V.D. Samper, et al., A novel 3D mammalian cell perfusion-culture system in microfluidic channels, *Lab Chip*. 7 (2007) 302-309.
- [8] P.J. Hung, P.J. Lee, P. Sabounchi, N. Aghdam, R. Lin, L.P. Lee, A novel high aspect ratio microfluidic design to provide a stable and uniform microenvironment for cell growth in a high throughput mammalian cell culture array, *Lab Chip*. 5 (2004) 44-48.
- [9] A.-L. Barabási, Z.N. Oltvai, Network biology: understanding the cell's functional organization, *Nature Reviews Genetics*. 5 (2004) 101-113.
- [10] I. Cantone, L. Marucci, F. Iorio, M.A. Ricci, V. Belcastro, M. Bansal, et al., A Yeast Synthetic Network for In Vivo Assessment of Reverse-Engineering and Modeling Approaches, *Cell*. 137 (2009) 172-181.

- [11] M. Bansal, V. Belcastro, A. Ambesi-Impiombato, D. di Bernardo, How to infer gene networks from expression profiles, *Mol Syst Biol.* 3 (2007).
- [12] T.S. Gardner, J.J. Faith, Reverse-engineering transcription control networks, *Physics of Life Reviews.* 2 (2005) 65-88.
- [13] T.S. Gardner, D. di Bernardo, D. Lorenz, J.J. Collins, Inferring Genetic Networks and Identifying Compound Mode of Action via Expression Profiling, *Science.* 301 (2003) 102 -105.
- [14] E. Orabona, F. Menolascina, L. De Stefano, D. di Bernardo, A microfluidic device for the Real-Time control of a Synthetic Gene Network, in: *Network Tools and Applications in Biology*, Naples, Italy, 2010.
- [15] S. Cookson, N. Ostroff, W.L. Pang, D. Volfson, J. Hasty, Monitoring dynamics of single-cell gene expression over multiple cell cycles, *Mol Syst Biol.* 1 (2005).
- [16] S. Bendib, Analytical study of microchannel and passive microvalve: application to micropump simulator, in: *SPIE*, 2001: pp. 283-291.
- [17] D.C. Duffy, O.J.A. Schueller, S.T. Brittain, G.M. Whitesides, Rapid prototyping of microfluidic switches in poly(dimethyl siloxane) and their actuation by electro-osmotic flow, *Journal of Micromechanics and Microengineering.* 9 (1999) 211-217.



# Chapter 5

## Electric field mapping in microfluidic devices

Computer aided design, finite element method, and numerical calculations are general tools which can be used for modelling and testing very different microfluidics based devices. The technical and scientific skills exploited for the development of the PhD research project have been used in an experiment in collaboration with the prof. A. Sasso group's, University of Naples "Federico II". The mix of competencies leads to an innovating method for the quantitative mapping generated by microelectrodes, published in G. Pesce, B. Mandracchia, E. Orabona, G. Rusciano, L. De Stefano, A. Sasso, "Mapping electric fields generated by microelectrodes using optically trapped charged microspheres", Lab Chip, 2011, DOI: 10.1039/C1LC20432G.

### 5.1 Electrokinetic transport phenomena

Electrokinetic pumping and particle manipulation are techniques widely used to move liquids and particles at small length scales since they are implemented through surface forces which scale down accordingly to length scales [1,2]. Electrokinetic techniques have the advantage of being easily integrated into microfluidic systems. The application of electric fields to colloids in a fluid can both actuate the liquids as well as the colloids. In a system where colloids are suspended in a media where a controlled electric field exists, the system is subjected to a variety of deterministic forces which it is possible to control as well as stochastic forces that cannot be influenced. The two major electrical forces that exist are electrophoresis and dielectrophoresis. Electrophoresis is the motion of charged matter under the influence of an applied electric field. The direction of

motion is always toward the electrode of opposite charge to that of the particle, and it is of no consequence whether the field is uniform or non-uniform. A double layer is an electric structure that appears on the surface of an object when it is placed into a liquid, and refers to two parallel layers of charge surrounding the object. The first layer, the surface charge (either positive or negative), comprises ions adsorbed directly onto the object due to a host of chemical interactions. The second layer is composed of ions attracted to the surface charge via the coulomb force, electrically screening the first layer. Due to the presence of the double layer, a charged particle when suspended in aqueous solution appears electro-neutral. Despite of this, movement of the particle still occurs due to the mobility of the ions in the double layer. The velocity of a charged particle due to the electric field is a function of the particle's size and charge as well as the viscosity and conductivity of the suspending liquid (i.e. the thickness of the double layer surrounding the particle). The main application of electrophoresis is in the separation of macromolecules such as DNA and proteins, since different macromolecules move with different velocities under the influence of the applied electric field. On the contrary, dielectrophoresis does not occur in a uniform electric field: the net force experienced by a neutral particle is zero. However, if the particle is placed in a non-uniform electric field the resulting force difference across the particle causes it to move. This movement arises due to the variation of the charge density over the particle. The free charges in a liquid system (induced or natural) also undergo a force. Electrokinetic effects are the result of the combined movement, irregular charge distribution and screening at the solid liquid interface [3].

## **5.2 Electric field mapping in microfluidic devices**

As explained in the previous paragraph, microfluidic devices use electrokinetic phenomena to pump, mix, inject, sort, and also to manipulate fluids, cells and particles. In lab-on-a-chip devices electric fields are usually applied by integrated microelectrodes. They are attracting much interest for their possibilities to generate high electric fields from relatively small applied AC potential. They also play an important

role, also for the investigation of sub-millimetre bio-logical structures, even at level of single cells [4]. Measurement of electric fields at microscopic scale is not trivial, and only few experimental measurements of electric fields have been proposed [5]. To overcome this limitation, typical approaches are based on numerical calculations using finite element method software assigning the appropriate boundary conditions. Optical tweezers can be used to measure the effects of electric field on to a charged particle while it is trapped by optical forces. Since both direction and amplitude of electric field generated by micro-electrodes requires the knowledge of the charge of the trapped particle, an absolute measure is possible. The basic idea is to use charged microspheres confined by an optical trap which acts as a sensitive force probe to explore the electric field. The electric field measurement derives from the equilibrium between the electric force ( $qE$ ) and the elastic optical restoring force ( $k\Delta x$ ). Two pairs of electrodes have been combined in the same device to measure the electric field in an aqueous environment: two plane parallel electrodes generate a well defined uniform electric field which has been used to estimate the charge while a second electrodes pair generates the electric field to be determined. The measurement principle is very simple; it is based on the detection of the displacement of the trapped particle from its equilibrium position under the effect of the external electric force. The particle displacement was measured in the three dimensions with nanometer precision using the back focal plane interferometry detection technique [6]. A detailed mapping of electric field has been performed moving the position of the optical tweezers (Figure 67).

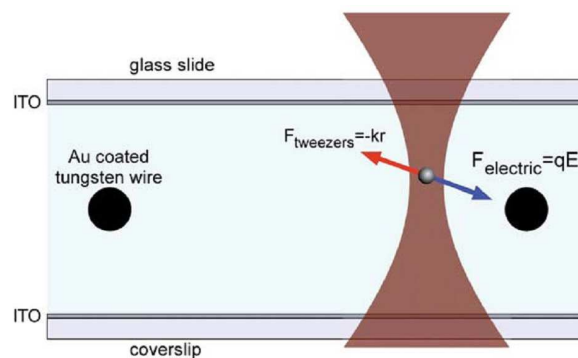


Figure 67 Scheme illustrating how a charged polystyrene bead held in an optical trap acts as a probe to measure amplitude and direction of an electric field.

It's important to note that in polar solutions like water, even for distilled deionized water (conductivity  $1.0 \mu\text{S}/\text{cm}$ ), the number of free ions is high enough to generate a double-layer around the electrodes that screens them, drastically reducing the electric field amplitude. Thus in polar solutions, static measurements are impossible and it is necessary to use alternating fields with oscillation frequency higher than the transit time of free ions in solution. The analysis of the trapped charged bead motion gives the amplitude of the force exerted on it. Nevertheless the oscillatory motion can be masked by the thermal motion when the electric field strength is particular low. To extract the oscillation amplitude the Power Spectral Density or the Auto Correlation Function can be used [7]. Therefore, using the same particle it's possible to determine both its charge and the distribution of the electric field. In this experiment two electrodes geometries has been used: a wire-wire geometry and a wire-plane geometry. In both cases the experimental results are compared with those obtained by numerical simulations. The experimental setup (Figure 68) comprises an homemade optical microscope with a high-numerical-aperture water-immersion objective lens ( $\text{NA}=1.2$ ) and a frequency and amplitude stabilized Nd-YAG laser ( $\lambda = 1.064 \mu\text{m}$ , 500 mW maximum output power) for the optical tweezers.

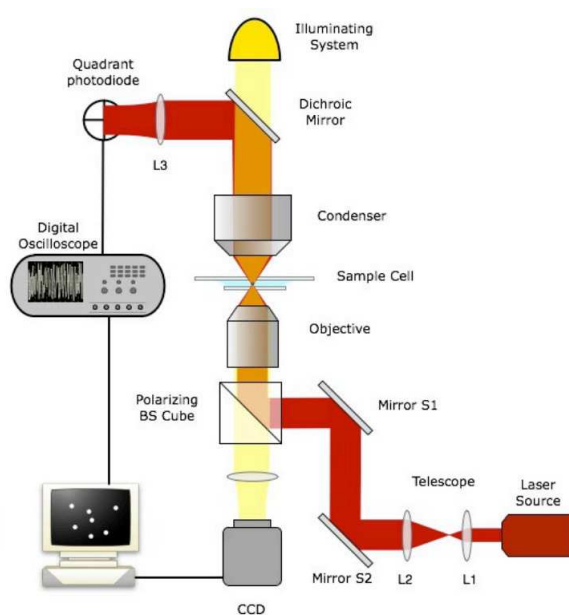


Figure 68 Experimental setup.

The particles were chosen negatively charged, sulphate coated polystyrene microspheres ( $1.06\text{g/cm}^3$  density, 1.65 refractive index) with a diameter of  $1.00\pm 0.05\mu\text{m}$ , and were diluted in distilled deionized water to a final concentration of a few particles/ $\mu\text{l}$ . The surface charge density, provided by the manufacturer, was  $5.7\ \mu\text{C/cm}^2$  that corresponds to a total charge of  $1.79\cdot 10^{-13}\ \text{C}$ . However due to screening effects of the polar solvent, the effective charge of the particles is less than the nominal value and has to be measured before using them as probes. A droplet of such solution ( $100\mu\text{l}$ ) is placed inside a sample chamber made of a  $150\ \mu\text{m}$ -thick coverslip and a microscope slide, both coated with a transparent conductive layer (Indium-Tin-Oxyde) that act as planar electrodes. The microfluidic device was mounted on a piezoelectric stage, which allows movements with nanometer resolution. The 3D particle position was monitored through the forward scattered light imaged on a quadrant photodiode (QPD) at the back focal plane of the condenser lens, using a digital oscilloscope for data-acquisition. The QPD-response was linear for displacements up to  $300\ \text{nm}$  ( $2\ \text{nm}$  resolution,  $250\ \text{kHz}$  bandwidth). First the charge of the trapped bead has been measured using the two ITO coated glasses that generated a uniform electric field whose amplitude was  $E=V/h \sim 2.7\ \text{kV/m}$ ; ( $h=185\ \mu\text{m}$ ). The effective charge measured was  $(1.03\pm 0.07)\times 10^{-16}\ \text{C}$ , that is about 2000 times smaller than the value reported by the manufacturer. This is due to the screening caused by the double-layer around the surface of the bead. This value remained constant within experimental errors for several hours. To check the uniformity of this field the bead motion at several position over a wide area of about  $500\times 500\mu\text{m}^2$  have been recorded, the electric field resulted to be uniform within the experimental error both in amplitude and direction. It is worth to note that the laser field induces a polarization of the trapped dielectric particle, but this effect is negligible since the value of the charge changing the intensity of the laser beam has been measured without observing any relevant difference. In the first geometry (see Figure 69a) a gold coated tungsten wire with a diameter of  $10\ \mu\text{m}$  and the bottom ITO coverslip have been used.

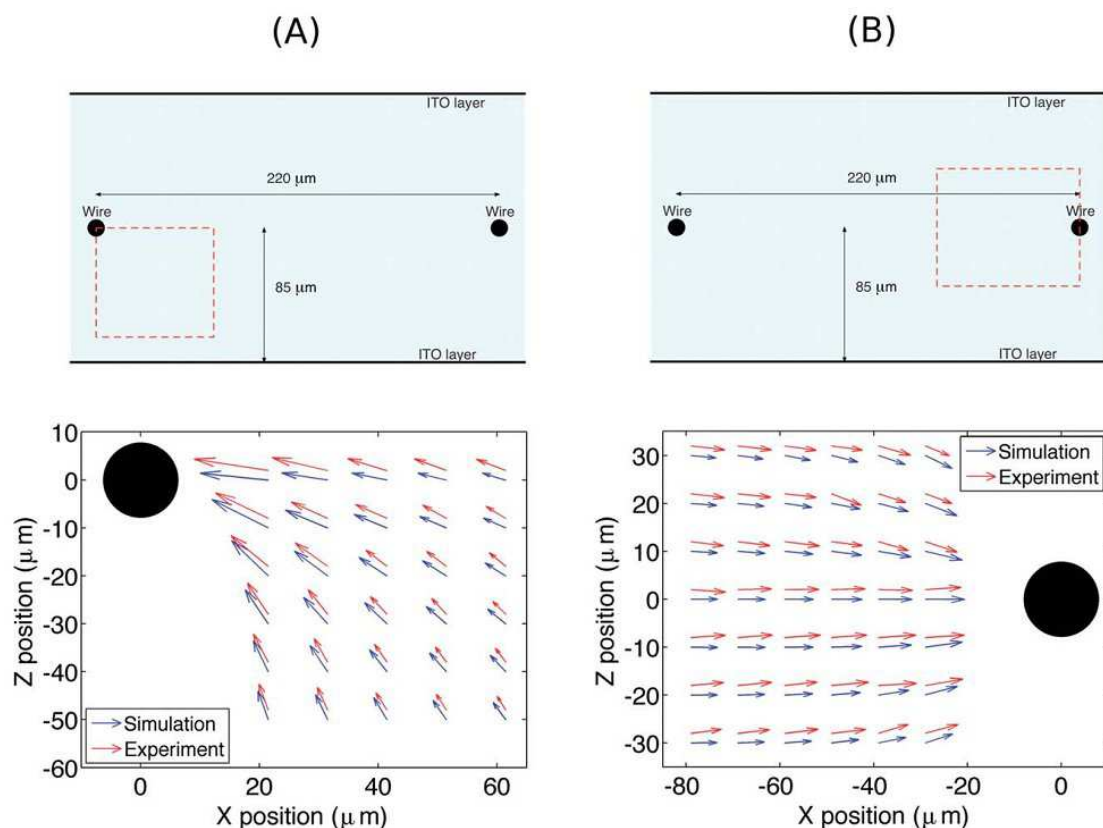


Figure 69 The electric field mapping, measured for the two configurations. Experimental results are displayed with red arrows and are vertically shifted 1 mm for clarity. Blue arrows are the results of finite elements method simulations. The regions where the electric field was measured are highlighted by a red dashed line in the upper figures.

The wire was placed in the middle of the sample cell at the height of 85 μm from the bottom coverslip. Measurements in the proximity of the wire, where the highest field gradient is expected, have been performed. For simplicity the electric field only in a plane perpendicular to the wires axis have been measured, but it is clear that measurements can be carried out in any three-dimensional geometry. The amplitude of the sinusoidal voltage at the electrodes was  $V = 250$  mV with a frequency of 87 Hz. Starting from an initial position the sample cell was moved with a fixed step in a raster scan around the electrode. In every position the bead trajectory was acquired for 20 s. At the end of every scan the electric field at the initial position has been measured again to check that the experimental conditions did not changed during the measurements. The sensitivity of apparatus has been tested by reducing the electric field amplitude up

to reach a signal-to-noise ratio close to 1. The minimum amplitude estimable was about 250 V/m. As expected, for the symmetry of the geometry used, the y-axis component is zero. In the second geometry (Figure 69b), the electrodes were two wires (10  $\mu\text{m}$  in diameter) placed at a distance of 220  $\mu\text{m}$  positioned at a height of 85  $\mu\text{m}$  from the bottom coverslip and 90  $\mu\text{m}$  from the upper microscope slide. The amplitude and frequency of the applied voltage were the same of the first geometry. For both the configurations used, the electric field maps were obtained. Theoretical field distribution has been estimated using the finite elements method of FEMLAB package. The agreement between experiment and simulation is excellent for both the geometries investigated [8,9]. In conclusion the technique provides a direct and realistic estimation of the electric field generated by whatever complex configuration of microelectrodes even when numerical simulation can fail.

## References

- [1] L. Bousse, C. Cohen, T. Nikiforov, A. Chow, A.R. Kopf-Sill, R. Dubrow, et al., Electrokinetically controlled microfluidic analysis systems, *Annu Rev Biophys Biomol Struct.* 29 (2000) 155-181.
- [2] S.C. Jacobson, T.E. McKnight, J.M. Ramsey, Microfluidic Devices for Electrokinetically Driven Parallel and Serial Mixing, *Anal. Chem.* 71 (1999) 4455-4459.
- [3] H. Bruus, *Theoretical Microfluidics*, Oxford University Press, USA, 2007.
- [4] J. El-Ali, P.K. Sorger, K.F. Jensen, Cells on chips, *Nature.* 442 (2006) 403-411.
- [5] I.I. Barbolina, K.S. Novoselov, S.V. Morozov, S.V. Dubonos, M. Missous, A.O. Volkov, et al., Submicron sensors of local electric field with single-electron resolution at room temperature, *Applied Physics Letters.* 88 (2006) 013901.
- [6] F. Gittes, C.F. Schmidt, Interference model for back-focal-plane displacement detection in optical tweezers, *Opt. Lett.* 23 (1998) 7-9.
- [7] G. Seth Roberts, T.A. Wood, W.J. Frith, P. Bartlett, Direct measurement of the effective charge in nonpolar suspensions by optical tracking of single particles, *The Journal of Chemical Physics.* 126 (2007) 194503.
- [8] G. Pesce, B. Mandracchia, E. Orabona, G. Rusciano, L.D. Stefano, A. Sasso, Mapping electric fields generated by microelectrodes using optically trapped charged microspheres, *Lab on a Chip.* (2011).
- [9] G. Pesce, B. Mandracchia, E. Orabona, G. Rusciano, L. De Stefano, A. Sasso, Local electric field measurements by optical tweezers, *AAPP| Physical, Mathematical, and Natural Sciences.* 89 (2011).



## Conclusions

Microfluidics, and the concept of the lab-on-a-chip, shown an extraordinary success during these last fifteen years, from laboratories to commercial products. Now, to stay on top, it must reinvent itself as a every field technology in science. Two ways can be foreseen for it: (i) it can gather up the technology that is now available, and develop it fully and completely finding uses for what now exists, and motivate the development of related manufacturing technologies. This step is absolutely necessary to transform laboratory prototypes into large-scale commercial products; (ii) it can invent new things, and see if these new ideas will carry the field forward. This strategy would support later technologies but does not probably result in products, at least in a very short period. In this PhD thesis, trust has been given to both hypotheses.

By following the first hypothesis, a microfluidic assisted porous silicon array for optical label-free biochemical sensing has been realized and optimised by using numerical simulations. The microsystem has been used for the study of DNA-DNA interactions and realized as a proof of concept device. From the technological point of view, a proper fabrication process has be designed to integrate PSi elements in a microarray: silicon nitride and SU8 photoresist have been used as masking material during the electrochemical etching; pro and con have been discussed in both cases. Experimental label free detection of DNA single strands hybridization (200  $\mu$ M) is performed by monitoring the reflectivity spectra shifts of PSi Bragg reflectors. High quality reflectivity (FWHM of about 25 nm) in the visible range (Bragg resonance peak at 627 nm) has been measured for all the optical elements of the microarray at normal incidence, which demonstrates the uniformity of the electrochemical etching on the whole microarray surface. A microfluidic system, realized by soft lithography technique, has been integrated with the porous silicon based microarray. The PSi elements of 200  $\mu$ m, spaced

600  $\mu\text{m}$ , constituting a four by four array, have been functionalized by directly injecting the DNA probe molecules into the microfluidic system. Smaller sample amounts (5 $\mu\text{l}$ ) and a functionalization time significantly shorter (3h) than those required for the not integrated device have been used. The performances of the microarray, in terms of precision and reproducibility, have been optimised by computer aided design and numerical simulations. Combining transport equations and reaction dynamics, the binding kinetics of the formation of a chemical complex C, starting from two components A and B, have been analyzed in the case of a generic molecular interaction which could happen in the channel of a pressure driven microfluidic circuit used to assist microarray operations. The conditions required to optimize the uniformity of the chemical species distribution on the sensing area, in terms of starting fluid velocity and channels geometry, have been found. Different microfluidic layouts have been proposed to improve the sensing features. Experiments can be performed in dynamic flow condition, which approach seems to be the best in terms of homogeneity and time parameters for the microfluidic biosensor, but static steady flow, as the one used in the present work, can be also very effective, when required in cases where very low sample consumption is an unavoidable restriction. The integrated microarray using a label-free detection method has revealed great potentiality and it could be of interest also in other application fields of the bio-analysis.

In the field of new ideas, microfluidics has been applied to a just born area of biological research that combines science and engineering: the synthetic biology. A microfluidic platform has been realized by soft lithography to achieve the control of biological genetic network: the aim is to drive gene expression by external stimuli, using a mathematical model of the biological process, by applying appropriate conditions. The goal can be achieved by applying the same methods of control systems theory to induce gene networks to follow a pre-determined behaviour. A computer program encoding the experiment strategy controls the valves managing the delivery of the compounds in the microfluidic device. A suitable benchmark five-gene network developed in yeast cells (IRMA) can be either switched on or off by galactose or glucose administration: these dynamics can be tracked by estimating the amount of a green fluorescent protein (GFP)

fused to one IRMA's genes. The microfluidic chip hosts yeast cells in a specific micro-chamber imaged via an inverted microscope that periodically sends images to the PC. The computer closes the loop by estimating the GFP fluorescence and comparing this signal with the reference one in order to compute the next input signal to be sent to the valves. An experiment where the switching sequence accounts for 180 min galactose pulse and 180 min glucose supply has been performed. Cells were imaged at 5 minutes time intervals and GFP-associated fluorescence was quantified. Numerical estimation of the fluorescence profile over time provided evidence for a satisfactory agreement between theoretical predictions and in-vivo quantification.

In all experiments a peristaltic pump has been used to move liquids into devices. Lab-on-a-chip devices use also electrokinetic phenomena to pump, mix, inject, sort, and also to manipulate fluids, cells and particles. Electric fields are usually applied by integrated microelectrodes. An highly sensitive and precise technique has been developed to measure the direction and amplitude of an electric field generated by microelectrodes using optical tweezers as a force transducer. Negatively charged sulfate coated polystyrene micro-spheres, trapped by the optical tweezers, have been used as a probe to detect its displacement from its equilibrium position under the effect of the external electric force. The particle displacement was measured three dimensionally with nanometre precision using the back focal plane interferometry detection technique. As examples, the technique has been applied to some simple microelectrode configurations, but it can be used in whatever complex configuration is needed. The technique provides a direct and realistic estimation of three-dimensional map of the electric field generated by microelectrodes or very complex electrode structures with a resolution below a micrometre and with a sensitivity as low as a few hundreds of V/m which can be useful even when numerical simulation can fail.

In conclusion, microfluidic assisted microsystems can be considered new powerful tools for an incoming technological revolution which will bring to reality devices for environmental monitoring, medical diagnostic, and life science research, in particular proteomics and cell biology. One expected result is the advent of personalized medicine, which will be possible only if genomic and proteomic determinations should be available

## Conclusions

---

for each person. The impact on the society cannot be foreseen. The research developed in the three years PhD program presented in this thesis, is in the direction of realize new devices by combining micromachining standard techniques and microfluidics methods in order to overcome limits of laboratory instrumentation and open new horizons to scientific research.

# Ringraziamenti

Alla fine di ogni esperienza mi sono sempre fermato per pensare a ciò che è passato e ringraziare chi ha permesso di avvicinarmi al traguardo. Questa volta, dopo tre anni, le persone da ringraziare sono veramente tante e sono sicuro che chi mi ha spinto fin qui non l'ha fatto solo per il proprio dovere e neppure per ricevere un "grazie". Sono stati tre anni intensi, di speranze, di precariato ma non privi di soddisfazioni. Quando sono arrivato in questo istituto ero un giovane neolaureato e sono stato accolto con grande fiducia dal direttore Ivo Rendina nel gruppo dove ho lavorato in questi anni.

Il mio tutor con i suoi insegnamenti, con le sue battute ed a volte anche con i suoi rimproveri mai ingiustificati, ha cercato di spronarmi per farmi vincere le paure che avevo: per questo motivo a te, Luca, va un sentito grazie. Ringrazio anche Ilaria, che con la sua profonda saggezza mi ha insegnato e tramandato con pazienza moltissimi insegnamenti: spero di non avverti deluso. Grazie anche ad Edo per avermi inconsapevolmente insegnato che nella vita non si può dire sempre sì. Grazie a Mariano per la compagnia in camera pulita e per avermi introdotto nel mondo delle microfabbricazioni. Grazie a Mario M. per le buie serate in camera oscura passate a realizzare maschere. Grazie a tutti i "ragazzi" dell'istituto, Antonella, Massimo, Peppe, Pia, per la compagnia in pausa pranzo e a tutti i ricercatori per il loro supporto.

Un doveroso grazie va a Diego di Bernardo, Filippo, Chiara e Gianfranco per la collaborazione che hanno avuto con me e con l'istituto. Un ringraziamento va anche al Prof. Sasso e a Peppe con i quali ho avuto l'onore di lavorare. Ringrazio poi STMicroelectronics ed in particolare Valeria e Fabrizio che mi hanno ospitato in azienda facendomi sentire una persona "di casa".

Ringrazio la mia famiglia che mi ha supportato economicamente e moralmente in questi tre anni. Il ringraziamento più grande spetta però alla mia metà, Angelica, che mi ha consolato e spronato ogni volta che ho avuto voglia di mollare tutto: senza di te non esisterei.

Emanuele Orabona